DUCTILE FRACTURE OF LASER POWDER BED FUSION ADDITIVELY MANUFACTURED Ti-6Al-4V

Thesis

Submitted to

The School of Engineering of the

UNIVERSITY OF DAYTON

In Partial Fulfillment of the Requirements for

The Degree of

Master of Science in Mechanical Engineering

By

Christopher Anthony Negri

UNIVERSITY OF DAYTON

Dayton, Ohio

August 2021

DUCTILE FRACTURE OF LASER POWDER BED FUSION ADDITIVELY

MANUFACTURED Ti-6Al-4V

Name: Negri, Christopher Anthony
APPROVED BY:

Robert L. Lowe, Ph.D Advisory Committee Chair Assistant Professor, University of Dayton Department of Mechanical and Aerospace Engineering	Dennis J. Buchanan, Ph.D Committee Member Division Head, Structural Materials University of Dayton Research Institute Department of Materials Engineering
Luke C. Sheridan, Ph.D Committee Member Turbine Engine Fatigue Facility Air Force Research Lab	Jeremy D. Seidt, Ph.D Committee Member Research Associate Professor The Ohio State University
Robert J. Wilkens, Ph.D., P.E. Associate Dean for Research and Innovation Professor School of Engineering	Margaret F. Pinnell, Ph.D. Interim Dean, School of Engineering

ABSTRACT

DUCTILE FRACTURE OF LASER POWDER BED FUSION ADDITIVELY MANUFACTURED Ti-6Al-4V

Name: Negri, Christopher Anthony
University of Dayton

Advisor: Dr. Robert L. Lowe

Understanding the mechanical performance of additively manufactured aerospace metals is of paramount importance for the development of new structural materials and next-generation aerospace components. Of particular interest in this investigation is the titanium alloy Ti-6Al-4V produced using laser powder bed fusion (LPBF), and its structural integrity in the event of sudden aerospace-related impacts. These impacts, known as foreign/domestic object damage, can cause catastrophic damage to aircraft components and serious injuries to passengers. To enable simulation-aided design and analysis for foreign/domestic object damage survival, the overarching goal of this project is to develop a stress-state-dependent ductile fracture model for LPBF Ti-6Al-4V that is representative of the material's behavior across a broad range of loading conditions. The foundational steps presented in this thesis include the design of an experimental program to calibrate the LPBF Ti-6Al-4V fracture locus, a three-dimensional representation of the variation of equivalent plastic strain at fracture with stress triaxiality and Lode parameter, commonly utilized in continuum damage models. The proposed experimental program provides a family of mechanical tests that employ different specimen geometries (e.g., notched plane stress, plane strain, axisymmetric, and thin-walled tube specimens) and loading conditions (e.g., tension,and torsion) to access a broad window of stress states (triaxiality and Lode parameter combinations).

Six axisymmetric tension specimens were chosen from the aforementioned family of candidate specimen designs for subsequent mechanical testing and stress state analysis. The grain morphology and porosity of the LPBF-printed Ti-6Al-4V material was characterized using electron

backscatter diffraction (EBSD) and X-ray computed tomography (XCT), respectively. Quasi-static mechanical testing was performed on a servo-hydraulic load frame, with full-field surface strains measured using three-dimensional digital image correlation (DIC). The effective plastic strain (EPS) at fracture for each test (thirty total, with five runs for each of the six specimen geometries) was obtained through direct DIC measurements and the customary plastic incompressibility assumption. Traces and weighted average values of the stress state parameters (triaxiality and Lode parameter) over the plastic deformation history were obtained from parallel numerical simulations of each test. Acceptable agreement between simulation and experiment – as quantified by comparing force-displacement and principal strain-displacement curves – was observed across the majority of the test series. However, a general trend was noticed across the force-displacement plots where the simulations predicted sometimes meaningfully higher yield stresses and ultimate tensile stresses than the experiments. This discrepancy is attributed to the material constitutive modeling and/or specimen metrology.

Arithmetic averages of the stress state parameters and EPS at fracture were reported across the five tests performed for each specimen geometry. A trend of the EPS at fracture (ductility) decreasing with an increasingly negative (tensile) triaxiality is observed, consistent with a significant body of previous literature in the ductile fracture community, including previously published results on wrought Ti-6Al-4V. The research presented in this thesis complements the few existing studies on ductile fracture of LPBF Ti-6Al-4V, providing additional fracture data that can be used to calibrate tabulated or parameterized ductile fracture models used in predictive simulations of aerospace-related structural impacts.

ACKNOWLEDGEMENTS

It is with great pleasure that I acknowledge Dr. Robert Lowe for encouraging me to challenge myself and pursue my master's degree. Without his knowledge and guidance, I would not have been able to surpass the many milestones I have achieved throughout the duration of this project. The wealth of knowledge that I have acquired under his guidance will serve as a crucial steppingstone in my future as an engineer.

Thanks to the Turbine Engine Fatigue Facility at Wright-Patterson Air Force Base for funding and technical support. Members such as Justin Warner, Luke Sheridan and Onome-Scott Emuakpor, Lucas Smith all provided essential consultation throughout all stages of the project. Most importantly, I would like to express my sincerest appreciation to Dino Celli for going above and beyond to help me perform mechanical tests and provide instruction regarding Digital Image Correlation. His help was a key factor in the development of this work.

I would also like to acknowledge all the staff at both the Air Force Institute of Technology and the Material's Directorate at Wright-Patterson Air Force Base who aided in material characterization processes. Their availability and experience ensured quality X-Ray Computed Tomography and Electron Backscatter Diffraction photos.

The origination of this project would not have been possible without the help of the Principal Investigator Steve Fuchs and the applied mechanics division at the University of Dayton Research Institute. The creation and fabrication of all tested specimens were produced by the University of Dayton Research Institute's Additive Manufacturing group.

The vision and execution of this project would not have been possible without the aid of those who have conducted similar work in this field previously. The works of Jeremy Seidt, Sean Haight and Jeremiah Hammer were tremendous resources to the developing the foundational step of this project bot theoretically and experimentally. A special thank you is owed to Leyu (Doug) Wang. Doug provided key insights on how to mesh various specimen geometries.

Thank you is certainly in order to all the members of the BAMS, lab at the University of Dayton. I would especially like to thank Luke Hoover for being my closest friend for all six years at the University of Dayton. As roommates, cross country teammates, lab partners and now co-workers, our friendship has been a staple to bettering myself as a person and as an engineer. Working in parallel with each other on our respective theses has been an exciting experience as it allowed us to bounce numerous ideas off each other and refine our skills across so many disciplines.

Above all I would like to thank my family. Without my close relationship to them I would most certainly not be able to achieve my potential. They are always there for me throughout all of the difficult times in my life. My mother and father, Kathy and Rick, are always able to offer me love, support and guidance at any crossroad I have stumbled upon and I am forever grateful for them. My siblings Andrew, Katherine and Claire are the closest people to me and never fail to brighten my day with absurdly funny life adventures. I would like to thank my brother Andrew especially though for being my role model and best friend in my life. He is the most genuine, caring, and selfless person I have ever met. I strive to develop his level of patience kindness and conscientiousness.

TABLE OF CONTENTS

LIST OF FIGURES

LIST OF TABLES

LIST OF ABBREVIATIONS AND NOTATIONS

Abbreviations:

2D	Two-Dimensional
3D	Three-Dimensional
AM	Additive Manufacturing
ASTM	American Society for Testing and Materials
CAD	Computer Aided Design
DED	Directed Energy Deposition
DIC	Digital Image Correlation
EB	Electron Beam
EBSD	Electron Backscatter Diffraction
FAA	Federal Aviation Administration
FEA	Finite Element Analysis
FOD	Foreign Object Debris
HIP	Hot Isostatic Pressing
IIHS	Insurance Institute for Highway Safety
LMD	Laser Metal Deposition
LPBF	Laser Powder Bed Fusion
NTSB	National Transportation Safety Board
OEM	Original Equipment Manufacturers
SEM	Scanning Electron Microscope
UAV	Unmanned Aerial Vehicle
XCT	X-ray computed tomography

Notations:

B	Left Cauchy Green Deformation Tensor
D	Damage Parameter

D_1, D_2, D_3, D_4, D_5	Calibrated Damage Model Parameters
δ_{ij}	Kronecker Delta
ε	Hencky Strain Tensor
$\varepsilon_1, \varepsilon_2, \varepsilon_3$	Principal Hencky Strains
$\Delta\varepsilon_p$	Equivalent Plastic Strain Increment
ε^f	Final Strain at Fracture
$\dot{\varepsilon}^*$	Dimensionless Strain Rate
$\dot{\varepsilon}$	Experimental Strain Rate
$\bar{\varepsilon}_p^f$	Parametrized Equivalent Plastic Strain at Fracture
$\dot{\varepsilon}_p^*$	Effective Plastic Strain Rate
$\bar{\varepsilon}$	Equivalent True Hencky Strain
ε_p^f	Equivalent plastic strain
F	Deformation Gradient
I	Identity Matrix
I_1, I_2, I_3	Cauchy Stress Tensor Invariants
J_1, J_2, J_3	Deviatoric Stress Tensor Invariants
L_c	Characteristic Gauge Length
σ	Cauchy Stress Tensor
σ_{ii}	Trace of Cauchy Stress Tensor
σ_m	Hydrostatic/Mean Stress
σ_{vm}	Von Mises Stress
σ^*	Stress Triaxiality
σ_{avg}^*	Weighted Average of Triaxiality
R	Rotation Tensor
S_{ij}	Deviatoric Stress Tensor

T^*	Homologous Temperature
μ	Lode Parameter
V	Left Stretch Tensor
v	Actuator Velocities
x	Spatial Position
X	Material Coordinate

CHAPTER 1

INTRODUCTION

1.1 Introduction

The modern world has become increasingly reliant upon its ability to develop advanced structural materials for high-capacity and high-speed travel, but such materials are subject to unexpected failure. Fail-safe guards and proper component maintenance are two key factors that could have prevented material failure in numerous past instances. However, even with the best redundancies in place, there are still circumstances where failure is beyond human control. Engineers must understand the limits and capabilities of new materials in the event of unforeseen catastrophes. The titanium alloy Ti-6Al-4V additively manufactured (AM) via laser powder bed fusion (LPBF) is an example of an emerging metal that can be used in structural designs across the aerospace, biomedical, and automotive industries. Determining the structural integrity of AM Ti-6Al-4V would allow for safer designs that reduce component failure rates. Such failures may be caused by high-energy impact events that can be studied with finite element analysis (FEA) codes capable of performing non-linear, inelastic analyses. During impact analyses, structural materials often undergo changing boundary conditions and large deformations

[1]. The FEA code used in this thesis, LS-DYNA, is frequently used for this type of analysis due to its reputability at modeling impacts and failures. With state-of-the-art predictive technology at their fingertips, manufacturers can efficiently produce products within the safe confines of the simulated environment. It is imperative that new materials, such as AM Ti-64, are carefully characterized in order to ensure the utmost safety and reliability of the end-user product.

1.1.1 Impacts and Large-Deformation Failures

This section discusses instances of non-linear, inelastic deformations and failure within structural components, as well as how FEA can be used to increase their safety and efficiency. Turbine engine components are designed by aerospace industry manufacturers to withstand various

forms of impacts and failures without significantly affecting the aircraft's structural integrity. Foreign object debris (FOD) damage is an impact event commonly associated with birds striking aircraft. According to a 2013 report published by the Federal Aviation Administration (FAA), bird strikes in the United States cause approximately $718 million in damage annually to civilian and military aircraft per year. This has resulted in a grounding of the affected aircraft for a combined downtime of 567,000 hours [2]. From 1990 to 2011, the FAA received over 100,000 reports of collisions caused by FOD; however, it is presumed this value has been underestimated by approximately 80% [3]. The data from [3] predicts these incidents will continue to occur at higher frequencies. Although rare, catastrophic events have occurred. For example, the downing of US Airways Flight 1549, an Airbus 320 that took off from LaGuardia Airport and, less than 10 miles away from its origin, struck a cluster of migratory Canadian geese [4], resulting in the damage shown in Figure 1.

Figure 1: Aftermath of US Airways Flight 1549 Turbine Engine Bird Strike; Photograph provided by AOPA [5]

The National Transportation Safety Board (NTSB) stated the FOD damage was caused by the ingestion of large birds into the turbines, which resulted in complete engine failure. The accident report also detailed how several engine components were fractured due to overloading [8]. These scenarios are extensively studied by engineers, with FEA, to ensure potential damage is contained in order to prevent other aircraft components from being affected.

Gas turbine engines are complex propulsion systems comprised of numerous moving components. The combustion process shown in Figure 2 exposes every moving part, specifically the compressor fan blades, to high tensile forces and extreme temperatures.

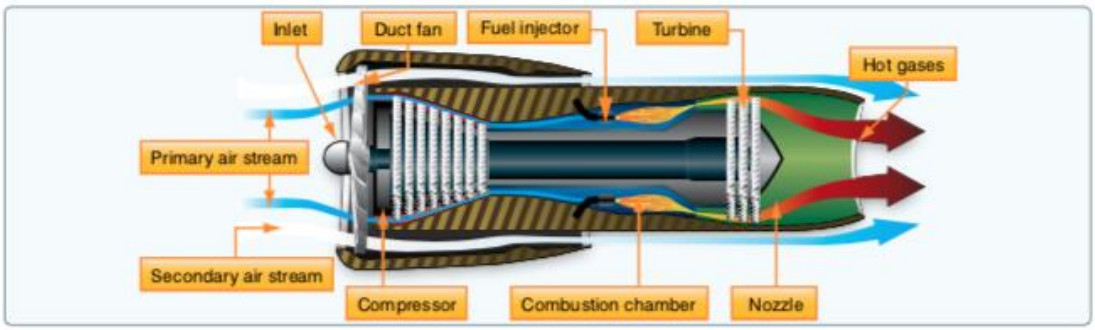

Figure 2: Anatomy of a Turbofan Engine; Diagram provided by the FAA [7]

An efficient combustion reaction between the air and fuel begins with air entering ducts, where it is subsequently compressed through a series of compressor-blade stages. The air is brought to the proper temperature and pressure before it is combined with fuel and ignited in the combustion chamber. Due to the high tensile forces and extreme temperatures experienced by the compressor fan blades during combustion, rotor-burst and blade-off events can occur. Blade-off events can result in an engine case penetration, resulting in unintentional fires or damage to the aircraft structure. Cabin depressurization is another danger posed by a blade-off event, as debris could strike the cabin. An example of this type of failure was seen on Southwest Airlines Flight 1380 on April 17, 2018. According to the NTSB, a Boeing 737-700 experienced port side engine failure causing the loss of an engine inlet and cowling during ascent. The fuselage and wing were struck by fragmented pieces of both engine inlet and cowling, resulting in a rapid depressurization of the cabin [8]. Despite the successful emergency landing of the plane, one passenger perished during the depressurization. NTSB concluded the no. 13 fan blade fatigued at the blade root in the left engine, causing the catastrophic failure [8]. The damage can be observed in Figure 3.

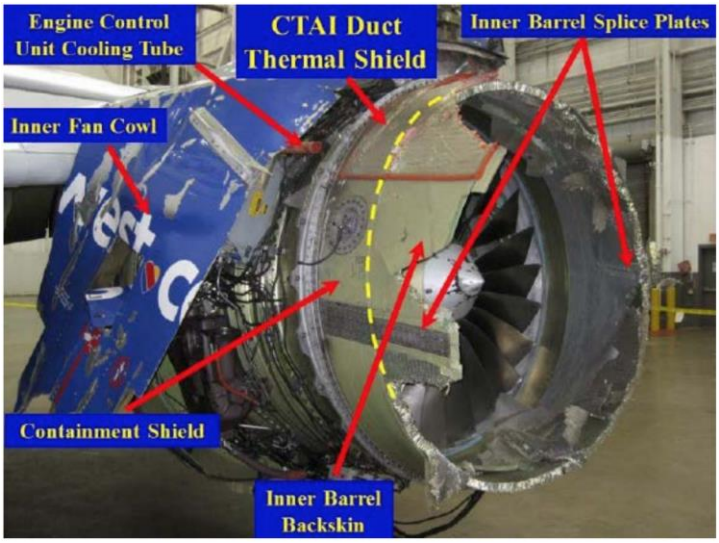

Figure 3: Resulting Damage to Cowl of Southwest Airlines Flight 1380; Photograph Provided by NTSB [8]

The area of the crack initiation was predicted to occur at the blade root, but the timing of the failure was earlier than anticipated. While the failure location was correct, the blade was not contained within the shell of the turbine, which led to the accident. The example of Southwest Airlines Flight 1380 only reinforces that there is still more research needed regarding designing accurate constitutive and ductile fracture models for structural metals in extreme environments.

Because of its modeling versatility, FEA for materials research spans across numerous industries. Automotive research and development teams are required to ensure passenger safety is guaranteed for common types of automobile accidents. Physical crash tests provide manufacturers with vehicle telemetry along with other metrics. However, it is impractical to replicate numerous forms of crashes for cars undergoing frequent redesign. The Insurance Institute for Highway Safety (IIHS) explains: “Manufacturers are constantly making changes to their vehicles, but time and budget constraints make it impossible for IIHS to test every model every year [9].” Due to these constraints, only certain cars will be physically tested based on a selective standard developed by the IIHS.

Automotive manufacturers can revise and conceptualize automobiles more effectively by using dynamic FEA software, such as LS-DYNA, to simulate crash tests. Prior to the twenty-first

century, automotive manufacturers understood the software's potential and began to experiment and invest in non-linear FEA to accurately model crash testing for automobiles. The Ford Motor Company [10] once discussed the benefits of FEA as it has increased accuracy and efficiency, leading to a faster development process. An example of the predicative capabilities of FEA can be seen in Figure 4.

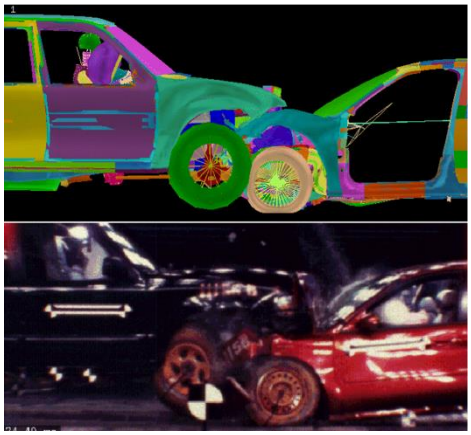

Figure 4: Automotive Crash Simulation (Top) vs. Physical Crash (Bottom); Photo Provided by Ford Motor Company [11]

Since the implementation of non-linear FEA crash testing, other codes have been developed for similar tasks. However, according to Ansys-LST, LS-DYNA is the primary crash analysis tool for over 80% of the world's major automotive original equipment manufacturers (OEMs); the code is used by an estimated 90% of tier 1 suppliers [12].

The final example of to be discussed is metal forming, which is the technology used for shaping metal alloys into useful products by processes such as "rolling, forging, extrusion, drawing and sheet-metal forming" [13]. These processes use controlled plastic deformations to shape metals, leaving forms of residual stresses behind on the surface or within the material. While there are standard mechanics of materials calculations that can be applied to metal forming processes, such as the bending of a sheet, these analytical solutions are confined to small elastic strains and an idealized deformation state. With the incorporation of FEA, standard metal processes involving large, non-linear, inelastic, and inhomogeneous deformations may be observed as they evolve and

at any location within the material. The inclusion of FEA simulations has allowed for the development and design of new metal forming processes [13].

1.1.2 Military Applications of Additively Manufactured Metals

Over the past two decades, the United States Air Force has taken a great interest in AM technologies. “With aging aircraft fleets, AM can help enable better maintenance and aircraft longevity by introducing low quantity engine components and lightweight parts [14].” As aircraft component materials progress, the technology and models used to develop them will need to mutually progress. It has been reported that approximately 75% of jet turbine engine components are suitable for AM [15]. The turbine fan blades take the shape of airfoils with cooling vanes that require complex machining via conventional methods. This limits the airflow through blades to cool them during operation. However, with the incorporation of AM, fan blades can now be created with increasingly elaborate cooling architectures. Figure 5 shows a schematic of the anatomy of gas turbine blade.

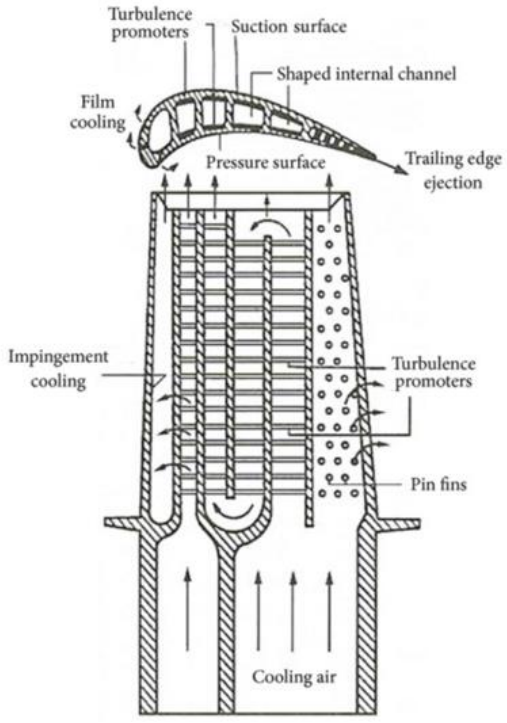

Figure 5: Gas Turbine Blade Internal Cooling Schematic; Provided by [16]

The ability to recreate discontinued or obsolete parts once produced in high quantity by OEMs is another added benefit of AM. For instance, the B-52 Stratofortress fleet (originally introduced in 1954) has not been retired since initial deployment, demonstrating a potential immediate application of AM methods. With the use of AM, manufacturers can now produce "one-off" replacement parts as they become scarcer, simultaneously reducing costs and lead times from vendor to consumer.

Further, unmanned aerial vehicles (UAVs) provide a great advantage to the United States Air Force. Their capabilities range from reconnaissance to counter insurgency missions and can vary in size greatly. Badum et al. [17] explains surveillance and support transport drones will become vital assets to modern military technology, "improving soldier safety and enabling logistic supply of remote units." Consequently, the demand for downscaled UAVs and downscaled propulsion systems has risen as a result [17]. Further, microturbines that produce less than 1 kW of power will most likely replace conventional batteries for UAVs [17]. However, there are limitations to their manufacturability: "previous work on gas turbines of this scale revealed severe challenges due to air bearing failures, heat transfer from turbine to compressor, rotodynamic instability and manufacturing limitations" [17]. A possible solution is the implementation of AM components that can be designed to have intricate and practical cooling mechanisms in order to prevent failure within certain non-structural components.

1.2 Literature Review

AM has begun to revolutionize manufacturing. It has even been described as the third industrial revolution. While AM capabilities remain in their infancy, the potential for utilization in structural applications is remarkable. "In sum, the vast potential for AM to change our lives is coming into full view" [18]. It is essential, however, that for AM metals to be properly introduced into the structural realm, these materials be tested to the point of failure for predictive modeling.

To understand the scope of AM and the significance of a ductile fracture failure model for powder bed fusion additively manufactured Ti-6Al-4V, an overview of the literature will highlight the key points of metal AM, LPBF metals, and ductile fracture.

1.2.1 Overview of Additive Manufacturing of Metals

The American Society for Testing and Materials (ASTM) has defined AM as "the use of computer aided design to build objects layer by layer. This contrasts with subtractive manufacturing, which cuts, drills and grinds material away from a solid work piece, often metal" [18]. The process begins by creating a component in computer aided design (CAD) software, then transferring it into a three-dimensional (3D) printing software where it is sliced into numerous fine layers. These layers are then reconstructed one-by-one, from the ground up, on a single stage by melting/sintering the material of choice in a path representative of that specific cross-sectional layer; this continues until every layer is printed. The completed component is removed from the substrate where any support structures are removed. Then the part is post-processed as desired. As the demand of AM has generally increased, industries such as aerospace, biomedical, and automotive are beginning to look to metal AM as an option for component design. This is because AM can create components using trustworthy metals more quickly while reducing waste, leading to improved manufacturing efficiency.

AM was introduced more than 30 years ago to develop prototype components for non-structural purposes [19]. Since then, metal AM has expanded through various techniques for a wide range of materials. These methods can be classified by their feedstock (wire or powder) and the mechanism in which each cross-sectional layer is fused together into either Directed Energy Deposition (DED) or Powder Bed Fusion [19] .The next variable is the heat/melting source, which includes lasers , electron beams (EB), plasma arc, and gas metal arc [19]. The available printing methods and the various unique thermo-mechanical properties associated with different alloys can generate significantly different microstructures, emphasizing the value of assessing each parameter for printing [19].

Alloy wire feedstock is commonly used in DED AM methods. The use of wire allows for greater rates of deposition to construct larger components [19]. Wire feedstock is also cheaper in comparison to powder stock, although post-process machining creates enough waste to offset the cost savings [19]. Wire feedstock also has "significantly less surface area per kilogram than powder product and is less likely to oxidize and absorb moisture or integrate with contaminants" [19]. Additionally, the spools themselves are not dangerous to store since the material is chemically stabilized within the ambient environment. The use of commercially available wire stock generates larger melt pools, leaving rougher surface finishes [19].

The alternative feedstock is alloy powder. A key benefit of utilizing powder feedstock is it allows for the reduction of wasted raw material; with each melted or sintered cross-sectional layer, the remaining unsintered powder can be recycled for another build. Powder is easier to feed and melt with EB and laser strategies [19] .Typical powder particle sizes range from 10-60 μm for L-PBF to 60-105 μm for EB-PBF [19] .To quantify particle size and surface morphology, scanning electron microscopy (SEM) and X-ray computed tomography (XCT) are used [19]. Powders can be produced directly from wrought metals or blended with other alloys to create specific compositions. Various methods of powder feedstock production include gas atomization, rotary atomization, water atomization, and the plasma rotating electrode process. In gas atomization, "the molten alloy is atomized by a high-pressure flow of argon and nitrogen gas" [19]. In rotatory atomization, molten metal is poured on a rotary disk, and the subsequent droplets are flung from the disk instantly solidifying them into microscopic particles [19]. In water atomization, the molten alloy is deposited into a jet stream of high-pressure water, solidifying and atomizing the droplets [19]. In the plasma rotating electrode process, a bar composed of the alloy of choice is melted using an electric arc of plasma [19]. This bar is spun about its length where, similar to the method of rotary atomization, molten droplets are discharged and solidified.

We now discuss several different methods of fusing cross-sectional layers. In Electron Beam Melting (EBM), the powder feedstock is fed from a hopper and raked onto a build plate. The

raked layer thickness can range from 50 μm to 200 μm [20]. The heat source for sintering each layer of powder is an electron beam generated by an electron gun [20]. The electron stream is accelerated by a voltage of 60 kV and guided by a magnetic scan coil [20]. Once a layer is completed, the build plate is lowered for the recoating arm to apply the next layer of powder; this process repeats until the component is completed. EBM takes place in a near ideal vacuum environment. Helium is pumped into the build chamber as a precaution to prevent the buildup of static electricity within the powder particles [20]. Another benefit of introducing helium is it increases heat conduction while simultaneously cooling the melt pool [20].

In Laser Metal Deposition (LMD), the feedstock material, wire or powder, is continuously fed from a nozzle while simultaneously being melted. Similar to welding, when the alloy is melted, shielding gases such as argon or helium protect the melt pool from foreign contaminants [20]. LMD has a feed rate between 4 g/min and 30 g/min, and a scan speed ranging from 150 mm/min to 1.5m/min, allowing for large build volume production. Lastly, LMD is not bound to a 2D plane during the build; the feed nozzle can move freely about a five degree of freedom robotic arm while the part remains stationary [20].

The final method of AM, which is also the most common, is LPBF or also known as Laser Beam Melting (LBM). LBM is associated with various names such as “Selective Laser Melting (SLM) [20], Direct Metal Laser Sintering (DMLS), LaserCUSING, Laser Metal Fusion (LMF), or industrial 3D printing” [20]. Similar to EBM, LBM sinters fine layers of powder based off of a predetermined cross-sectional area referenced from a 3D model. The layer thickness can range from 20 μm to 100 μm, allowing for more precision than EBM [20]. Also similar to EBM, the powdered metal is sourced from either a hopper or an adjacent bed next to the build plate. As the LBM build progresses, the build plate lowers as more layers are added. In order to deposit the layer precisely, and level, a recoating arm will spread the powder over the build area. The laser will then melt the powder with a power ranging from 20 W to 1 kW at up to 15 m/s with a laser spot size of between 50 μm and 180 μm [20]. Once the build is completed, the excess powder can be removed and

recycled for another build. Again, similar to EBM, LBM manufacturing occurs within a sealed chamber of inert gases, such as nitrogen and argon, to the point where oxygen makes up less than 1% of the composed atmosphere [20]. These gases cycle through the chamber to ensure the metal powder does not have any spontaneous reactions. Lastly, once the build process is completed, any additional support structures are removed. These structures can serve as structural supports for any overhanging features or as heat sinks to maintain ideal temperature [20].

1.2.2 Common LPBF Aerospace Metals

While metal AM has been growing rapidly in terms of the methods to physically build components, the ability to print new metals has equally grown. The most common engineering alloys used in structural applications are steels. There is a broad range of steels that are suited for LPBF such as austenitic steels, maraging steels, and stainless steels. These iron-based alloys are developed for general-use applications, as well as high-strength mold and tool applications [20]. AM steels tend to generate unconventional and unique microstructures, these alloys tend to generate varying phases as a function of cooling rate which can be heavily influenced by build parameters within AM [20].

Aluminum alloys are cost effective and easy to machine in their wrought forms, making them less suitable for AM. Unlike steel and Titanium, 3D printing Aluminum is difficult because of its difficulty to weld which is essentially the basis of metal AM. Other obstacles that may be encountered within Aluminum AM involves some hardenable alloys that contain zinc, Al-Zn 7xxx [20]. These compositions are notorious for generating turbulent melt pools, splatter and porosity [20]. With regard to laser melting, Aluminum has a high reflectivity which adds another complication to AM of Aluminum [20]. The melted metal may also create an issue within the build as it has a relatively low viscosity. AM Aluminum does have clear benefits. The metal's thermal conductivity allows for excellent cooling and reduction in thermally induced stresses, this reduces the need for support structures and faster processing speeds [20].

Perhaps the most sought-after AM metals are titanium alloys. These have remarkable strength-to-weight ratios and corrosion resistance, but require a lengthier process to manufacture from wrought stock. Hence AM offers a greater advantage to reduce costs and lead times. Ti-6Al-4V is one of the more common and most studied titanium alloys. This α+β alloy has a chemical composition of 6% aluminum, 4% vanadium, 0.25% (maximum) iron, 0.2% (maximum) oxygen, and the remainder titanium [21]. Figure 6 is a general overview of the partial phase diagram for Ti-6Al-4V.

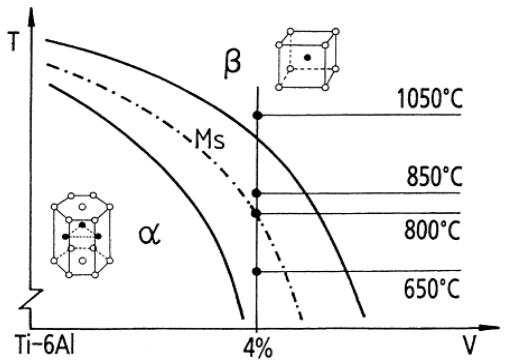

Figure 6: Partial Phase Diagram of Ti-6Al-4V [21]

"The great variety of alloy composition and related microstructure, and the allotropy of Ti-6Al-4V in combination with the high temperature gradients and complex thermal cycle usually involved in AM also make Titanium based alloys one of the most interesting materials for research regarding the relationship between AM process, microstructure and properties" [20]. Further in Gorji et. al [22] the sensitivity of AM Ti-6Al-4V to temperature gradients during manufacturing are discussed. Phase transitions occur throughout the AM processes [22]. Once the material is melted and surpasses 1000 °C, the Body Centered Cubic structure (beta grains) will cool to the Hexagonal Close Packed structure (alpha grains). However, as the material temperature drops, the highly elongated beta grain structures known as columnar grains, as seen in Figure 7 begin to develop traveling in the direction of the applied heat from the energy source [22]. Therefore it is vital to address all manufacturing parameters for an AM Ti-6Al-4V

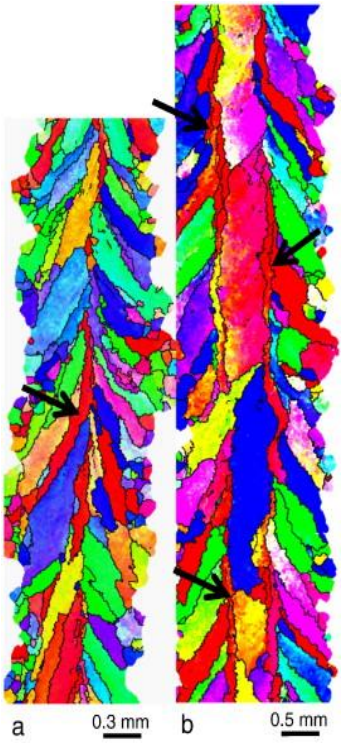

Figure 7: Electron Backscatter Diffraction (EBSD) of AM Ti-6Al-4V Columnar Microstructure [23]

1.2.3 Ductile Fracture Experiments and Failure Modeling of Aerospace Metals

The complex impact-penetration physics accompanying FOD damage generally involves high strain rates, large plastic deformations, damage accumulation, and ultimately ductile fracture, all of which must be considered in an analysis. Notably, the ductile fracture model employed in the analysis must be capable of accounting for multiple potential failure modes (e.g., plugging, petaling, and mixed-mode failure) as shown in Figure 8, which are intimately tied to the impact conditions (e.g., projectile and target material properties, geometry, relative orientation, and impact speed) and subsequent state of stress at impact.

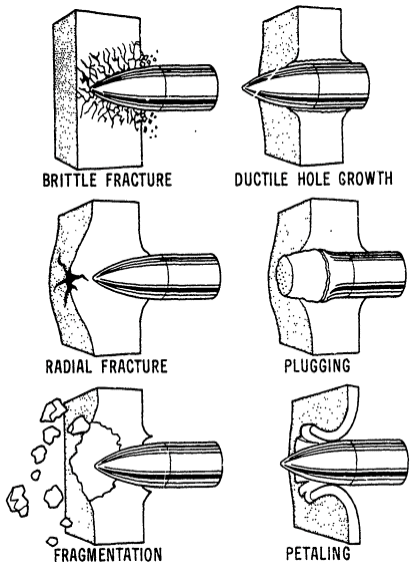

Figure 8: Potential Failure Modes During Impact Events [24]

While ductile fracture has been a phenomenon observed for a long period of time, it was not analytically studied until McClintock's pioneering work in 1968. McClintock [25] theoretically proved that at the location of plastic deformation, micro-voids will initiate, grow, and perhaps eventually coalesce. McClintock's work laid the foundation for ductile fracture mechanics from the development of a theoretical failure criterion which established that the complete state of stress needs to be taken into account when determining plastic strain at fracture [25]. Similar to McClintock's cylindrical void model, Rice and Tracey later proved that spherical void growth rates are based upon superposed hydrostatic tension [26]. They also proved that in applications of moderate and high stress triaxiality, the growth rate can become amplified "by a factor depending exponentially on the mean normal stress" [26]. Conventionally, the stress triaxiality is defined as the ratio of the hydrostatic stress,σ_m, to the Von Mises Stress, σ_{vm}, represented as:

$$\sigma^* = \frac{\sigma_m}{\sigma_{vm}} \tag{1}$$

where the hydrostatic stress is defined as (note the repeated subscript denotes an implied summation):

$$\sigma_m = \frac{1}{3}\sigma_{ii} \tag{2}$$

The von Mises stress (effective stress) is defined as:

$$\sigma_{vm} = \sqrt{\frac{3}{2}S_{ij}S_{ij}} \tag{3}$$

where $S_{ij} = \sigma_{ij} - \sigma_m\delta_{ij}$ is the deviatoric part of the Cauchy stress σ_{ij}.

Although these theoretical models could characterize failure in terms of stress state alone, Gurson [27] questioned whether it was possible to develop a more physically motivated plasticity model. His plasticity model's yield criterion was based on the incorporation of plastic dilatation of porous ductile materials with micro-voids through the void volume fraction. Gurson was able to verify how the dilatancy is dependent on the hydrostatic stress, opening the possibility of understanding plastic behavior within components subjected to increased levels of hydrostatic stress [27]. The Gurson model, at the time of its development, was employed into numerous applications of ductile fracture. The results, however, proved further development of the model was needed to incorporate void coalescence [28] and relax the assumption that void shapes are consistently spherical [29]. Tvergaard and Needleman [28] were able to manipulate the Gurson model to incorporate a void volume fraction composed of a void nucleation and a void growth component. This allowed for the determination of a critical strain that is dependent upon the stress and deformation histories [28]. This type of model is denoted a "coupled model" due to the co-dependent evolution of the plasticity and ductile fracture models. While this provides a realistic description of the evolution of ductile fracture, it is not the primary choice for impact analyses in automotive and aerospace R&D.

The development of a more popular and common "uncoupled" fracture model (where the ductile fracture model depends on the plasticity model, but not the converse) began with Johnson [30] in 1980. His model could computationally model fracture by taking the "effects of strain, strain rate, temperature, pressure and stress" into account while also being less complex than the

micromechanics-based Gurson-type models. Accordingly, this requires fewer material constants that must be calibrated to experimental test data [31]. In the Johnson-Cook model [31], ductile fracture is modeled based on a method known as damage accumulation, where the damage increment is defined as:

$$D = \sum \frac{\Delta \varepsilon_p}{\varepsilon_p^f} \tag{4}$$

and $\Delta \varepsilon_p$ is the equivalent plastic strain increment and ε_p^f is the equivalent plastic failure strain [31]. In an explicit FEA simulation, the solution will evolve over a set time interval. At each time step, every element in the simulation will have a stored variable of damage, D, starting at 0. The damage will begin to accumulate when an element experiences an increment of plastic strain, $\Delta \varepsilon$. At each time step, for each element, the plastic strain increment is normalized by the failure strain ε^f, which depends on the current triaxiality σ^* (stress state), strain rate $\dot{\varepsilon}^*$, and temperature T^*:

$$\varepsilon^f = (\sigma^*, \dot{\varepsilon}^*, T^*) \tag{5}$$

An element will fail and erode when the summation of all the increments of damage, D, is equal to one.

The experiments developed by Hancock, Mackenzie, and Brown [32] – which proved that effective strain at fracture is strongly dependent upon the stress triaxiality – paved the way for the development of the Johnson-Cook model. When stress triaxiality increases, which is indicative of a tensile-dominated stress state, the effective strain at fracture will be significantly lower [32]. In 2004, Bao and Wierzbicki [33] calibrated a ductile fracture locus for the aluminum alloy 2024-T351 by conducting a series of tensile tests that captured the relationship between failure strain and average triaxiality. They altered the value of triaxiality in their specimens by varying the notch radius within the gage section, aiming to cover a broader range of triaxialities than Ref. [32] for improved model fidelity. Figure 9 shows a piecewise fracture locus comparing plastic strain at fracture to triaxiality.

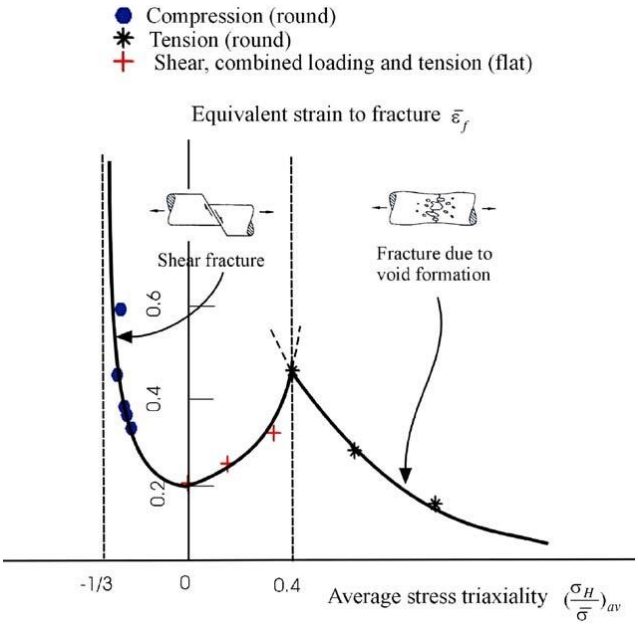

Figure 9: Two-Dimensional (2D) Fracture Locus of Aluminum Alloy 2024-T351 [33]

Interestingly, Bao and Wierzbicki noted even though "fracture ductility was found to be strongly dependent on the stress triaxiality. It was also observed that shear fracture dominates in the upsetting tests which is in the range of negative stress triaxialities [33]." This conclusion began investigations to understand how shear deformation plays a role in quantifying the stress state for a given specimen. In 2006, Barsoum and Faleskog developed a study that took a similar approach to Bao and Wierzbicki, where different specimens were assessed for triaxiality and fracture strain [34]. However, the Lode parameter, μ, was also included as an additional stress state parameter because it took shear deformation into account. The Lode parameter is defined as "a function of the third invariant of the stress deviator and is used to distinguish between the different shear stress states in three dimensions ranging from axisymmetric tension to biaxial tension with axisymmetric compression and passing through in-plane shear" [35]. Here, μ is taken to be the normalized third invariant of the deviatoric stress, i.e.,

$$\mu = \frac{27}{2}\frac{J_3}{\sigma_{vm}^3} \tag{6}$$

where J_3 is the determinant of the deviatoric stress tensor **S**:

$$J_3 = \det(\mathbf{S}) \tag{7}$$

Barsoum and Faleskog concluded that at low levels of triaxiality the Lode parameter is crucial to characterizing ductility and the stress state. This changes the fracture locus from a 2D plot, as seen in Figure 9, to a 3D surface plot where fracture strain becomes a function of both triaxiality and Lode Parameter.

An execution of this theory was conducted in 2012 by Hammer [36], which investigated the plastic deformation and ductile fracture of wrought Ti-6Al-4V. The intent was to develop accurate plasticity and failure models that could be applied to modeling high-energy impacts (e.g., blade-off and rotor-burst events) in LS-DYNA. While experimentation was successful, Hammer concluded the parameterized Johnson-Cook failure model would not suffice in terms of accuracy. It was recommended that a more sophisticated material card such as LS-DYNA's *MAT_224 material card be employed [36]. *MAT_224, also known as the tabulated Johnson-Cook model, is an elastic-viscoplastic constitutive model that gives the option to define strain rate and temperature dependent stress strain curves [38]. With regard to the failure model, *MAT_224 uses a Johnson-Cook accumulated damage model to determine failure in an element together with a tabulated failure surface constructed from user-defined experimental data.

Building on Hammer's work, Haight et al. [37] developed a tabulated ductile fracture model for wrought Ti-6Al-4V using *MAT_224. Parallel numerical simulations of Hammer's ductile fracture experiments were performed to deduce the triaxiality, Lode parameter, and effective plastic strain at fracture in the most highly strained element in the specimen gage. These data points were then used to construct a three-dimensional failure surface. The development of this failure model proved to be effective based on validation experiments. The validation test consisted of a high-speed projectile impact against a wrought Ti-6Al-4V plate. The exit velocity of the projectile was compared against a simulated test setup in LS-DYNA. The authors concluded that the failure model was reasonably accurate.

1.2.4 Ductile Fracture of LPBF AM Ti-6Al-4V

For the first time in 2019, Wilson-Heid and Beese [39] reported results from a novel investigation of the ductile fracture behavior of Ti-6Al-4V additively manufactured (AM) using laser powder bed fusion (LPBF) in various printing orientations. Mechanical tests were performed on six different specimen geometries (butterfly, circular disk, and thick notched) to generate seven different states of stress. The results (i.e., Lode parameter, triaxiality, and equivalent plastic strain at fracture) from the mechanical tests were then fitted to six different ductile fracture models. The authors found that both the triaxiality and Lode parameter are needed to quantify the state of stress. A calibrated modified Mohr-Coulomb failure criterion was found to be the most appropriate model for capturing the effects of the stress state parameters on fracture. The authors noted that the maximum shear stress failure criterion can be calibrated with a single test, but this can be challenging to accomplish. Reported failure strains were greater for specimens manufactured with respect to the build direction compared to those built perpendicular to the build direction. An error margin of ± 15% with respect to the two-branch empirical fit, maximum shear stress, modified Mohr-Coulomb, and Hosford-Coulomb fracture criterions was appropriate for describing the experimental variation of the fracture strain in LPBF Ti-6Al-4V.

Recently in January 2021, Nalli et al. [43] began the investigation of ductile damage assessment for several wrought and AM aerospace alloys, one being Ti-6Al-4V. To calibrate the ductile damage models, uniaxial tension tests were carried out on four types of specimens. Round Bars, Round Notched Bars, Plane Strain specimens and Torsional specimens were fabricated to evoke specific stress states. The specimens of each alloy types were either tested in their wrought form, as built from AM or post-processed from AM. The data from the mechanical tests and parallel numerical simulations were synthesized to help fit the data to four ductile fracture failure models. The results showed the AM specimens were more brittle than their wrought counter parts, however there was not a significant reduction in mechanical properties such as yield strength or ultimate tensile strength.

1.3 Research Opportunity

Respective to the reviewed literature, only two previous studies have investigated the ductile fracture of LPBF AM Ti-6Al-4V. Thus, at present, the ductile fracture locus of LPBF AM Ti-6Al-4V is sparsely populated, limiting its utility in predictive models for investigating the impact physics of this emerging material. Additional ductile fracture experiments that probe not-yet-investigated stress states are needed.

1.4 Intent of Research and Experimental Overview

Failure prediction within metals is determined by the generation of an accurate constitutive model and ductile fracture model. The purpose of this thesis is to provide foundational knowledge about the structural limits of LPBF AM Ti-6Al-4V in the form of a ductile fracture failure model, using a *MAT_224 material card within LS-DYNA. This will be achieved by designing, mechanically testing, and numerically simulating mechanical test specimens to generate the three necessary components of failure surface: triaxiality, Lode parameter and the plastic strain at fracture. It is anticipated that the states of stress probed in this investigation will be novel for LPBF AM Ti-6Al-4V. The specimens that will be used for this project will be manufactured together in a single build.

CHAPTER 2

DESIGN OF DUCTILE FRACTURE EXPERIMENTAL PROGRAM

2.1 Goals and Overview

In this chapter, mechanical test specimens are designed and simulated in LS-DYNA® to target unique stress states at fracture for laser powder bed fusion additively manufactured Ti-6Al-4V. Nominal baseline specimen geometries are developed based on previous designs in Hammer [36], Haight et al. [37], and Seidt [46], with the intent of populating four key areas of 2D stress state space: plane stress tension, axisymmetric tension, plane strain tension. And pure torsion (Figure 10).

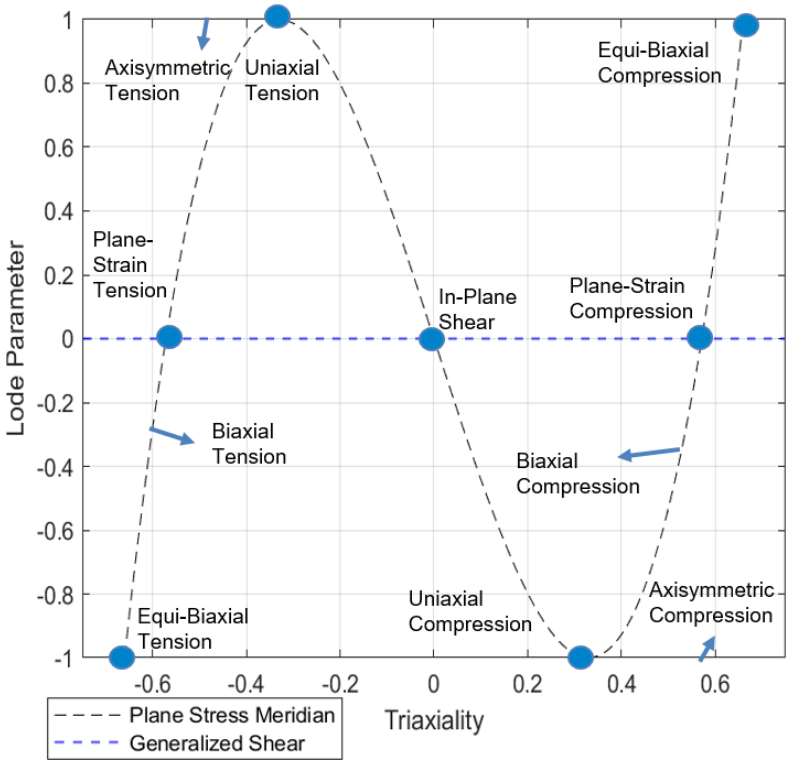

Figure 10: 2D Stress Space (Lode Parameter vs. Triaxiality)

2.2 Preliminary Continuum Mechanics and Kinetics

To capture the triaxiality and the Lode parameter, the LS-DYNA FEA suite will be used. Execution of the solver's code outputs element-wise data on the macroscopic level within a

continuum. At this level, matter is regarded as continuous and infinitely divisible, with no attention given to the underlying molecular structure [40]. As a consequence of external loadings, there will be deformations in the material of ranging magnitudes, described by the general motion of a continuum:

$$\mathbf{x} = \chi(\mathbf{X}, t) \tag{8}$$

In this motion, each material particle is mapped from its material coordinate, **X**, in the reference configuration to its spatial position, **x**, in the current configuration [40]. The local deformation is described by a tensor known as the deformation gradient **F**:

$$\mathbf{F} = \text{Grad}\,\mathbf{x} = \frac{\partial \mathbf{x}}{\partial \mathbf{X}} \tag{9}$$

The deformation gradient, **F**, contains knowledge of what happens – both stretch and rotation – to any element within the continuum. **F** can be polarly decomposed into the left stretch tensor, **V**, and the rotation tensor, **R**:

$$\mathbf{F} = \mathbf{VR} \tag{10}$$

The left stretch tensor, **V**, can be related to the left Cauchy-Green deformation tensor, **B**, defined as:

$$\mathbf{B} = \mathbf{F}\mathbf{F}^{\mathrm{T}}, \qquad \sqrt{\mathbf{B}} = \mathbf{V} \tag{11}$$

Subsequently, the Hencky (logarithmic, true) strain tensor, $\boldsymbol{\varepsilon}$, can be derived from the left stretch tensor:

$$\boldsymbol{\varepsilon} = \ln \mathbf{V} \tag{12}$$

A benefit of choosing the Hencky strain tensor is its ability to measure strains at large deformations [41]. The equivalent true strain, $\bar{\varepsilon}$, can be computed from the Hencky strain tensor with respect to the principal Hencky strains:

$$\bar{\varepsilon} = \frac{2}{\sqrt{3}}[(\varepsilon_1 - \varepsilon_2)^2 + (\varepsilon_2 - \varepsilon_3)^2 + (\varepsilon_1 - \varepsilon_3)^2]^{1/2} \tag{13}$$

The state of stress can be described at any point by beginning with the second order Cauchy (true) stress tensor, σ. The tensor can be manipulated to define its three principal invariants:

$$I_1 = \mathrm{tr}(\boldsymbol{\sigma}) \qquad I_2 = \frac{1}{2}[(\mathrm{tr}\,\boldsymbol{\sigma})^2 - \mathrm{tr}\,\boldsymbol{\sigma}^2] \qquad I_3 = \det \boldsymbol{\sigma} \tag{14}$$

Next, **σ** can be additively decomposed into two components, the spherical (volume-changing) component, $\sigma_m\mathbf{I}$, and the deviatoric (shape-changing component), **S**:

$$\boldsymbol{\sigma} = \sigma_m\mathbf{I} + \mathbf{S} \tag{15}$$

where the mean stress σ_m is defined in Eq. (2). The three principal invariants of **S** are:

$$J_1 = \mathrm{tr}(\mathbf{S}) \equiv 0 \qquad J_2 = \frac{1}{2}[(\mathrm{tr}\,\mathbf{S})^2 - \mathrm{tr}\,\mathbf{S}^2] \qquad J_3 = \det \mathbf{S} \tag{16}$$

The von Mises (equivalent) stress is then defined from the second invariant of the deviatoric stress:

$$\sigma_{vm} = \sqrt{3J_2} \tag{17}$$

Recall from Eqs. (1) and (6) that the stress triaxiality and Lode parameter are defined as:

$$\sigma^* = \frac{\sigma_m}{\sigma_{vm}} \qquad \mu = \frac{27}{2}\frac{J_3}{\sigma_{vm}^3} \tag{18}$$

The calculation of triaxiality in LS-DYNA differs from the customary equation, Eq. (18) above by a minus sign.

2.3 Simulation Details

2.3.1 Explicit vs. Implicit FEA

For the purposes of this project, uniaxial tension tests and combined loading tests will be simulated via Ansys/LST's explicit solver LS-DYNA. An explicit solver assures consistency between the developed plasticity model provided by Hoover et al. [42] and the work outlined in this thesis. Additionally, the final failure model will be validated through physical ballistic

simulation tests, similar to the validation tests conducted in Haight et. al. [37]. Regarding the FEA solver, the acquired solutions are achieved much more quickly than using an implicit solver. This is due to the fact that implicit, or static analysis, has no dependencies on inertia or damping. Each step of the solution is an iteration of convergence to establish equilibrium within the system. These steps are not bounded by time, and can be several orders of magnitude larger and computationally demanding. The numerical solver may need to invert the stiffness matrix as many times as necessary to converge on a solution [44].

Explicit analysis takes a different and less demanding approach. The solution steps are bound by time (and a stability criterion) and not dependent on convergence. At every time step the "nodal accelerations are solved directly. [44] In addition, the stiffness matrix is not inverted, making the solution faster to obtain [44] "Once accelerations are known at time n, velocities are calculated at time $n + 0.5$, and displacements at time $n + 1$. From displacements come strain. From strain comes stress. And the cycle is repeated" [44]. Ultimately, the benefit of using an explicit solver is the trade-off of less computational expense and jettisoning iteration/convergence issues in exchange for (smaller) time steps that are bound by a stability criterion.

2.3.2 Element Types, Material Models, and Boundary Conditions

Mechanical test specimens were designed and simulated in LS-DYNA® (version R10.1.0D, Ansys/LST, Livermore, CA) to target unique stress states at fracture for LPBF AM Ti-6Al-4V. Nominal baseline specimen geometries were developed based on previous designs in Hammer [36], Haight et al. [37], and Seidt [46], with the intent of populating four key areas of 2D stress state space: plane stress tension, axisymmetric tension, plane strain tension, and combined tension-torsion (Figure 10). All specimens are pre-processed in a three-step manner prior to simulation in LS-DYNA. First, all 3D solid models are rendered using SolidWorks (2019 version, Dassault Systemes, Waltham, MA), where dimensions are based on nominal design values. Second, the solid models are exported into the finite element grid generation software HyperMesh (2017.1 version, Altair, Troy, MI). Specimens are meshed using solid 3D hexahedron, 8-node elements

with a characteristic length of 0.2 mm. This characteristic length is chosen based on the mesh sensitivity analysis performed by Haight et al. [37]. Each meshed specimen is divided into three parts denoted by red, yellow, and green element colors. The green and red components (gripped sections) are modeled to be representative of the section of the specimen tab that are clamped within the hydraulic wedge grips. It is good practice for these components to occupy 75% of the specimen tabs [47]. The center (yellow) component serves as the deformable material which will be studied for stress-state characterization. Third, once the mesh is generated, it is exported to LS-PrePost® (version R4.7.22, Ansys/LST, Livermore, CA), as an include (.in) file, where element types, loads, boundary conditions, and initial conditions are assigned. All elements within the model are assigned to be under-integrated constant-stress elements (ELFORM = 1). This element type increases efficiency and accuracy, but requires hourglass stabilization. Stiffness-based hourglass control (IHQ = 6) is assigned with an hourglass coefficient QH = 0.1. Further, hexahedrons using ELFORM = 1 usually provide greater computational efficiency, and reliable responses given proper hourglass stabilization [38,].

To verify methodology and guide LPBF AM Ti-6Al-4V ductile fracture specimen design, initial benchmark simulations in this chapter will be performed using a publicly available *MAT_224 material card for wrought Ti-6Al-4V and compared to those in Haight et al. [37]. The resulting simulated stress states for wrought Ti-6Al-4V specimens are expected to be a reasonable first-order approximation for the stress states of corresponding AM Ti-6Al-4V specimens, and thus suffice for design purposes. The specimen tabs are modeled as un-deformable rigid elements using the *MAT_20 (*MAT_RIGID) material card from the LS-DYNA material library; the required material constants for *MAT_20 are density, elastic modulus, and Poisson's ratio, which are borrowed from the calibrated *MAT_224 model for wrought Ti-6Al-4V.

The last pre-processing step in LS-PrePost is to assign the simulation boundary conditions. The motion of the rigid tabs of the specimen tabs are limited via the center of mass constraint flag (CMO = 1) in *MAT_20. Additional inputs to *MAT_20 are the constraint parameters CON1 and

CON2. When both tabs are situated within the mechanical grips of the material testing system, only one remains stationary throughout testing, which is reflected in the simulation by setting CON1 = CON2 = 7, thereby constraining all translational and rotational degrees of freedom. Depending on the type of mechanical test, the actuated grip constraints in the simulation will vary. For uniaxial tension tests, displaced grips will have CON1 = 5 and CON2 = 7 so that only axial translation is permitted. For torsional loadings, CON1 = 1 and CON2 = 5 to allow for rotation about longitudinal axis. The actuator speed is assigned with a *BOUNDARY_PRESCRIBED_MOTION_RIGID card. The rate of the actuator is kept at a constant ("artificial") speed of 1 m/s. All hardening curves within the *MAT_224 material card are suppressed except the quasi-static strain rate of 1E-2/s, which is the expected strain rate during testing. A rate-independent material model reduces computational costs due to the larger ("artificial") actuator speed. An issue that could arise is the development of inertial effects, however their absence was confirmed by running simulations over a range of "artificial" loading speeds (e.g., 10 m/s, 1 m/s, 0.1 m/s), and identifying where the simulation results (e.g., force-displacement curves) first diverged [37].

Lastly, simulations of mechanical tests run in this chapter were considered terminated once a single element was deleted from the simulation. This is possible by the inclusion of the failure model provided within the wrought Ti-6Al-4V material card. It is possible results from the simulations described in this chapter and those reported by [37] will show slight differences in stress state values. This could be due to differences in meshes or the inability to capture the exact same frame of the simulation which can be altered by the reporting interval in LS-DYNA.

2.3.3 Stress-State Extraction

For any given mechanical test simulation, specific triaxialities and Lode parameters are expected to be evoked based on the specimen geometries. However, it is impossible for these values to remain constant throughout the duration of a simulation due to the onset of localized plastic deformation. The most strained elements will begin to deform irrespective of the original geometry, consequently altering the stress state parameters as seen in Figure 11.

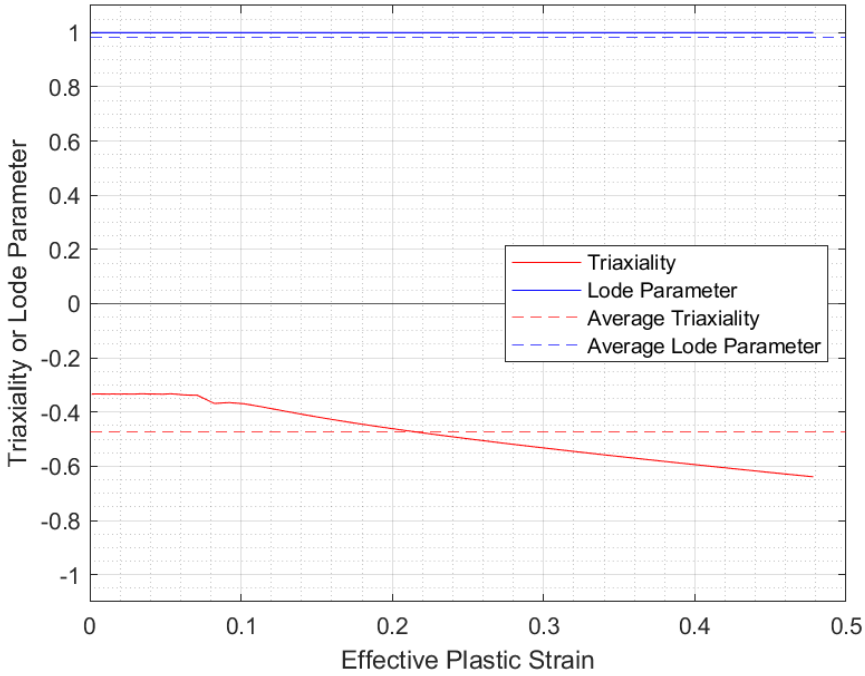

Figure 11: Representative Triaxiality or Lode Parameter vs. Effective Plastic Strain Plot

Therefore, instead of assigning stress-state parameter values based on discrete data points produced from severely strained elements, an alternative method to decide these values is used. The element that has acquired the most effective plastic strain is picked for analysis. A weighted average for the triaxiality and Lode parameter is then performed over the respective data sets to capture the evolution of the stress state parameters until the effective strain at fracture (gathered from parallel physical mechanical tests) is reached. Equations (19) and (20) demonstrate how the weighted average of triaxiality and Lode parameter are calculated [45]:

$$\sigma^*_{avg} = \frac{1}{\varepsilon^f}\int_0^{\varepsilon^f} \sigma^* \, d\bar{\varepsilon}^p \tag{19}$$

$$\mu_{avg} = \frac{1}{\varepsilon^f}\int_0^{\varepsilon^f} \mu_{avg} \, d\bar{\varepsilon}^p \tag{20}$$

Where ε^f is the effective strain at fracture. The resulting stress state values, σ^*_{avg} and μ_{avg}, from weighted averages serve as a benchmark to better understand where the unique stress state values might fall for AM Ti-6Al-4V.

2.4 Specimen Design

Based on the Johnson-Cook damage accumulation parameter shown in Eq. (4), the plastic strain at fracture will be variable with respect to unique combinations of stress triaxiality and Lode parameter. To quantify these values, mechanical tests specimens have been developed and simulated to the point of fracture with using a wrought Ti-6Al-4V *MAT_224 material card generated by the FAA [37]. In each simulation, the element that has accumulated the most damage will be analyzed, and depending on the stress state the triaxiality will range from -∞ to ∞ and the Lode parameter will range from -1 to 1. The benefit of using an existing wrought Ti-6Al-4V material card provides a reasonable estimation for where the stress state parameters should fall for respective AM Ti-6Al-4V specimens.

2.4.1 Plane Stress Specimens

The plane stress specimen family consists of four small thin specimens that will have varying notch radii to create four unique stress states that can be plotted within the 2D stress space. The first plane stress specimen will be denoted as SG1. This tensile specimen will have a straight gage section to create a pure tension state of stress. Figure 13 through Figure 19 highlight the specimen dimensions and the characteristics of each mesh.

SG1 (Figure 12) has a straight gage section so that, when the specimen is loaded uniaxially, a pure tension state of stress results. When the final SG1 mesh (Figure 13) with a characteristic length of 0.2 mm was generated, it had a total of 73,808 elements, all with an approximate 1:1:1 aspect ratio. The two gripped sections (red and green) both have 26,880 elements, and the ungripped section (yellow) has 20,048 elements. Four through-thickness elements are used throughout the entirety of the specimen.

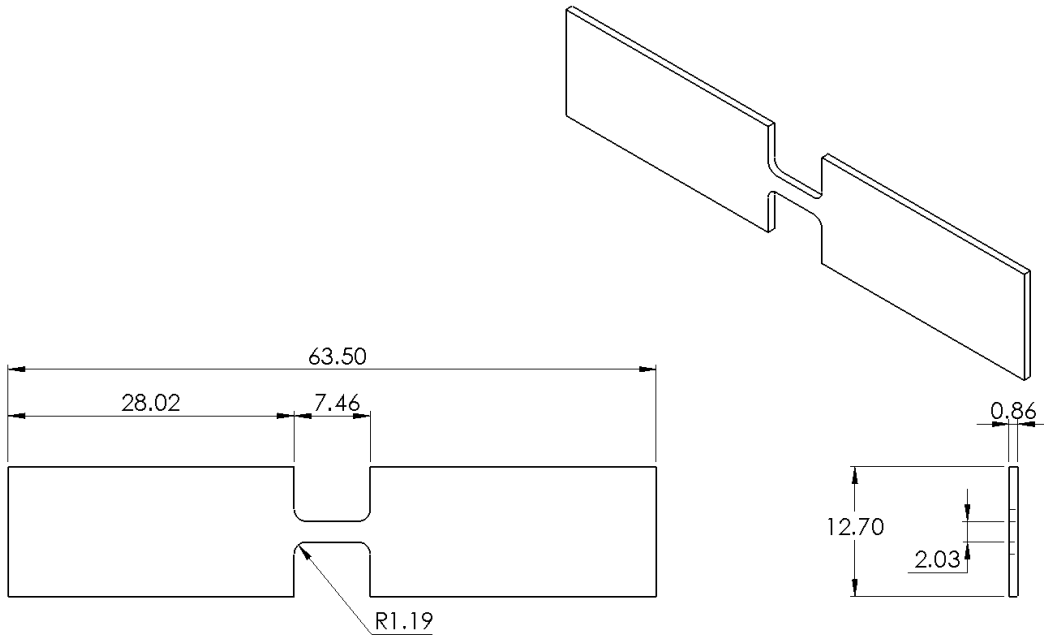

Figure 12: Orthographic Projections and Isometric View of SG1 3D Model

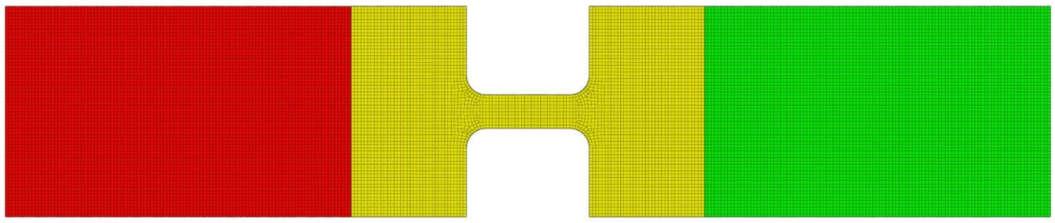

Figure 13: 3D Mesh of SG1

SG2 (Figure 14) has a gently notched gage section so that, when the specimen is loaded uniaxially, an axisymmetric state of stress that departs gently from pure tension results. When the final SG2 mesh (Figure 15) with a characteristic length of 0.2 mm was generated, it had a total of 68,288 elements, all with an approximate 1:1:1 aspect ratio. The two gripped sections (red and green) both have 20,856 elements, and the ungripped section (yellow) has 26,576 elements. Four through-thickness elements are used throughout the entirety of the specimen.

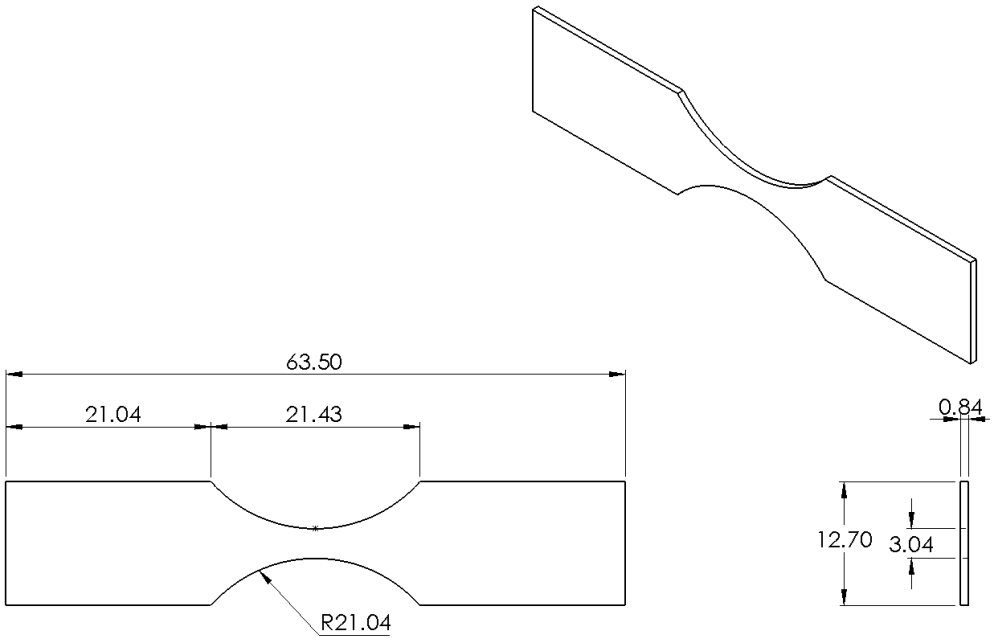

Figure 14: Orthographic Projections and Isometric View of SG2 3D Model

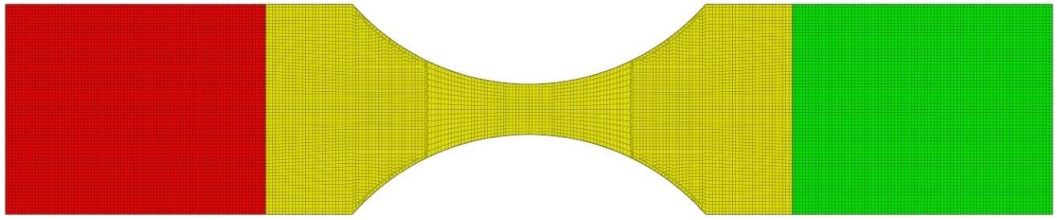

Figure 15: 3D Mesh of SG2

SG3 (Figure 16) has a more substantially notched gage section so that, when the specimen is loaded uniaxially, an axisymmetric state of stress that more significantly departs from pure tension results. When the final SG3 mesh (Figure 17) with a characteristic length of 0.2 mm was generated, it had a total of 73,888 elements, all with an approximate 1:1:1 aspect ratio. The two gripped sections (red and green) both have 25,856 elements, and the ungripped section (yellow) has 22,176 elements. Four through-thickness elements are used throughout the entirety of the specimen.

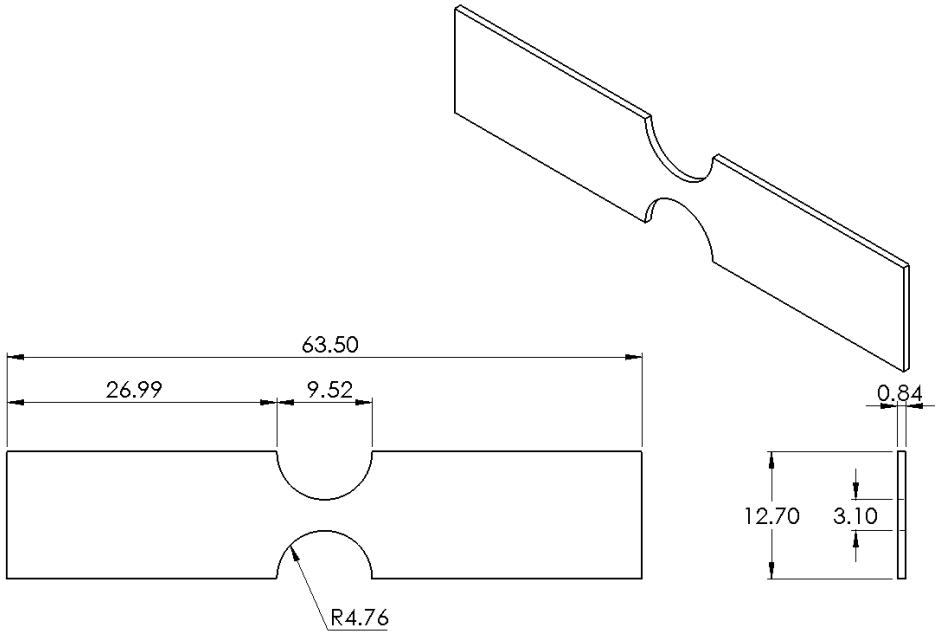

Figure 16: Orthographic Projections and Isometric View of SG3 3D Model

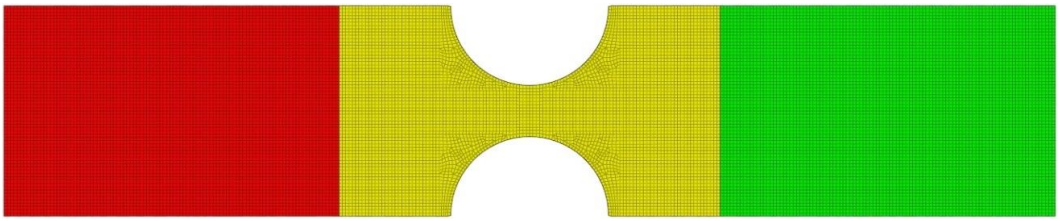

Figure 17: 3D Mesh of SG3

SG4 (Figure 18) has a sharp notched gage section so that, when the specimen is loaded uniaxially, an axisymmetric state of stress that markedly departs from pure tension results. When the final SG4 mesh (Figure 19) with a characteristic length of 0.2 mm was generated, it had a total of 78,592 elements, all with an approximate 1:1:1 aspect ratio. The two gripped sections (red and green) both have 29,264 elements, and the ungripped section (yellow) has 20,064 elements. Four through-thickness elements are used throughout the entirety of the specimen.

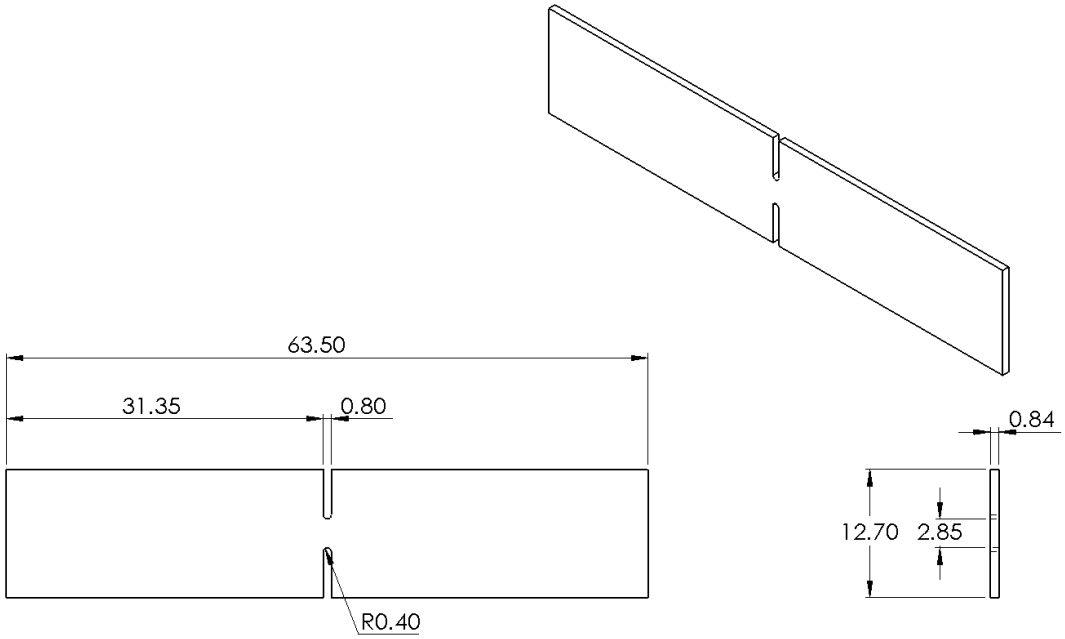

Figure 18: Orthographic Projections and Isometric View of SG4 3D Model

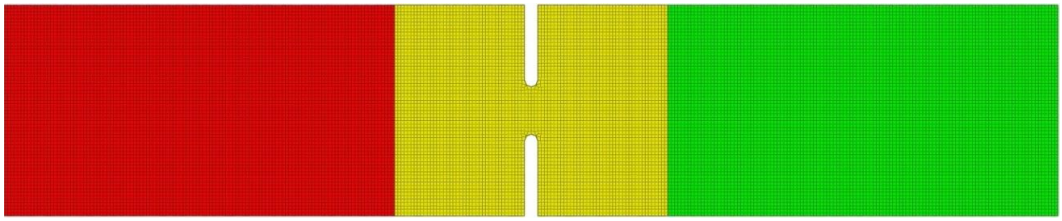

Figure 19: 3D Mesh of SG4

When the final mesh, shown in Figure 19, was generated it had a total of 78,592 elements all with an approximate 1:1:1 aspect ratio. The two tabs (Red and Green) both have 29,264 elements, and the center (Yellow) has 20,064 elements. The thickness, throughout the entirety of the specimen, is 4 elements.

The resulting stress states produced by the simulated mechanical test specimens SG1-SG4 are presented as discrete points within in 2D stress space in Figure 20. Clearly, introducing a decreasing notch radius has a significant impact on the stress state (triaxiality and Lode parameter) – namely, making the triaxiality more negative and decreasing the Lode parameter – allowing for the generation of unique stress states, all falling on (or very near) the plane stress meridian.

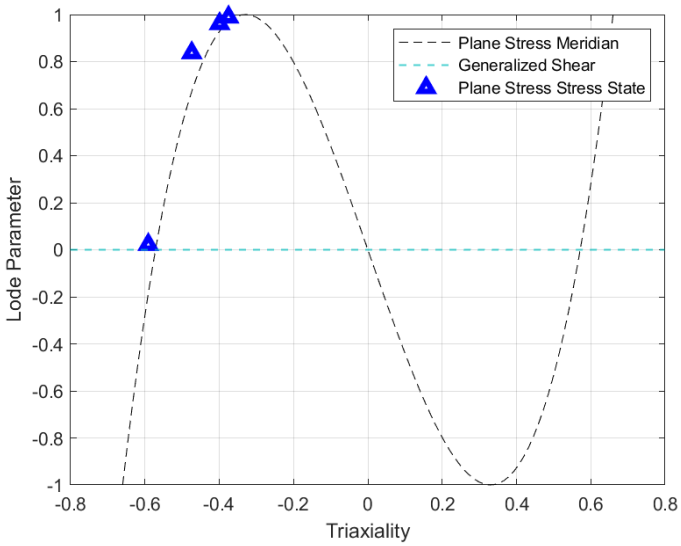

Figure 20: Targeted Plane Stress States within 2D Failure Map

2.4.2 Axisymmetric Specimens

The axisymmetric specimen family (denoted SG5-SG10) consists of six cylindrical tensile specimens (rounds) that have varying notch radii to create six unique stress states at fracture that can be plotted within the 2D stress space. Figure 21 through Figure 32 highlight the specimen dimensions and the characteristics of each mesh. Note that all dimensions are in mm.

SG5 (Figure 21) has a straight gage section so that, when the specimen is loaded uniaxially, the state of stress in the gage is pure tension. When the final SG5 mesh (Figure 22) with a characteristic length of 0.2 mm was generated, it had a total of 336,878 elements, all with an approximate 1:1:1 aspect ratio. The two gripped sections (red and green) both have 69,064 elements, and the ungripped section (yellow) has 198,750 elements.

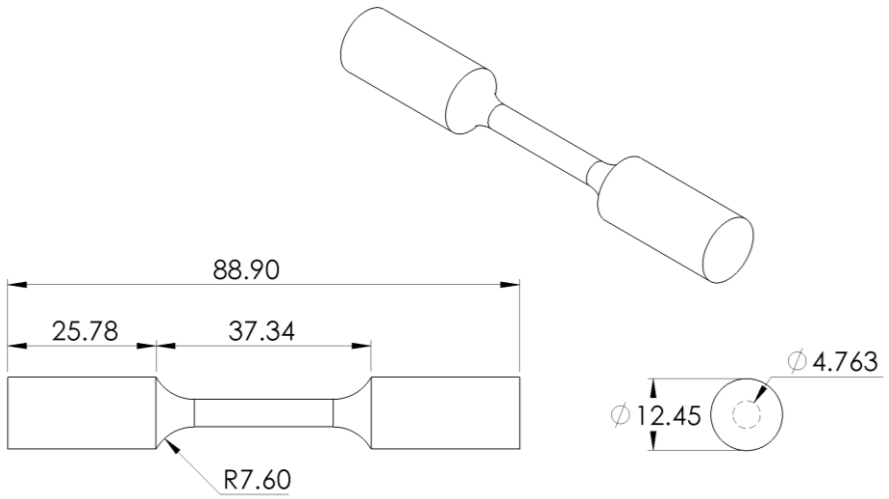

Figure 21: Orthographic Projections and Isometric View of SG5 3D Model

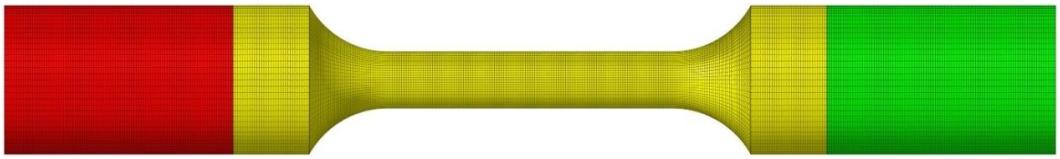

Figure 22: 3D Mesh of SG5

SG6 (Figure 23) has a notched, tapered gage section so that, when the specimen is loaded uniaxially, the state of stress at the gage center departs from pure tension. When the final SG6 mesh (Figure 24) with a characteristic length of 0.2 mm was generated, it had a total of 320,400 elements, all with an approximate 1:1:1 aspect ratio. The two gripped sections (red and green) both have 75,472 elements, and the ungripped section (yellow) has 169,456 elements.

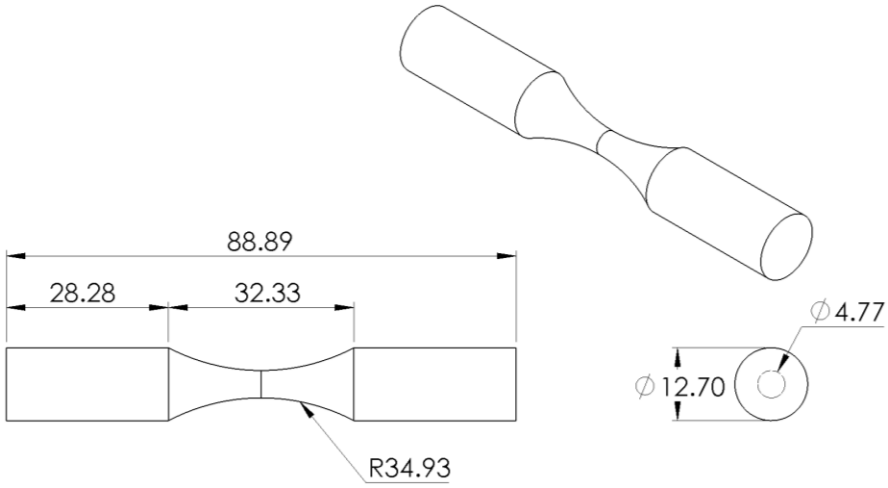

Figure 23: Orthographic Projections and Isometric View of SG6 3D Model

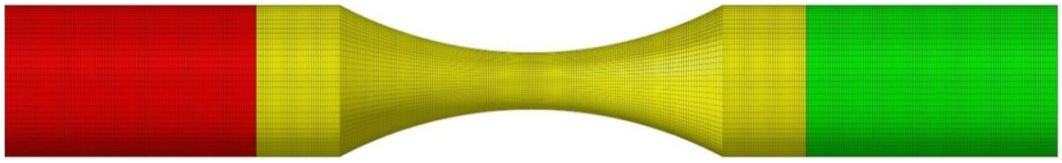

Figure 24: 3D Mesh of SG6

SG7 (Figure 25) has a notched, tapered gage section so that, when the specimen is loaded uniaxially, the state of stress at the gage center departs from pure tension. When the final SG7 mesh (Figure 26) with a characteristic length of 0.2 mm was generated, it had a total of 323,248 elements, all with an approximate 1:1:1 aspect ratio. The two gripped sections (red and green) both have 89,000 elements, and the ungripped section (yellow) has 145,248 elements.

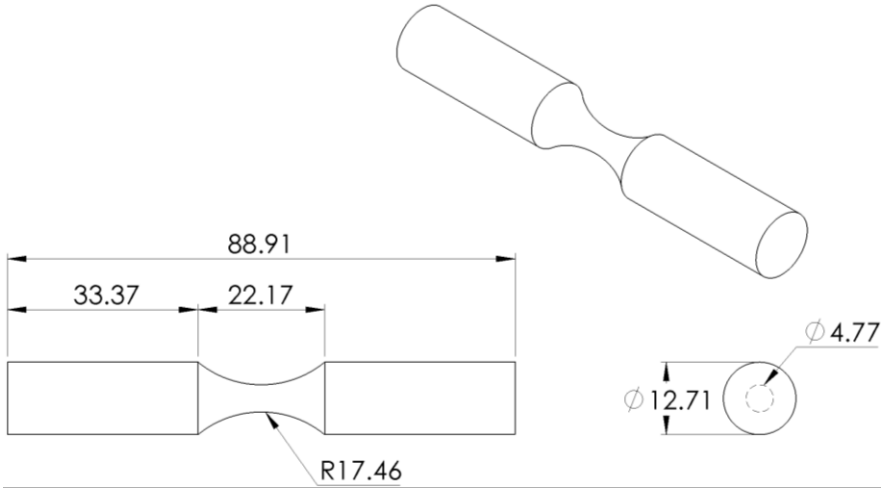

Figure 25: Orthographic Projections and Isometric View of SG7 3D Model

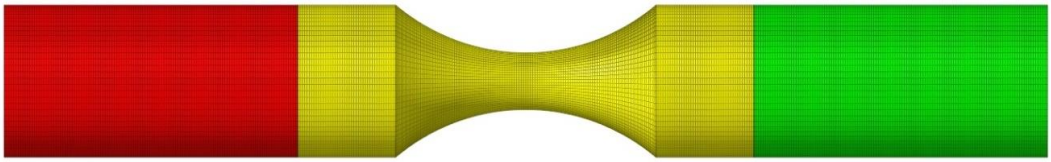

Figure 26: 3D Mesh of SG7

SG8 (Figure 27) has a notched, tapered gage section so that, when the specimen is loaded uniaxially, the state of stress at the gage center departs from pure tension. When the final SG8 mesh (Figure 28) with a characteristic length of 0.2 mm was generated, it had a total of 323,248 elements, all with an approximate 1:1:1 aspect ratio. The two gripped sections (red and green) both have 94,696 elements, and the ungripped section (yellow) has 133,856 elements.

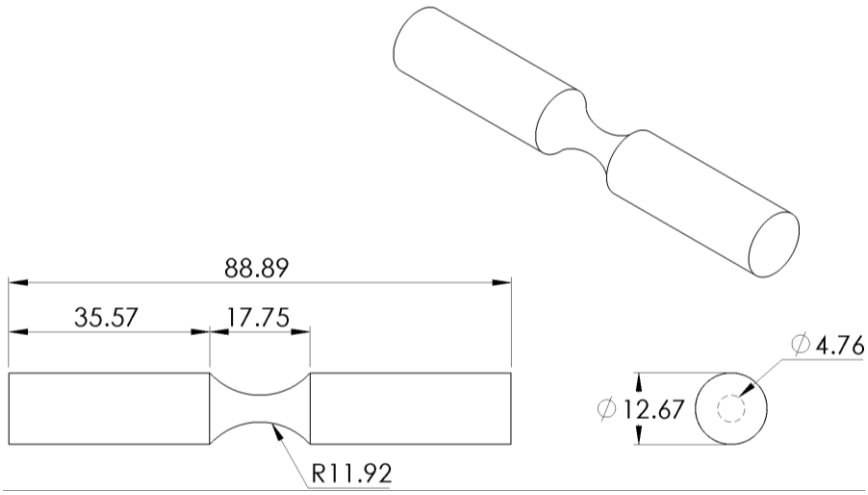

Figure 27: Orthographic Projections and Isometric View of SG8 3D Model

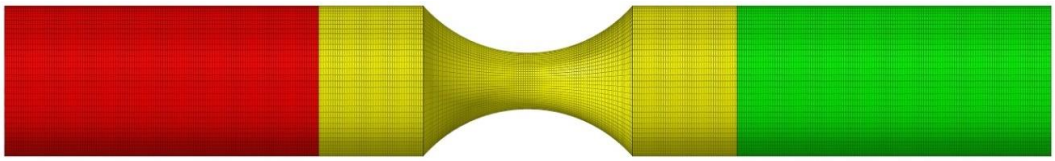

Figure 28: 3D Mesh of SG8

SG9 (Figure 29) has a notched, tapered gage section so that, when the specimen is loaded uniaxially, the state of stress at the gage center departs from pure tension. When the final SG9 mesh (Figure 30) with a characteristic length of 0.2 mm was generated, it had a total of 328,944 elements, all with an approximate 1:1:1 aspect ratio. The two gripped sections (red and green) both have 102,528 elements, and the ungripped section (yellow) has 123,888 elements.

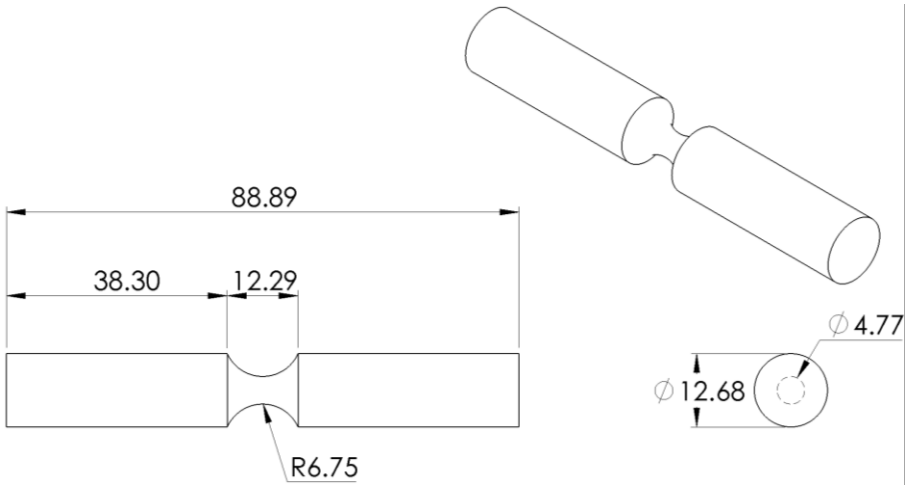

Figure 29: Orthographic Projections and Isometric View of SG9 3D Model

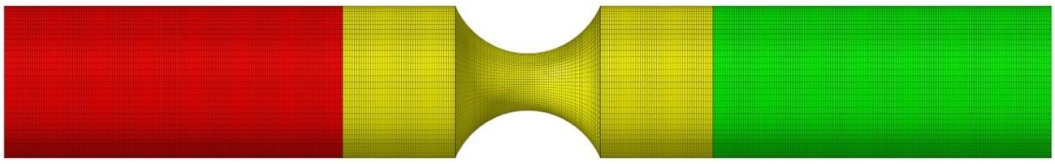

Figure 30: 3D Mesh of SG9

SG10 (Figure 31) has a notched, tapered gage section so that, when the specimen is loaded uniaxially, the state of stress at the gage center departs from pure tension. When the final SG10 mesh (Figure 32) with a characteristic length of 0.2 mm was generated, it had a total of 613,920 elements, all with an approximate 1:1:1 aspect ratio. The two gripped sections (red and green) both have 223,200 elements, and the ungripped section (yellow) has 167,520 elements.

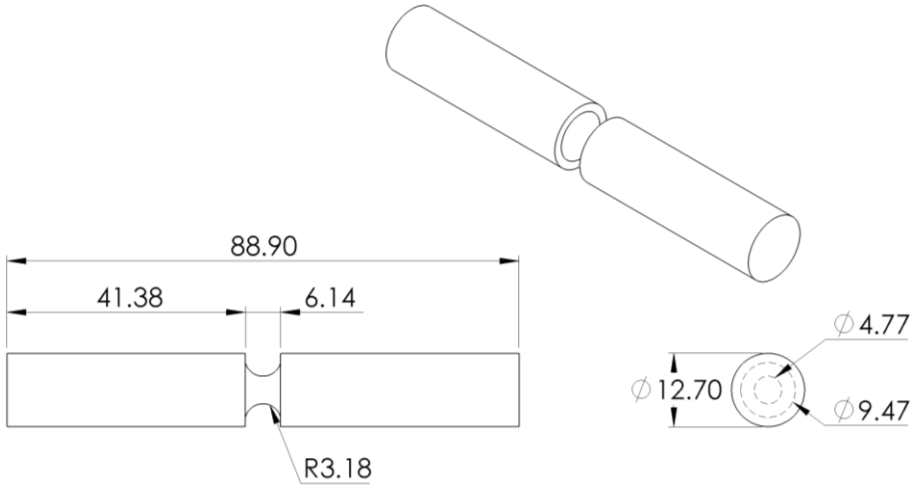

Figure 31: Orthographic Projections and Isometric View of SG10 3D Model

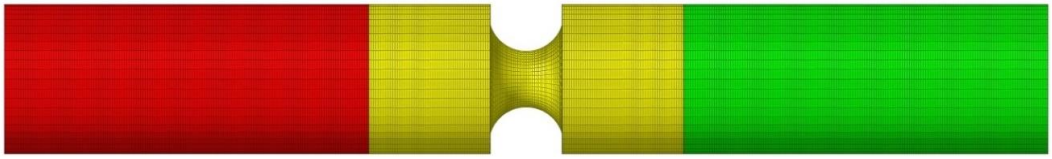

Figure 32: 3D Mesh of SG10

The simulated stress states produced by specimens SG5-SG10 are presented as discrete points within in 2D stress space in Figure 33. The introduction of a decreasing notch radius makes the triaxiality increasingly negative (at nearly constant Lode parameter), allowing for the generation of unique stress states falling within the axisymmetric region of the 2D map denoted in Figure 10.

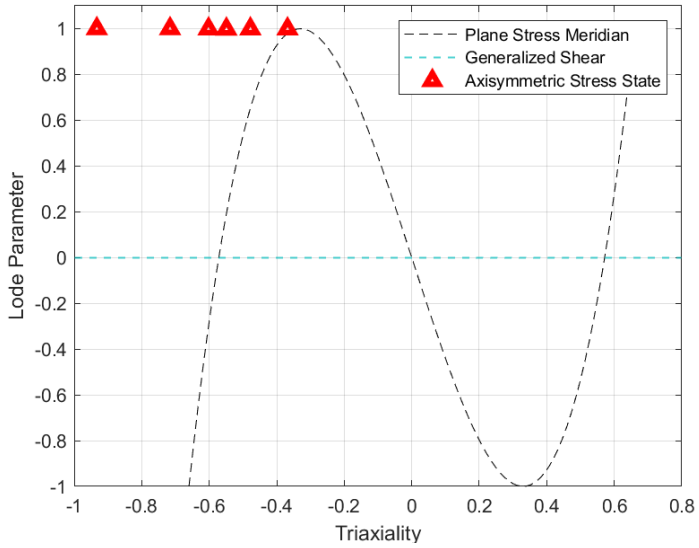

Figure 33: Targeted Axisymmetric Stress States within 2D Failure Map

2.4.3 Plane Strain Specimens

The plane strain specimen family (denoted SG11-SG13) consists of three thick tensile specimens that will have varying notch radii to create three unique stress states that can be plotted within the 2D stress space. Figure 34 through Figure 39 highlight the specimen dimensions and the characteristics of each mesh. Note that all dimensions are in mm.

SG11 (Figure 34) has a thick, tapered gage section so that, when the specimen is loaded uniaxially, the state of stress at the gage center departs from pure tension. When the final SG11 mesh (Figure 35) with a characteristic length of 0.2 mm was generated, it had a total of 3,566,668 elements, an order of magnitude higher than SG1-SG10, all with an approximate 1:1:1 aspect ratio. The two gripped sections (red and green) both have 1,300,480 elements, and the ungripped section (yellow) has 965,708 elements. 127 through-thickness elements are used throughout the entirety of the specimen.

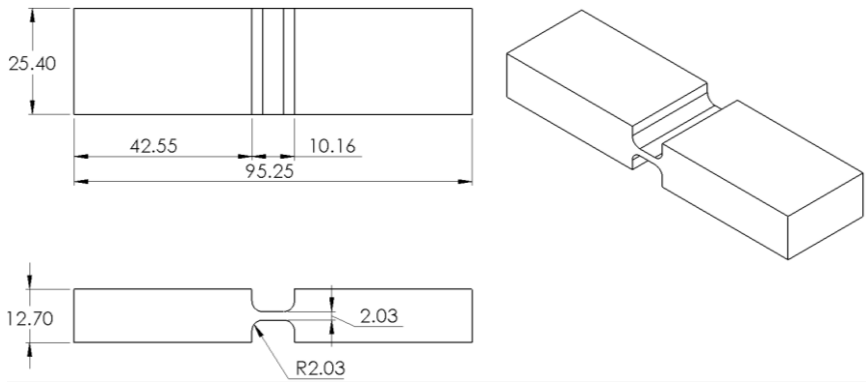

Figure 34: Orthographic Projections and Isometric View of SG11 3D Model

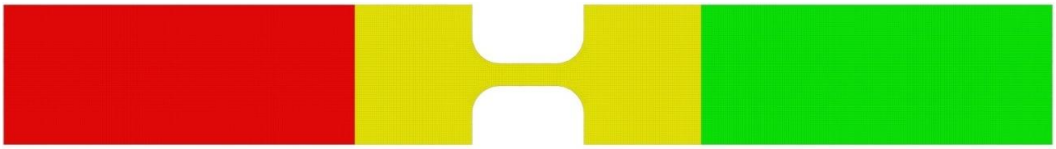

Figure 35: 3D Mesh of SG11

SG12 (Figure 36) has a thick, tapered gage section so that, when the specimen is loaded uniaxially, the state of stress at the gage center departs from pure tension. When the final SG12 mesh (Figure 37) with a characteristic length of 0.2 mm was generated, it had a total of 3,296,412 elements, an order of magnitude higher than SG1-SG10, all with an approximate 1:1:1 aspect ratio. The two gripped sections (red and green) both have 1,137,920 elements, and the ungripped section (yellow) has 1,020,572 elements. 127 through-thickness elements are used throughout the entirety of the specimen.

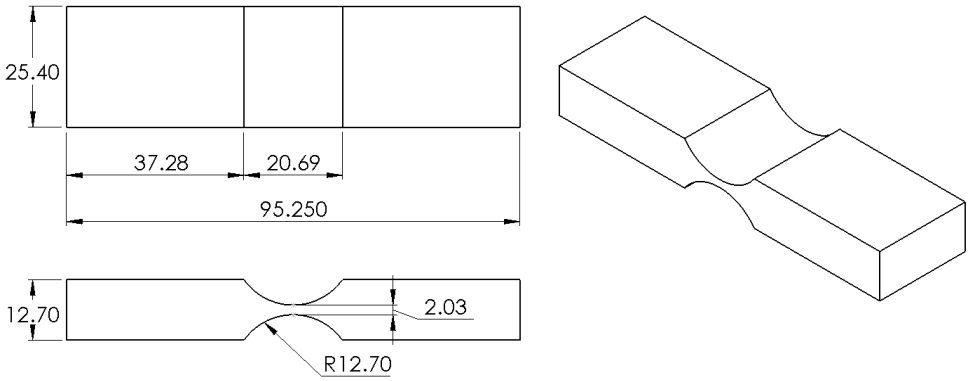

Figure 36: Orthographic Projections and Isometric View of SG12 3D Model

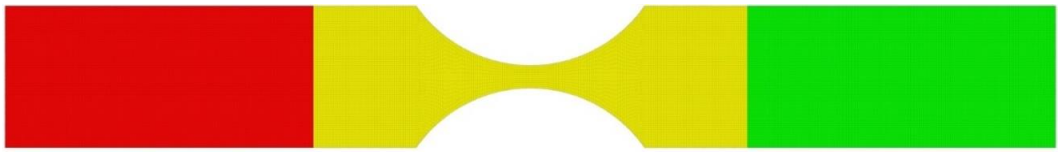

Figure 37: 3D Mesh of SG12

SG13 (Figure 38) has a thick, tapered gage section so that, when the specimen is loaded uniaxially, the state of stress at the gage center departs from pure tension. When the final SG13 mesh (Figure 39) with a characteristic length of 0.2 mm was generated, it had a total of 3,720,084 elements, an order of magnitude higher than SG1-SG10, all with an approximate 1:1:1 aspect ratio. The two gripped sections (red and green) both have 1,684,782 elements, and the ungripped section (yellow) has 350,520 elements. 127 through-thickness elements are used throughout the entirety of the specimen.

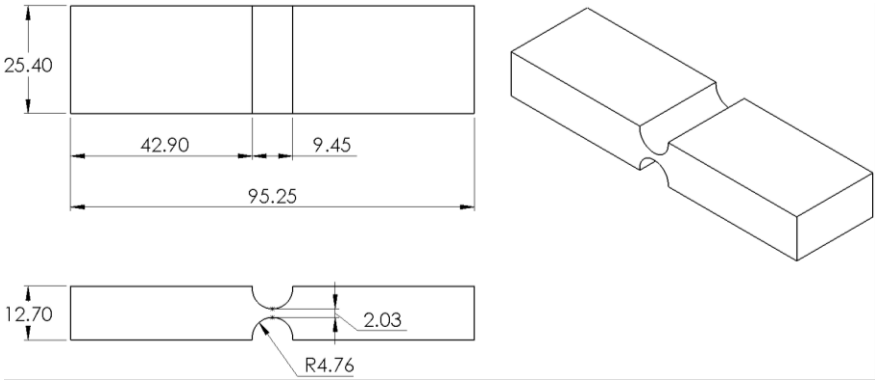

Figure 38: Orthographic Projections and Isometric View of SG13 3D Model

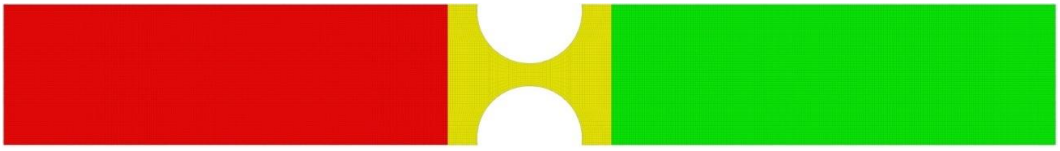

Figure 39: 3D Mesh of SG13

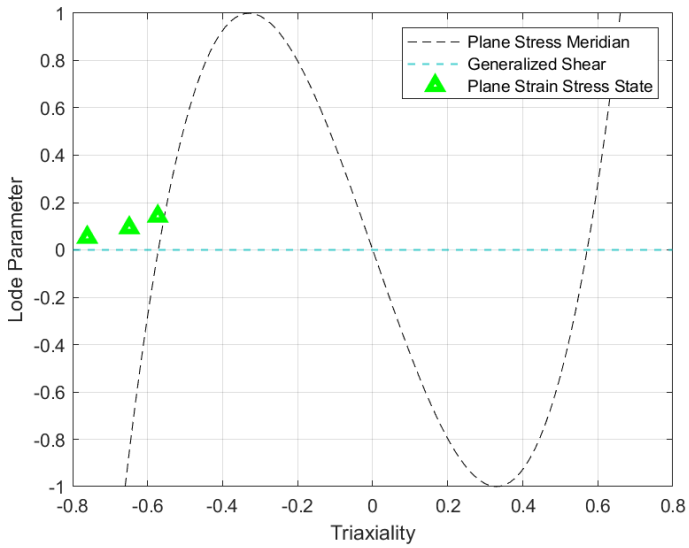

Figure 40: Targeted Plane-Strain Stress States within 2D Failure Map

The stress-states produced by specimens SG11-SG13 are presented as discrete points within in 2D stress space in Figure 40. It can be seen that the introduction of a decreasing notch radius does have implications upon the triaxiality making it more negative, allowing for the generation of unique stress states falling within plane strain region of the 2D map as denoted in Figure 10.

2.4.4 Pure Shear Specimen

The pure torsion (pure shear) specimen consists of a hollowed tube specimen with a singular straight gauge section. The motion of the mechanical grips is imposed by rotating one of the bases about the longitudinal axis of the tube. Figure 41 and Figure 42 highlight the specimen dimensions and the characteristics of its mesh. When the final mesh, shown in Figure 42, was generated, it had a total of 619,428 elements with a 0.2 mm characteristic length and an approximate 1:1:1 aspect ratio. The two gripped sections (red and green) both have 227,304 elements, and the ungripped section (yellow) has 164,820 elements.

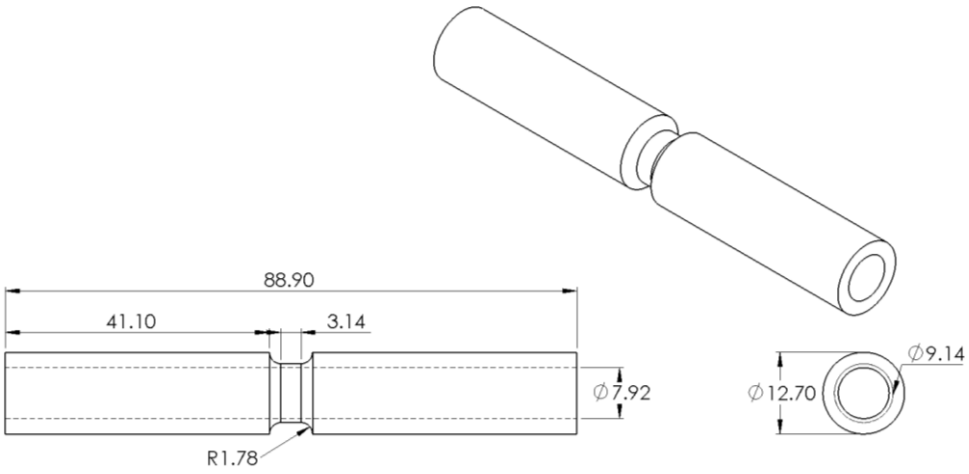

Figure 41: Orthographic Projections and Isometric View of LR3 3D model

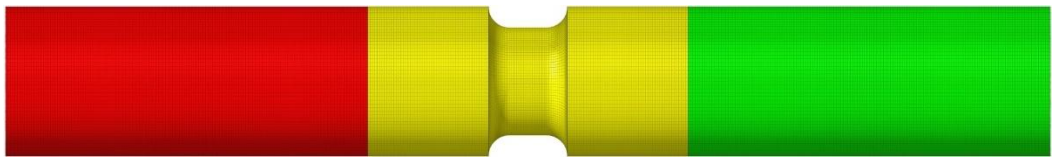

Figure 42: 3D Mesh of LR3

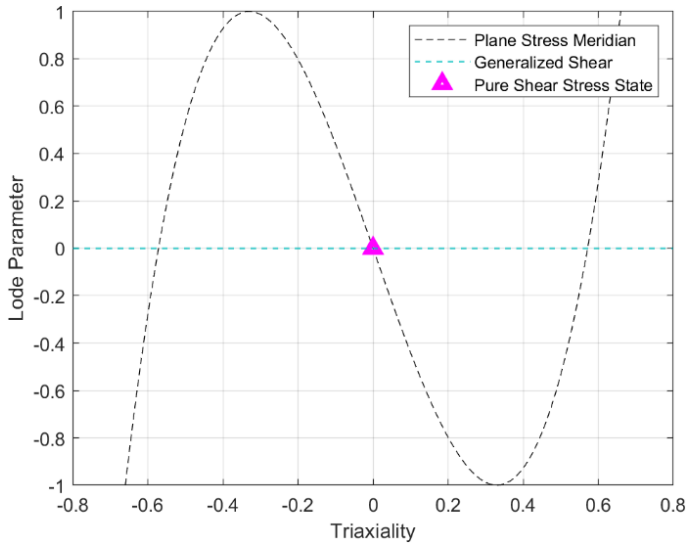

Figure 43: Targeted Pure-Shear Stress State within 2D Failure Map

The stress-state produced by specimen LR3 is presented as a discrete point within 2D stress space in Figure 43. Table 1 records both stress state parameters and the effective plastic strain at failure for the as-designed specimen geometries, and directly compares them to previous values

reported by Haight et al. [37]. The results from this analysis show strong agreement between and should provide a fair estimation for AM stress states.

Table 1: Wrought Ti-6Al-4V Stress-State Validations

Test Number	Acquired Stress States			Haight et. al		
	Triaxiality	Lode Parameter	Failure Strain	Triaxiality	Lode Parameter	Failure Strain
SG1	-0.375	0.989	0.467	-0.390	0.975	0.460
SG2	-0.399	0.961	0.428	-0.412	0.935	0.420
SG3	-0.474	0.837	0.380	-0.475	0.803	0.380
SG4	-0.591	0.022	0.140	-0.592	0.005	0.135
SG5	-0.368	0.999	0.334	-0.370	1.000	0.340
SG6	-0.478	0.999	0.286	-0.480	1.000	0.300
SG7	-0.549	0.998	0.288	-0.553	1.000	0.280
SG8	-0.602	0.999	0.240	-0.588	1.000	0.240
SG9	-0.716	1.000	0.238	-0.712	1.000	0.240
SG10	-0.933	1.000	0.290	-1.000	1.000	0.180
SG11	-0.573	0.142	0.257	-0.573	0.146	0.260
SG12	-0.649	0.093	0.218	-0.643	0.099	0.220
SG13	-0.761	0.053	0.210	-0.691	0.054	0.290
LR3	0.000	0.003	0.254	-0.014	0.059	0.259

CHAPTER 3

DUCTILE FRACTURE SPECIMENS EXPERIMENTAL PROGRAM AND SIMULATIONS

3.1 Introduction

The development of a ductile fracture model for laser powder bed fusion (LPBF) additively manufactured (AM) Ti-6Al-4V is essential for predictive numerical simulations exploring the structural integrity of aerospace components. The structural mechanics community is interested in developing failure models for both existing and new structural aerospace metals on an ongoing basis. The performance of failure models for aerospace metals is intimately linked to their proper calibration to coupon-level experiments over a broad range of stress states (triaxiality and Lode parameter), given the well-established dependence of ductility (and ductile fracture) on stress state. For the purposes of this thesis, a catalogue of candidate ductile fracture specimen designs that produce unique states of stress at failure were presented in Chapter 2. In this chapter, six axisymmetric specimen designs were chosen from this catalogue for further evaluation. This chapter will review existing work in ductile fracture of AM metals (with an emphasis on LPBF Ti-6Al-4V) and explain the hybrid experimental-numerical approach that we used to quantify the equivalent plastic strain at fracture (ductility) at various stress states (triaxiality and Lode parameter combinations).

As discussed in Chapter 1, plasticity models and ductile fracture models have yet to be extensively calibrated for additively manufactured AM aerospace metals. Several notable exceptions include the work of Concli et al. [48], Wilson-Heid and Beese [39], and Nalli et al. [43]. Concli et al. [48] investigated the ductile fracture of selective laser melting (SLM) A357 aluminum alloy using a hybrid experimental-numerical approach. An incremental plastic constitutive model with isotropic hardening and a ductile damage criterion was employed. The plasticity model was calibrated for FEA simulations using experimental data from quasi-static tensile tests on smooth, unnotched cylindrical specimens. To deduce the equivalent true stress-strain response after

necking, an inverse numerical procedure was used. To model ductile fracture, the parameterized Johnson-Cook model was adopted:

$$\bar{\varepsilon}_p^f = [D_1 + D_2 \exp(D_3 \sigma^*)]\left[1 + D_4 \ln\left(\dot{\varepsilon}_p^*\right)\right][1 + D_5 T^*] \tag{21}$$

where $\sigma^*$is the triaxiality, $\dot{\varepsilon}_p^*$ is the effective plastic strain rate, T^* is the homologous temperature, and $D_1, \ldots, D_5$ are material-dependent parameters. The parameters $D_1, \ldots, D_5$ were calibrated using mechanical test specimens that produce various triaxialities at fracture. The specimens were Round Bars, Round Notched bars, flat shear plates, and cylindrical round specimens for compression. Once the fracture locus was calibrated, the model was validated by comparing simulation to experiment for several trabecular structures subjected to compressive loads. The authors discussed discrepancies between simulated and experimental force-displacement plots, surmising they may have been a result of manufacturing imperfections. However, there were instances where the simulations had strong predictive capabilities.

Wilson-Heid and Beese [39] reported results from a novel investigation of the ductile fracture behavior of Ti-6Al-4V additively manufactured using LPBF in various printing orientations. Mechanical tests were performed on six different specimen geometries (butterfly, circular disk, and thick notched) to generate seven different states of stress. The results (i.e., Lode parameter, triaxiality, and equivalent plastic strain at fracture) from the mechanical tests were then fitted to six different ductile fracture models. The authors found that both the triaxiality and Lode parameter are needed to quantify the state of stress. A calibrated modified Mohr-Coulomb failure criterion was found to be the most appropriate model for capturing the effects of the stress state parameters on fracture. The authors noted that the maximum shear stress failure criterion can be calibrated with a single test, but this can be challenging to accomplish. Reported failure strains were greater for vertically built specimens compared to those built horizontally built specimens. An error margin of ± 15% with respect to the two-branch empirical fit, maximum shear stress,

modified Mohr-Coulomb, and Hosford-Coulomb fracture criterions was appropriate for describing the experimental variation of the fracture strain in LPBF Ti-6Al-4V.

Recently, Nalli et al. [43] conducted a study on Ti-6Al-4V titanium alloy, 17-4 PH stainless steel, and AlSi10Mg aluminum alloy to identify constitutive behavior and calibrate four different ductile fracture models. A hybrid experimental-numerical approach was used to develop constitutive models for each respective alloy along the build direction (vertically) and perpendicular to the build direction (horizontally). Four ductile fracture models (maximum equivalent strain, Rice-Tracey, Mohr-Coulomb, and Coppola-Cortese-Folgarait) were calibrated to mechanical test data to understand compare their predictive capabilities. To calibrate the ductile damage models, uniaxial tension tests were carried out on four types of specimens. Round Bars, Round Notched Bars, Plane Strain specimens and Torsional specimens were fabricated to evoke specific stress states. The results indicated that the yield stress and ultimate tensile stress did not vary significantly between wrought and AM specimens, although AM specimens exhibited less ductility. For Ti-6Al-4V and AlSi10Mg, better surface finishes were necessary to prevent premature fracture.

This thesis entails a similar hybrid-experimental numerical approach to those employed in previous investigations. However, a distinguishing feature of our work is that both the plasticity and ductile fracture models for LPBF/SLM AM Ti-6Al-4V are *tabulated* rather than *parameterized*, driven entirely by user-defined sets of experimental data and reflecting the state of the art in ductile fracture modeling. Further, our axisymmetric test series is expected to produce stress states that differ from those reported in Wilson-Heid and Beese [39] and Nalli et al. [43] for SLM AM Ti-6Al-4V, thus expanding the breadth of available experimental data in the literature for ductile fracture model calibration.

3.2 Experiments

3.2.1 Materials and Specimen Preparation

All mechanical test specimens were fabricated via laser powder bed fusion (LPBF) additive manufacturing (AM) on an EOS M290 single Ytterbium-fiber laser system with a tool steel recoater arm. The powder used for the builds was virgin grade 5 Ti-6Al-4V (AP&C Powder Metallurgy). The vendor-reported chemical composition of the powder is shown in Table 2; all values are in accordance with ASTM F2924 [49]. The vendor-reported median particle size was 38 μm.

Table 2: Chemical Composition of Ti-6Al-4V Powder (in wt.%)

Ti	Al	V	O	Fe	C	N	H	Yb	Other
Bal.	6.34	3.92	0.19	0.17	0.02	0.01	0.002	< 0.001	< 0.40

The EOS M290 printer used the EOS default “striped in-skin with post-contours” scan strategy, where stripes rotate 67 degrees every layer. Other AM build parameters are listed in Table 3. The chamber environment was inert argon. All specimens were built vertically, with their longitudinal axes aligned with the build direction. Total build time was about 72 hours.

Table 3: AM Build Parameters

Build Parameter	Value
Layer Thickness	30 μm
Laser Speed	1050 mm/s
Laser Power	260 W
Laser Wavelength	1060-1100 nm
Laser Spot Diameter	82 μm
Melt Pool Diameter	110-120 μm
Hatch Spacing	140 μm
Stripe Width	5 mm
Stripe Overlap	None
Stripe Rotation	67°/Layer
Build Platform Temp.	150 °C

During post-fusion heat treatment, the specimens were kept on the build plate (Figure 44) for the first (stress relief) cycle where they were placed in a vacuum furnace at ~650°C for approximately three hours and rapidly cooled with inert argon.

Figure 44: Post AM Build with Specimens Attached to Build Plate

The purpose of the first heat treatment is to remove residual stresses so the applied stress is the only stress the material experiences during mechanical testing. The second (ductility restoration) stage of heat treatment involved placing the specimens in the vacuum furnace at a temperature of ~800°C for approximately three hours, then rapidly cooling with inert argon. After heat treatment, specimens were removed from the build plate with a band saw. The specimens were machined to the proper grip diameter using a lathe. The test sections were then ground and smoothed to a 10 Ra surface finish.

3.2.2 Material Characterization

The LPBF-printed Ti-6Al-4V material was characterized with X-ray computed tomography (XCT) and electron backscatter diffraction (EBSD) to investigate both porosity and grain morphology. Figure 45 shows an inverse pole figure of a printed specimen obtained via EBSD. The extracted section for analysis was a thin, disk-shaped cross-sectional slice taken from the grip section of a representative specimen.

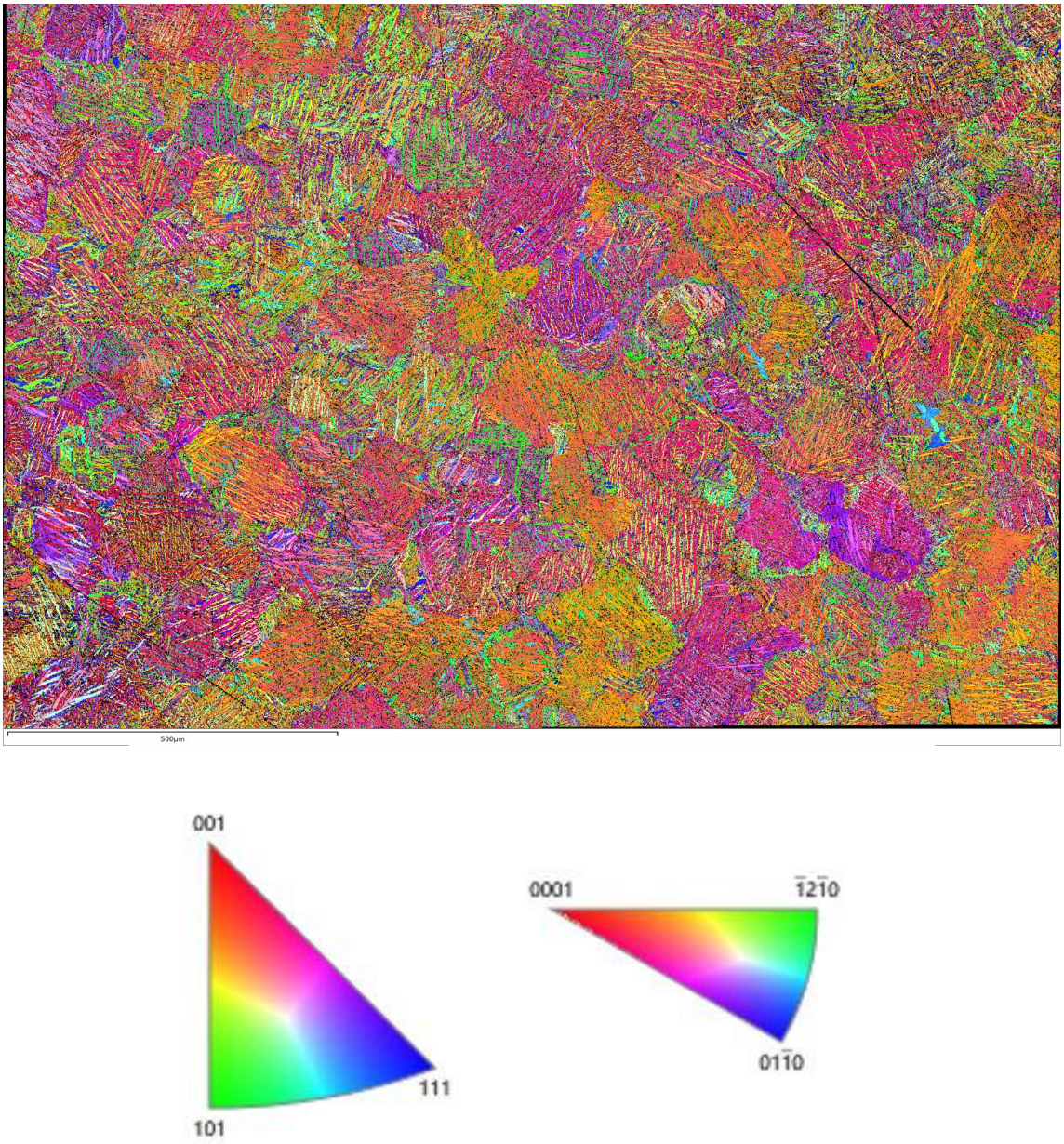

Figure 45: EBSD Map of LPBF AM Ti-6Al-4V; Miller Indices Denoting Crystallographic Orientations Shown below

The specimen surface was polished with a 0.05 μm colloidal silicon polish on a vibrating polisher. The EBSD map was constructed with a 75μm step size at a 700X magnification using an Oxford Instruments (Ultim Max & Symmetry Camera) and a Thermoscientific Apreo C Microscope. The map was construct with 36 images in a 6x6 mat. The specimen was grounded

with a piece of copper tap to reduce electron noise during imaging. Based on the cross section, it is probable that columnar grain structures travel through the direction of the build, in this case in and out of plane. This observation agrees with the columnar grain structure observed in previous characterizations of LPBF Ti-6Al-4V (Figure 7).

3.2.3 Axisymmetric Specimen Designs

The specimens investigated in our ductile fracture experiments for LPBF AM Ti-6Al-4V follow from the axisymmetric series developed in Section 2.4.2 and are shown in Figure 46 through Figure 51. All solid models and orthographic projections were generated using 3D CAD software (SolidWorks, 2019 version, Dassault Systemes, Waltham, MA); dimensions in all drawings are in millimeters. SG5 (Figure 46) has a straight gage section so that, when the specimen is loaded uniaxially, the state of stress in the gage is pure tension. SG6 through SG10 (Figure 47 through Figure 51) have notched, tapered gage sections so that, when the specimens are loaded uniaxially, the state of stress at the gage center departs from pure tension.

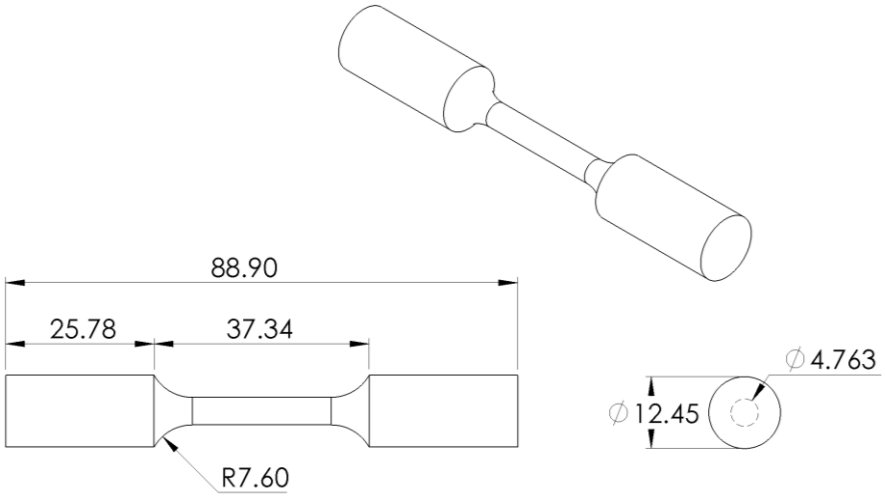

Figure 46: AM Ti-6Al-4V SG5 Orthographic Projections

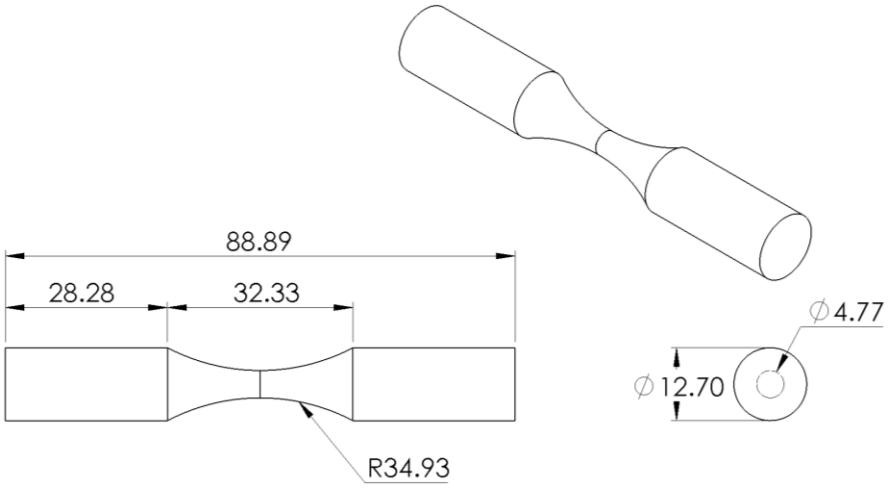

Figure 47: AM Ti-6Al-4V SG6 Orthographic Projections

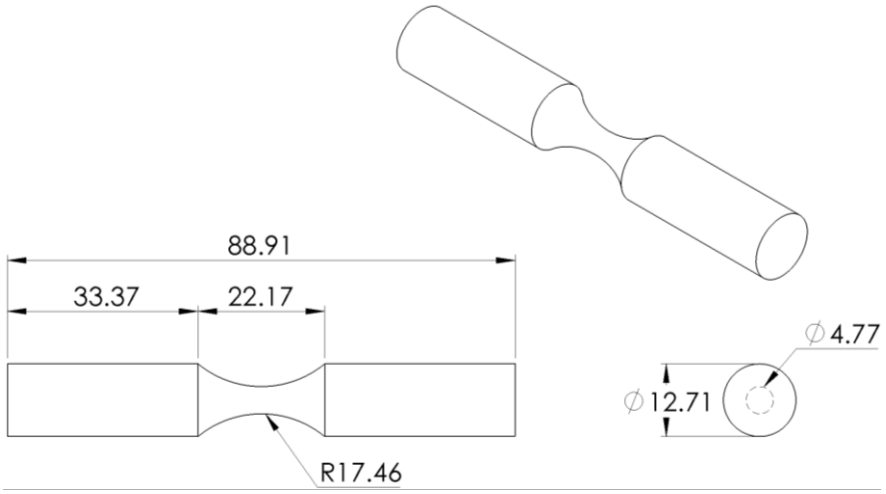

Figure 48: AM Ti-6Al-4V SG7 Orthographic Projections

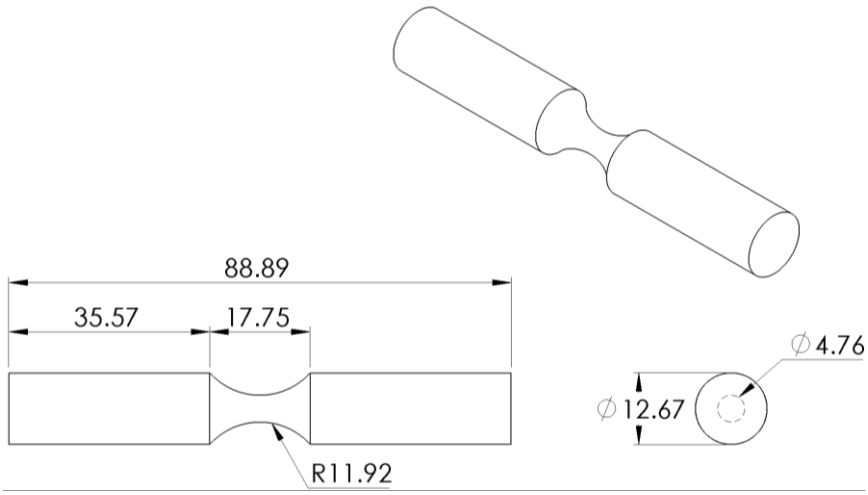

Figure 49: AM Ti-6Al-4V SG8 Orthographic Projections

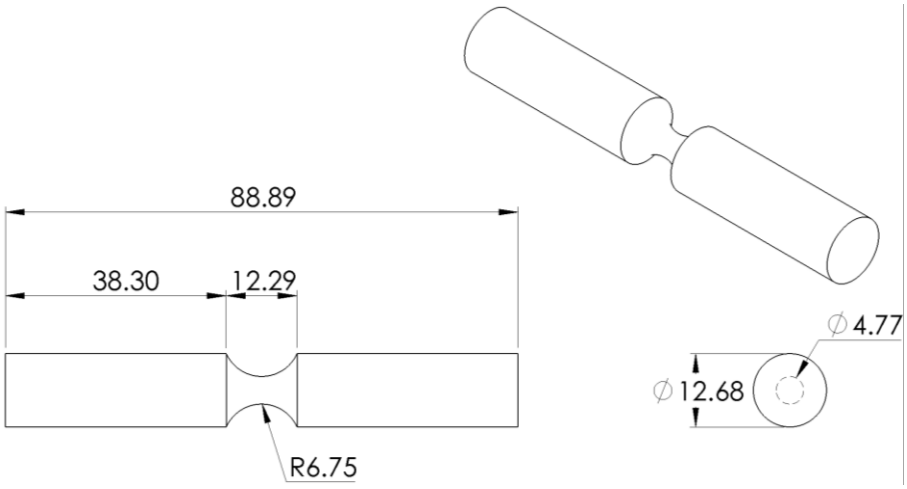

Figure 50: AM Ti-6Al-4V SG9 Orthographic Projections

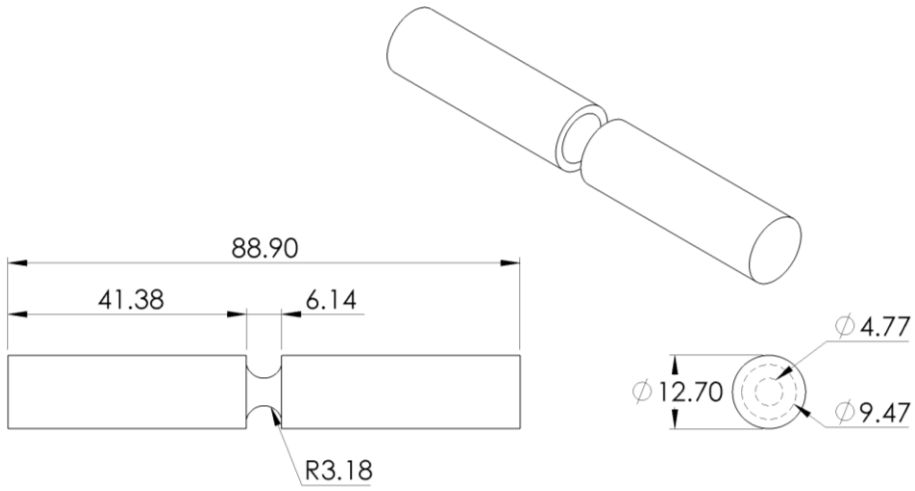

Figure 51: AM Ti-6Al-4V SG10 Orthographic Projections

3.2.4 Specimen Metrology Details

Inherent error in post-build machining generally leads to a mismatch between nominal and as-machined dimensions. It is imperative that as-machined dimensions be used throughout all pre- and post-processing methods, as inconsistencies can lead to scaling errors in force-displacement plots generated by the finite element simulations. As-built specimen dimensions were measured using a non-contact optical 3D measurement system (VR-3000, KEYENCE, Itasca, IL). The optical measurement system generates a topographical scan of an object placed within its field of view, allowing for accurate measurements along any point in the topography. Prior to optical measurement, the specimen gage sections were lightly sprayed with non-aqueous wet developer aerosol (SKD-S2, Magnaflux, Glenview, IL) to reduce the effects of polished metal reflecting light, leading to an unwanted reduction in scanning accuracy. For each specimen, three diameter measurements were taken in both the gripped (wide) sections as well as the center of the gage (reduced) section, then averaged. A lengthwise measurement was also taken across the specimen. The length of the gripped sections was assumed to be the same as the nominal dimensions in Figure 46 through Figure 51, from which the gage length was backed out.

3.2.5 Mechanical Testing

All quasi-static uniaxial tension tests were performed on a custom-built MTS 858 tabletop servo-hydraulic load frame. The load frame was equipped with a MTS #609 10A-01 load cell for axial force measurement. MTS 647 hydraulic wedge grips with 0.5-inch round wedges were used for specimen gripping. Continuous analog force data was recorded throughout the tests using a MTS FlexTest60 controller. All tests were executed in displacement control to achieve a nominal quasi-static strain rate $\dot{\varepsilon} =$ 1E-4 1/s, with actuator velocities v (in mm/s) calculated using:

$$v = L_c(\dot{\varepsilon}) \tag{22}$$

where the characteristic length L_c (in mm) is taken to be the gage length for specimens with smooth, unnotched reduced sections and the gauge arc radius/diameter for notched specimens. Note that this nominal quasi-static strain rate is a targeted "characteristic" strain rate that will vary both spatially and temporally during the test, especially after localization. Five tests were performed for each specimen type (SG5-SG10). Table 4 displays the actuation velocities for all tested specimen groups.

Table 4: Actuation Velocities for Axisymmetric Specimen Groups

Specimen No.	Taget Strain Rate (1/s)	Gage Length (in)	Notch Diameter (in)	Actuator Velocity (in/s)
SG5	0.0001	0.95	***	0.000095
SG6	0.0001	***	2.75	0.000275
SG7	0.0001	***	1.374	0.0001374
SG8	0.0001	***	0.94	0.000094
SG9	0.0001	***	0.53	0.000053
SG10	0.0001	***	0.25	0.000025

Prior to executing the test series, the load train was aligned using the MTS 609 alignment fixture (Figure 52, left). The fixture can be adjusted angularly and concentrically under full preloading; this reduces error induced by the preloading process. Alignment was achieved by placing and gripping a strain-gaged specimen within the wedge grips of the load frame. A computer loaded with MTS 709 alignment software generated readings for the bending strain imposed on the specimen in the form of three graphical points (Figure 52, right). The location of these graphical

points was adjusted by increasing or decreasing the torque in the adjustment bolts. Ultimately, the graphical points were adjusted to fall within a 5% bending strain envelope, the required resolution for a Class 5 alignment.

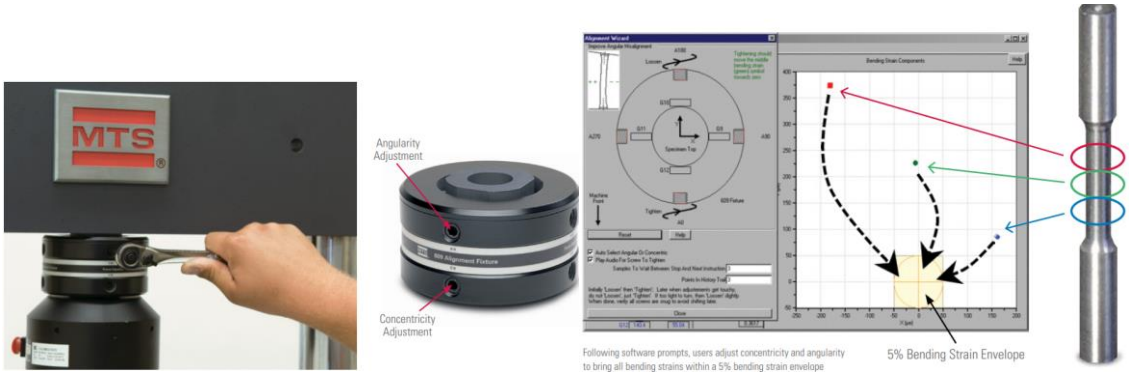

Figure 52: (Left) MTS 609, (Right) MTS 709 Alignment wizard [50]

3.2.6 Digital Image Correlation

Digital image correlation (DIC) was used to measure the full-field strain on the surface of the specimens, allowing for the resolution of deformation gradients and strains in localizations (such as necking and shear bands). DIC is a non-contact, optical strain measurement technique that tracks the motion of a high-contrast speckle pattern applied to the specimen gage. In preparation for speckle application, each specimen's gage section was cleaned with acetone or isopropyl alcohol to remove superficial surface impurities. Then a base layer of white spray paint was applied to the surface. This layer covered slightly more than 180° of the circumference of the specimen's gage section. The base layer was left to dry for several minutes, then a fine sparse black layer of paint was applied using an airbrush. These paint droplets are referred to as facets. Holding the airbrush farther away from the specimen during painting gave greater control over how many paint droplets were applied to the test section. This process resulted in a high-contrast, randomized speckle pattern (Figure 53). Each specimen underwent mechanical testing soon after both layers of paint were applied to prevent the paint from cracking as the specimen deforms.

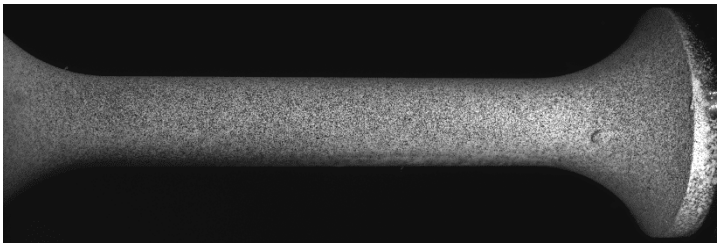

Figure 53: Example of DIC Speckle on SG5 Specimen

To capture the motion of the applied speckle pattern, two high-performance 8-megapixel cameras (Point Grey) with Schneider XNP 50-mm lenses were used. The test setup was equipped with polarization lenses and films to reduce the effect of light reflection during the test. One camera acted as the primary imaging source, and the second was oriented at a stereo angle to "perform 3D photogrammetry in addition to image correlation" [51]. The calibration of both cameras involved capturing images of a ceramic calibration target in varying positions within the field of view of both cameras. "This precisely calculates the cameras' intrinsic and extrinsic parameters while triangulating the cameras' positions and removing lens distortions. This removes any measurement bias and defines a three-dimensional coordinate system on the specimen's surface." [52] The calibration file was stored for testing and used for post-processing. Importantly, the calibration file specifies the resolution of the picture in units of pixel/mm, which is essential for determining the mesh size in each simulation. Ideally, the benefit of matching the element size to the VSG is so the elements of the mesh will average strain over the same surface area.

Once the specimen was secured in the hydraulic wedge grips of the MTS load frame, the cameras were lined up to target the geometric center of the specimen. The cameras' exposure time was adjusted as necessary to ensure the picture was clear, and the image was not too bright or overexposed. Lastly, the subset and step sizes of the image were adjusted to minimize error during correlation. The subset size is the area in which a group of facets are analyzed throughout the duration of the test. These facet groups need to be distinctive enough in order to be properly tracked. The step size determines the spacing of analyzed points. The step size is typically one quarter of the subset size and directly correlates to how many pixels are skipped over before they are analyzed

in any direction [53]. The subset size was adjusted based on the uncertainty within the image (Figure 54). If there is a large amount of uncertainty, then a larger subset size is required. Larger subset sizes can reduce the accuracy of the test, hence why the application of a quality speckle is vital. Subset and step size for each test are reported in Table 5.

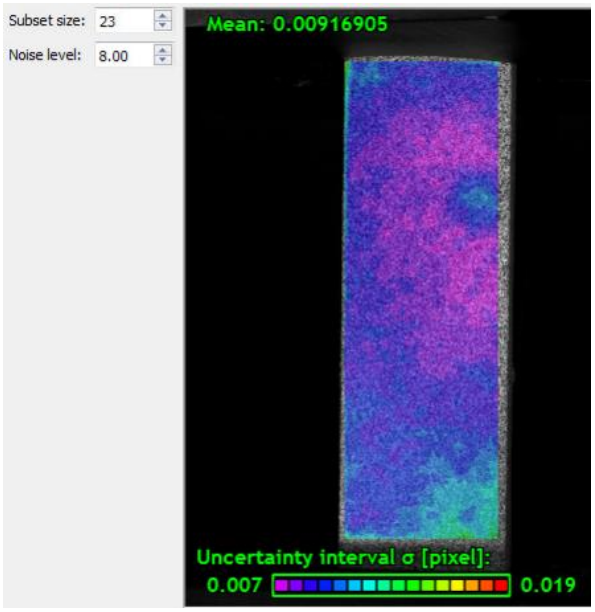

Figure 54: Example of Uncertainty Gradient in DIC Speckle [53]

Once mechanical testing concluded, the camera images for each experiment were correlated using three-dimensional digital image correlation software (VIC-3D, Correlated Solutions, v.7, Irmo, SC). The user-defined region of interest was selected to be the gage section of each tensile specimen. The correlation used the same subset size and step size used during the test. The DIC software computes displacements, strains, and other deformation measures within the correlated area. When calculating a desired deformation measure, the user is asked to select a filter size. This filter determines the value of any single point in the gradient by applying a Gaussian low-pass logarithmic filter around the point. The radius of the filter is determined by the multiplication of the filter size and the step size. Filter size for each test is reported in Table 5.

After the desired strain measure is calculated with the selected filter, a virtual strain gauge (VSG) was placed at the region of highest longitudinal strain in the image just prior to final fracture.

The size of the VSG was chosen to be similar to that of mesh size chosen for the wrought Ti-6Al-4V simulations performed in Chapter 2. The shape of the VSG was square (1:1 aspect ratio) to replicate the shape of the finite elements in the numerical simulations. A virtual extensometer (VE) was also placed in the region of interest. By creating the finite element mesh first, the DIC VE was placed so that its endpoints correspond to the nodes in the pre-generated finite element mesh (i.e., the DIC VE length and location were dictated by the length and location of the VE in the simulation). VSG and VE sizes for each test are reported in Table 5.

Table 5: DIC Information

Spec No.	Cal File	Subset	Step	Filter 1	Pixel/mm	No. Pixels	VSGL	VEL	F#	Seconds/Image
SG5_1	Cal Axial	61	15	23	0.20223	28	0.20223	16.8896	16.5	0.15
SG5_2	Cal Axial	33	8	23	0.20223	28	0.20223	18.096	16.5	0.15
SG5_3	Cal Axial	61	15	23	0.20223	28	0.20223	16.8896	16.5	0.15
SG5_4	Cal Axial	61	8	23	0.20223	28	0.20223	8.448	16.5	0.15
SG5_5	Cal Axial	61	15	23	0.20223	28	0.20223	18.096	16.5	0.15
SG6_1	Cal Axial Hourglass	61	15	23	132.574	28	0.2112	23.0817	16.5	0.3
SG6_2	Cal Axial Hourglass	33	8	23	132.574	28	0.2112	23.1533	16.5	0.5
SG6_3	Cal Axial Hourglass	51	12	23	132.574	28	0.2112	20.81594	16.5	0.5
SG6_4	Cal Axial Hourglass	33	8	23	132.574	28	0.2112	21.53094	16.5	0.5
SG6_5	Cal Axial Hourglass	33	8	23	132.574	28	0.2112	11.5473	16.5	0.15
SG7_1	Cal Axial Hourglass	33	8	23	132.574	28	0.2112	12.43142	16.5	0.5
SG7_2	Cal Axial Hourglass	33	8	23	132.574	28	0.2112	12.40482	16.5	0.5
SG7_3	Cal Axial Hourglass	33	8	23	132.574	28	0.2112	12.34946	16.5	0.5
SG7_4	Cal Axial Hourglass	33	8	23	132.574	28	0.2112	12.3705	16.5	0.5
SG7_5	Cal Axial Hourglass	33	8	23	132.574	28	0.2112	12.40334	16.5	0.5
SG8_1	Cal Axial Hourglass	33	8	23	132.574	28	0.2112	10.04144	16.5	0.25
SG8_2	Cal Axial Hourglass	33	8	23	132.574	28	0.2112	9.80556	16.5	0.25
SG8_3	Cal Axial Hourglass	33	8	23	132.574	28	0.2112	10.0136	16.5	0.25
SG8_4	Cal Axial Hourglass	33	8	23	132.574	28	0.2112	9.83414	16.5	0.25
SG8_5	Cal Axial Hourglass	33	8	23	132.574	28	0.2112	10.02742	16.5	0.25
SG9_1	Cal Axial Hourglass	33	8	23	132.574	28	0.2112	8.30114	16.5	0.25
SG9_2	Cal Axial Hourglass	33	8	23	132.574	28	0.2112	8.35998	16.5	0.25
SG9_3	Cal Axial Hourglass	33	8	23	132.574	28	0.2112	8.2006	16.5	0.25
SG9_4	Cal Axial Hourglass	33	8	23	132.574	28	0.2112	8.2836	16.5	0.25
SG9_5	Cal Axial Hourglass	33	8	23	132.574	28	0.2112	8.29288	16.5	0.25
SG10_1	Cal Axial Hourglass	33	8	23	132.574	28	0.2112	3.7223	16.5	0.25
SG10_2	Cal Axial Hourglass	33	8	23	132.574	28	0.2112	3.6915	16.5	0.25
SG10_3	Cal Axial Hourglass	33	8	23	132.574	28	0.2112	3.89196	16.5	0.25
SG10_4	Cal Axial Hourglass	33	8	23	132.574	28	0.2112	3.71662	16.5	0.25
SG10_5	Cal Axial Hourglass	33	8	23	132.574	28	0.2112	3.77034	16.5	0.25

3.3 Finite Element Simulations

Numerical simulations of mechanical tests outlined in Section 2.3 were performed in LS-DYNA® (version R9.3D, Ansys/LST, Livermore, CA). Prior to finite element analysis, 3D solid models of the test specimens were rendered in SolidWorks (2019 version, Dassault Systemes, Waltham, MA) using exact measured dimensions of the as-built geometries. Solid models were exported to the finite element grid generation software HyperMesh (2017.1 version, Altair, Troy, MI). Specimens were meshed using solid 3D hexahedron, 8-node elements with a characteristic length based on the VSG lengths shown in Table 5. Each meshed specimen was divided into three parts denoted by red, yellow, and green element colors (Figure 55).

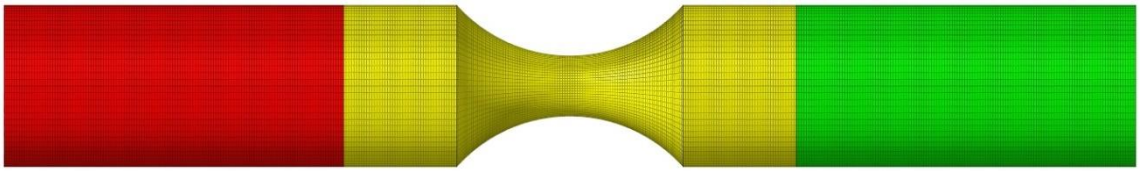

Figure 55: Representative Finite Element Mesh for SG8 Specimen

The green and red components are modeled to be representative of the section of the specimen tab that are clamped within the hydraulic wedge grips. It is good practice for these components to occupy 75% of the specimen tabs [47]. The center (yellow) component serves as the deformable material that will be studied for stress-state characterization.

Once the mesh was generated, it was exported to LS-PrePost® (version R4.7.22, Ansys/LST, Livermore, CA) as an include (.in) file. The input deck originally used for simulations in Chapter 2 was modified to take advantage of the LS-DYNA's massively parallel processing (MPP) solver, significantly reducing the computational expense. All elements within the model were assigned to be under-integrated constant-stress elements (ELFORM = 1). This element type increases efficiency and accuracy, but requires hourglass stabilization. Stiffness-based hourglass control (IHQ = 6) was assigned with an hourglass coefficient QH = 0.1. The specimen tabs are modeled as rigid elements using the *MAT_20 (*MAT_RIGID) material card from the LS-DYNA material library. The deformable area was modeled using the *MAT_024 elasto-plastic constitutive model developed by Hoover [42] for LPBF AM Ti-6Al-4V (vertical build only). This material model couples isotropic linear elastic deformation with post-yield viscoplastic deformation specified via a series of user-defined strain hardening curves (effective true stress vs. effective true plastic strain) at varying strain rates.

The motion of the gripped sections of the specimen were limited via the center of mass constraint flag (CMO = 1) in *MAT_20. An additional input of *MAT_20 are its constraint parameters CON1 and CON2. For the fixed grip, the constraint parameters CON1 = CON2 = 7 so that all translational and rotational degrees of freedom were constrained. For the actuated grip, CON1 = 5 and CON2 = 7 so that only axial translation is permitted. The actuator speed was

assigned with a *BOUNDARY_PRESCRIBED_MOTION_RIGID card. The rate of the actuator was kept at a constant ("artificial") speed of 1 m/s. All hardening curves within the *MAT_024 material card were suppressed except the quasi-static strain rate of 1E-4 1/s, which was the targeted nominal strain rate during testing. A rate-independent material model reduces computational costs due to the ability to impose a larger ("artificial") actuator speed. The absence of inertial effects at the 1 m/s "artificial" actuator was confirmed in our simulations (e.g., no dynamically induced oscillations after simulation start-up) and follows best practices from previous simulations of wrought Ti-6Al-4V [37].

3.4 Results

3.4.1 Simulation vs. Experiment Verification

In each of our ductile fracture experiments, the stress and strain fields are inhomogeneous (non-uniform) in the specimen gage section, particularly after the onset of localization. Thus, the history of the state of stress (triaxiality and Lode parameter) and equivalent plastic strain are obtained using a hybrid experimental-numerical approach. For each experiment, measured data (e.g., force-displacement and principal surface strains) are compared to the corresponding results from the parallel numerical simulation in Section 3.3. Agreement between the simulation and the measured data implies that the simulation is adequately capturing the three-dimensional stresses and strains during the experiment. The simulation is then used to extract the history of the triaxiality and Lode parameter at the anticipated site of fracture initiation, the most highly strained element in the gage section.

For each specimen geometry (SG5-SG10) in the axisymmetric test series, simulation and experiment were compared using axial force vs. axial displacement curves and principal surface strains (maximum E1 and minimum E2) vs. displacement curves; see Figure 56 through Figure 61. Agreement between simulation and experiment was also assessed using contour plots of the principal surface strain fields just prior to fracture (Figure 62 through Figure 67). Note that the color scales from experiment in simulation match in Figure 62 through Figure 67. Of the five

tests/simulations conducted per specimen geometry, results for one representative test/simulation are shown in this chapter, with the remainder relegated to the Appendix.

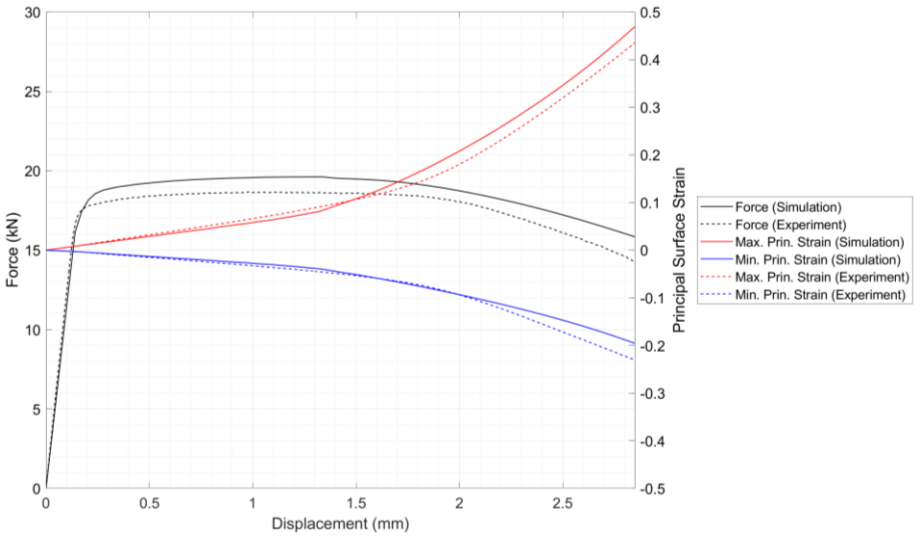

Figure 56: SG5 Test #4 (SG5_4) Force vs. Displacement (Left) and Principal Surface Strains (E1 – max, E2 – min) vs. Displacement (Right)

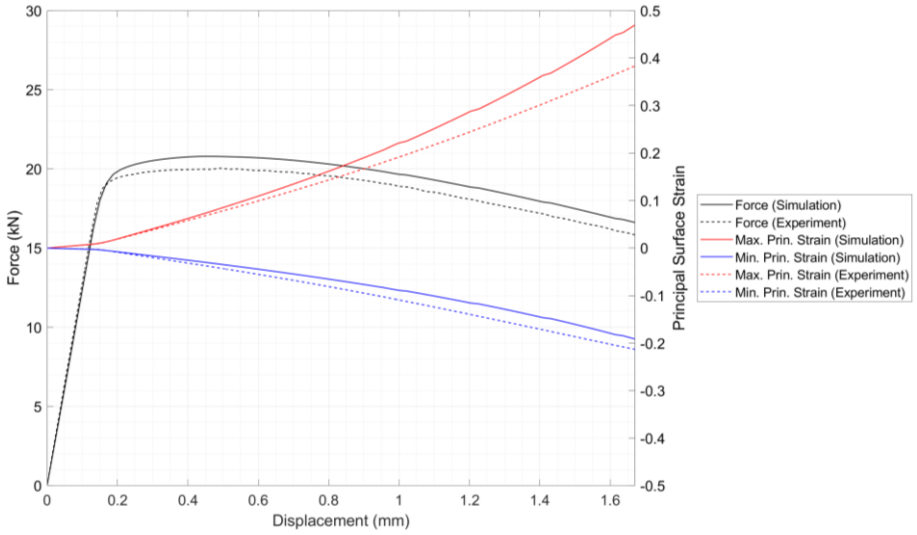

Figure 57: SG6 Test #1 (SG6_1) Force vs. Displacement (Left) and Principal Surface Strains (E1 – max, E2 – min) vs. Displacement (Right)

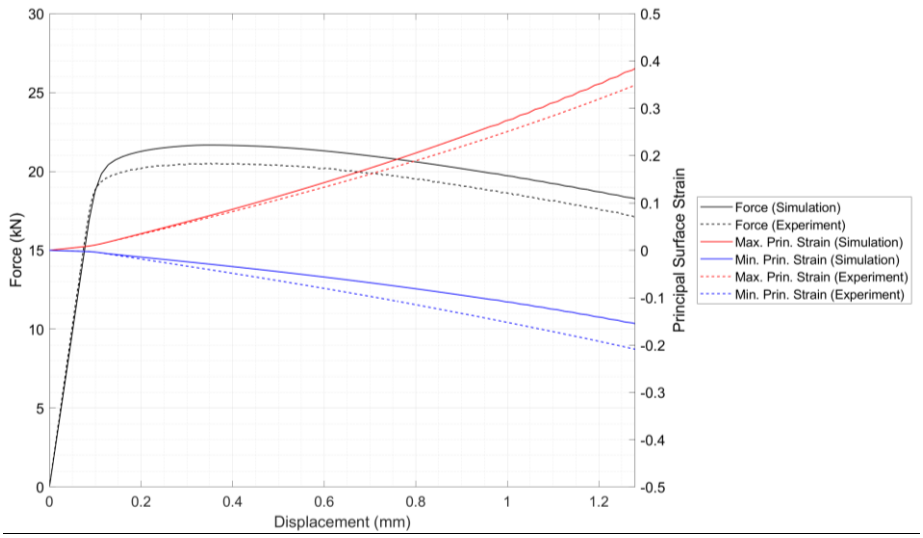

Figure 58: SG7 Test #1 (SG7_1) Force vs. Displacement (Left) and Principal Surface Strains (E1 – max, E2 – min) vs. Displacement (Right)

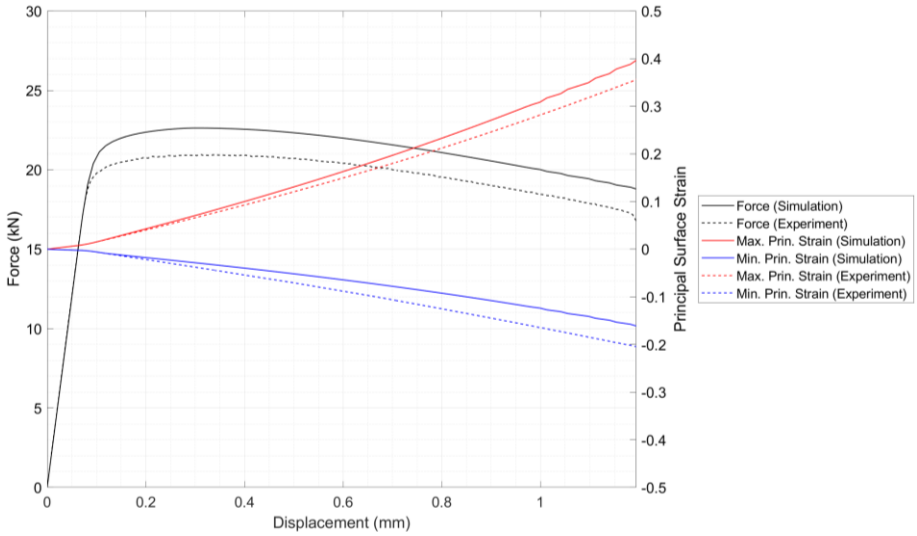

Figure 59: SG8 Test #1 (SG8_1) Force vs. Displacement (Left) and Principal Surface Strains (E1 – max, E2 – min) vs. Displacement (Right)

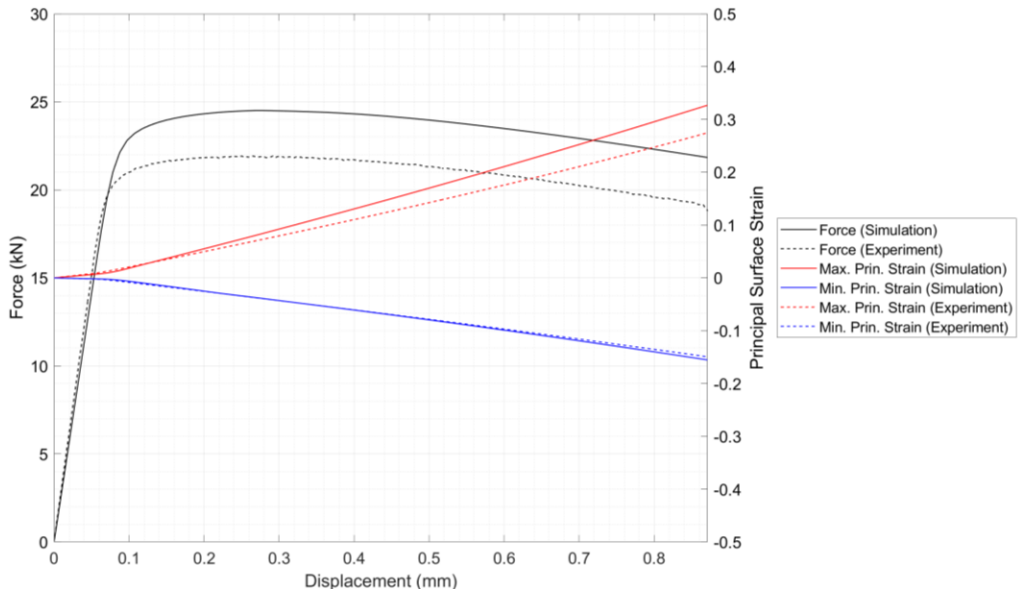

Figure 60: SG9 Test #1 (SG9_1) Force vs. Displacement (Left) and Principal Surface Strains (E1 – max, E2 – min) vs. Displacement (Right)

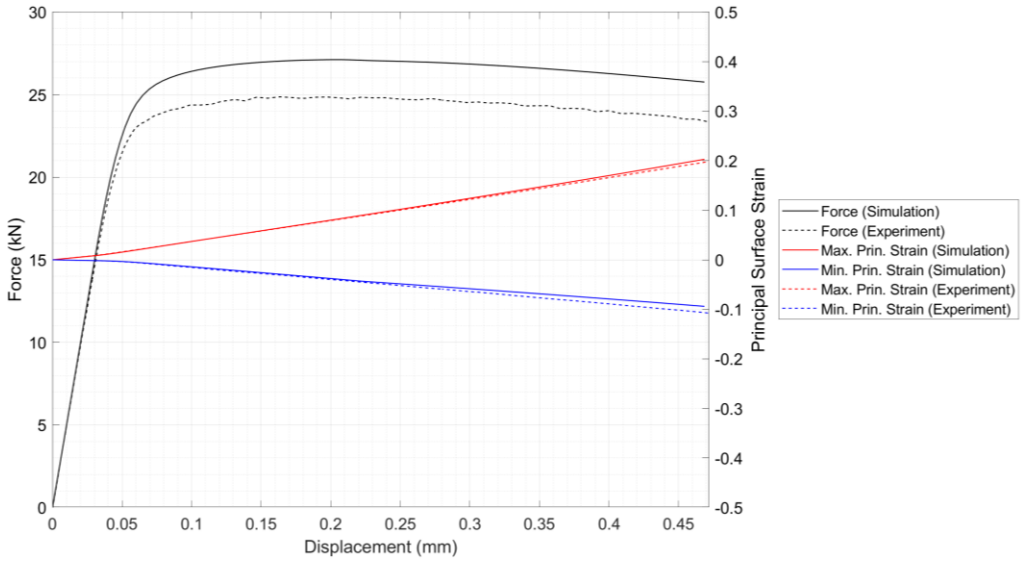

Figure 61: SG10 Test #1 (SG10_1) Force vs. Displacement (Left) and Principal Surface Strains (E1 – max, E2 – min) vs. Displacement (Right)

The following figures of principal surface strain fringe plots display both the DIC and FEA fringe plots. The scales were equivocated for both data sets and were placed between each respective fringe plot.

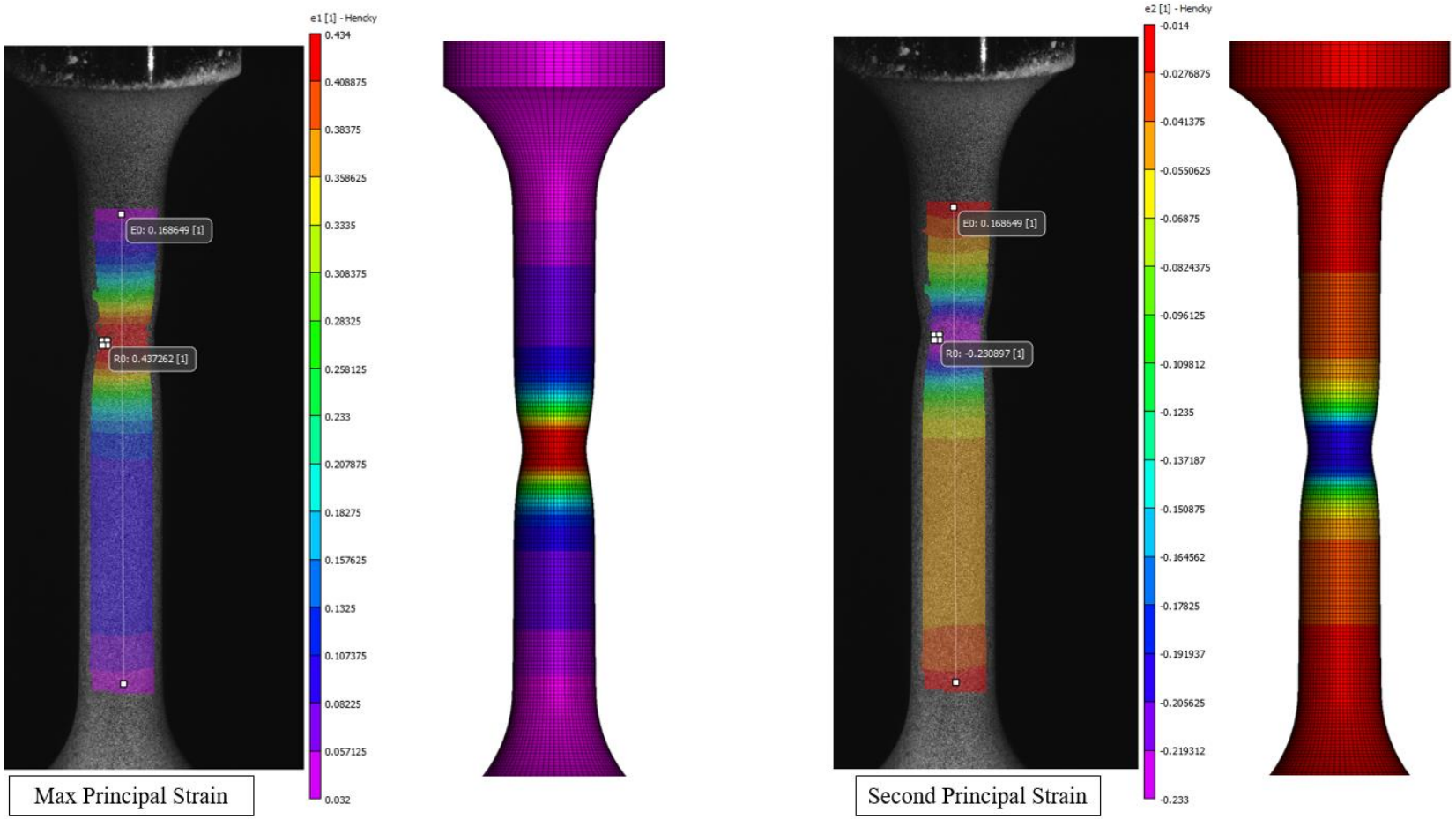

Figure 62: SG5_4 Principal Surface Strain Fringe Plots (Experimental vs. Simulation)

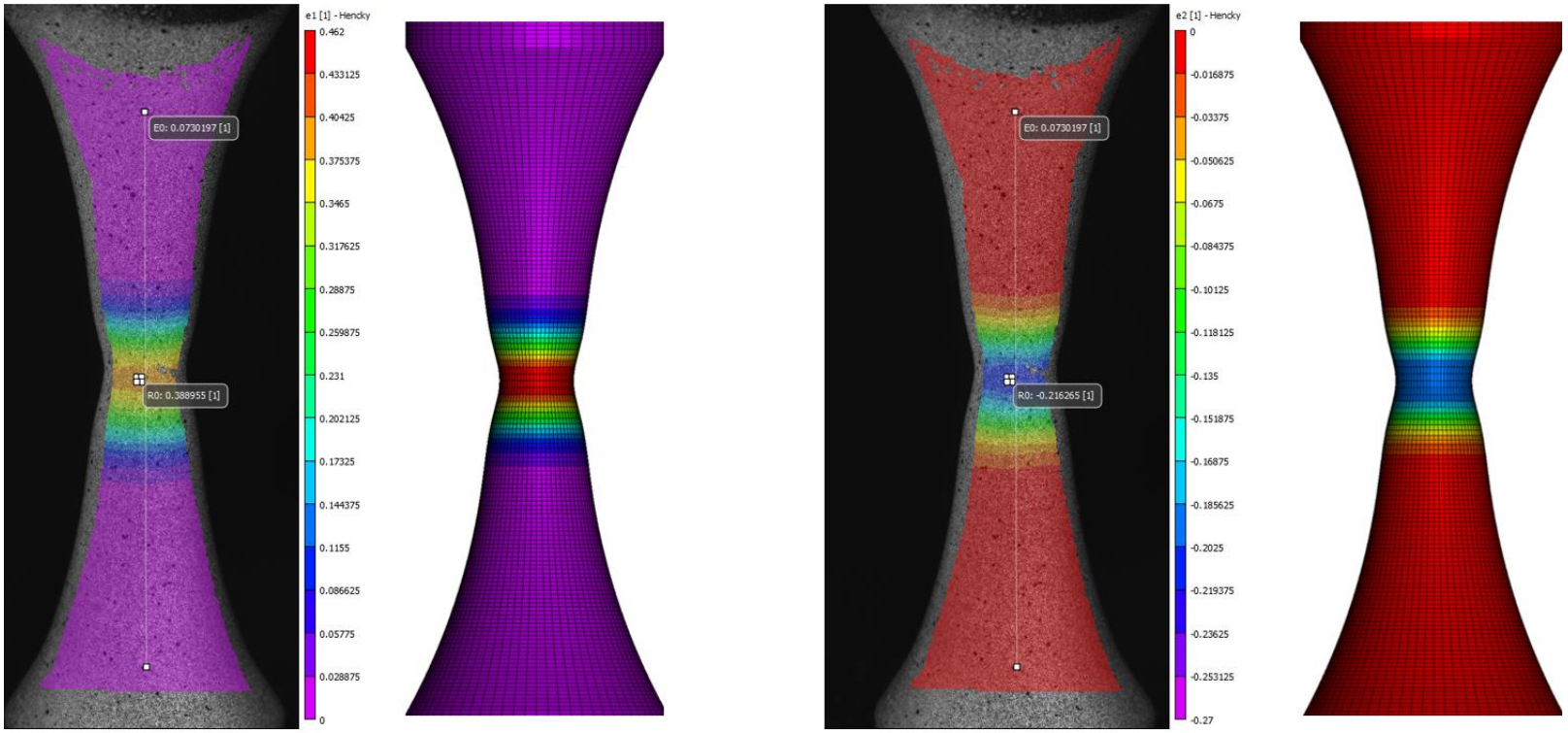

Max Principal Strain

Second Principal Strain

Figure 63: SG6_1 Principal Surface Strain Fringe Plots (Experimental vs. Simulation)

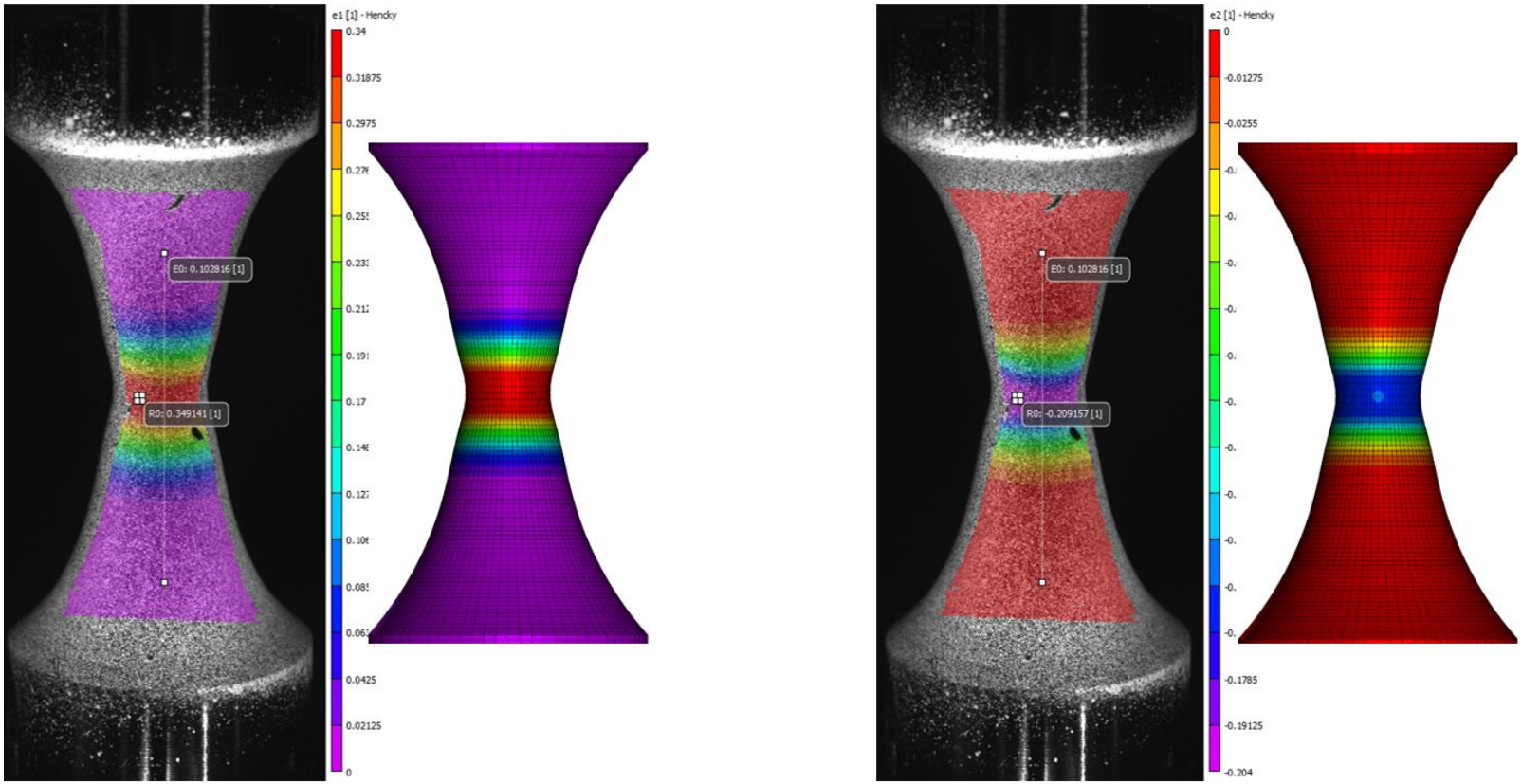

Max Principal Strain

Second Principal Strain

Figure 64: SG7_1 Principal Surface Strain Fringe Plots (Experimental vs. Simulation)

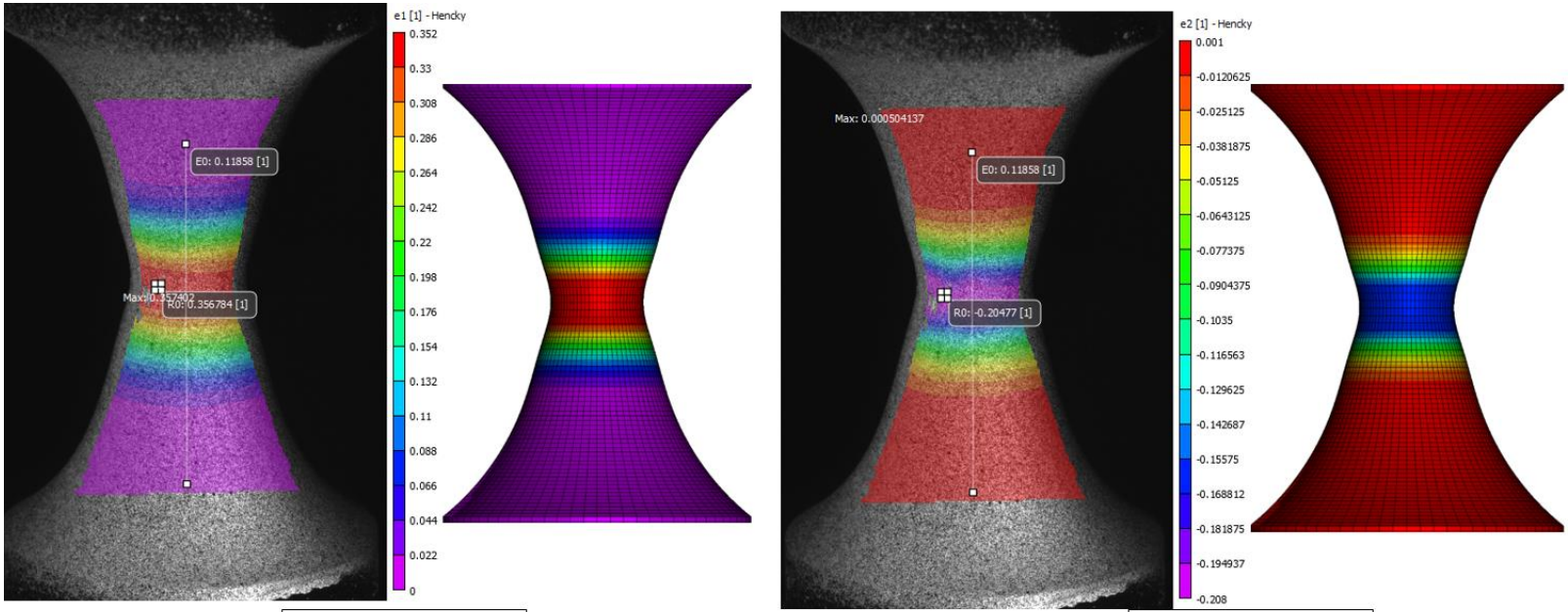

Max Principal Strain

Second Principal Strain

Figure 65: SG8_1 Principal Surface Strain Fringe Plots (Experimental vs. Simulation)

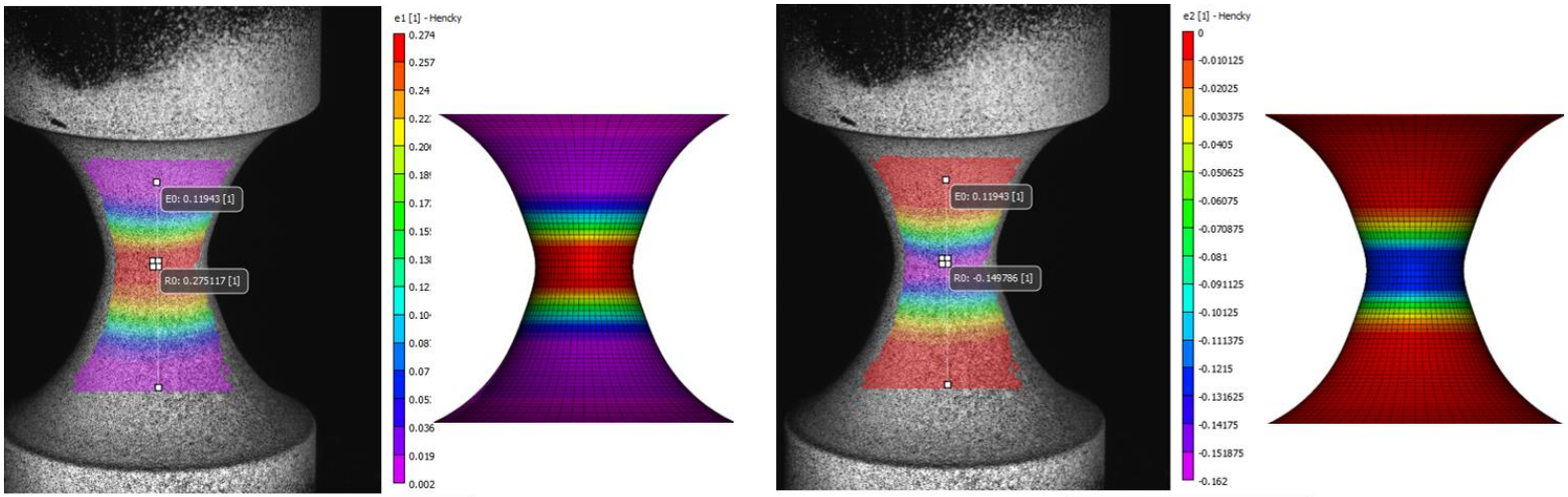

Max Principal Strain

Second Principal Strain

Figure 66: SG9_1 Principal Surface Strain Fringe Plots (Experimental vs. Simulation)

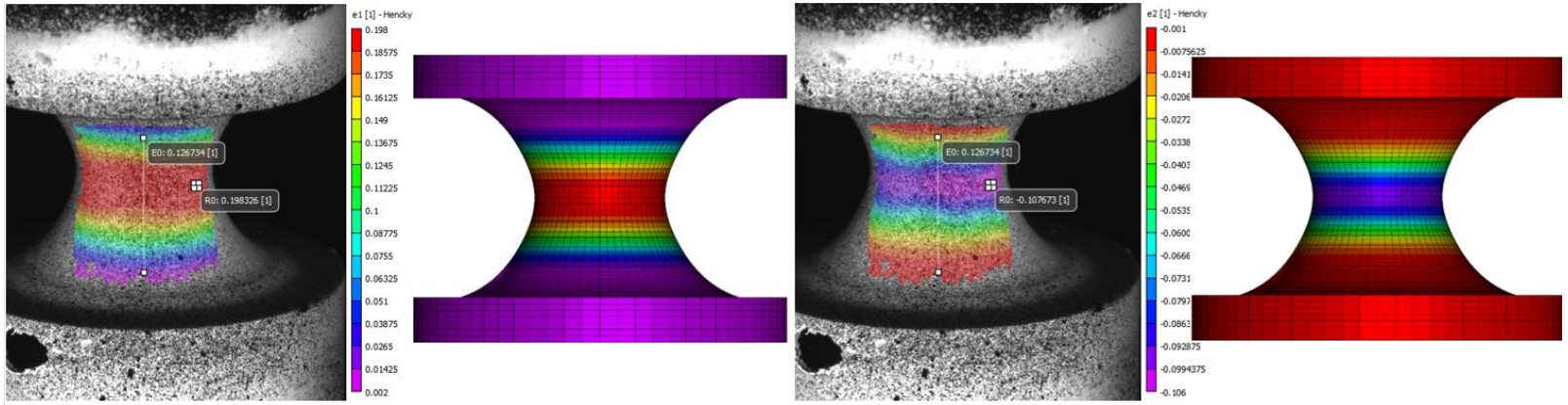

Figure 67: SG10_1 Principal Surface Strain Fringe Plots (Experimental vs. Simulation)

There is sufficient agreement between the simulations and experiments to extract the history of the state of stress (triaxiality and Lode parameter) from the numerical simulations throughout the test series. That said, discrepancies in the force vs. displacement and principal Hencky strains vs. displacement were observed, some significant. Although the simulated and experimental hardening behavior in the force vs. displacement plots agree very well, yield is consistently over-predicted in the simulations (slightly for SG6_1, Figure 57, and more egregiously for SG9_1, (Figure 60). Further, maximum principal surface strains are consistently over-predicted in the simulations (slightly for SG10_1, Figure 61, and more egregiously for SG6_1, Figure 57). Minimum principal surface strains are generally under-predicted in the simulations, with the exception of SG9_1 (Figure 60). Potential sources of error include:

- Specimen metrology: Dimensional inaccuracy can lead to "scaling errors" like those observed in the force vs. displacement plots.
- Strain rate discrepancies: The strain rate used in the material model (1E-4 1/s) may not reflect actual testing conditions in the ductile fracture experimental program. The simulated behavior is "stiffer," indicating the strain rate in the material model may be too high.
- Anisotropy: If an axisymmetric specimen is isotropic, then the transverse (off-axis) principal strains should be equal throughout the specimen's deformation history. Differences in transverse principal strains reported by DIC, a signature of anisotropy, can be deduced from Figure 58 and Figure 59 (assuming plastic incompressibility see section 3.4.2).
- Inconsistent material properties between the LPBF AM Ti-6Al-4V material used in the plasticity experiments and the ductile fracture experiments (specimens were fabricated in different builds, albeit with the same processing parameters and post-fusion heat treatment)

3.4.2 Stress State Values and Equivalent Plastic Strain at Fracture

As previously noted, there is acceptable agreement between the simulations and experiments to extract the history of the state of stress (triaxiality and Lode parameter) from the numerical simulations throughout the full test series. Figure 73 shows the evolution of triaxiality and Lode parameter during the specimen's plastic deformation history for representative SG5-SG10 tests. Stress states are extracted from the anticipated site of fracture initiation in the simulation, i.e., the most highly strained element in the gage section.

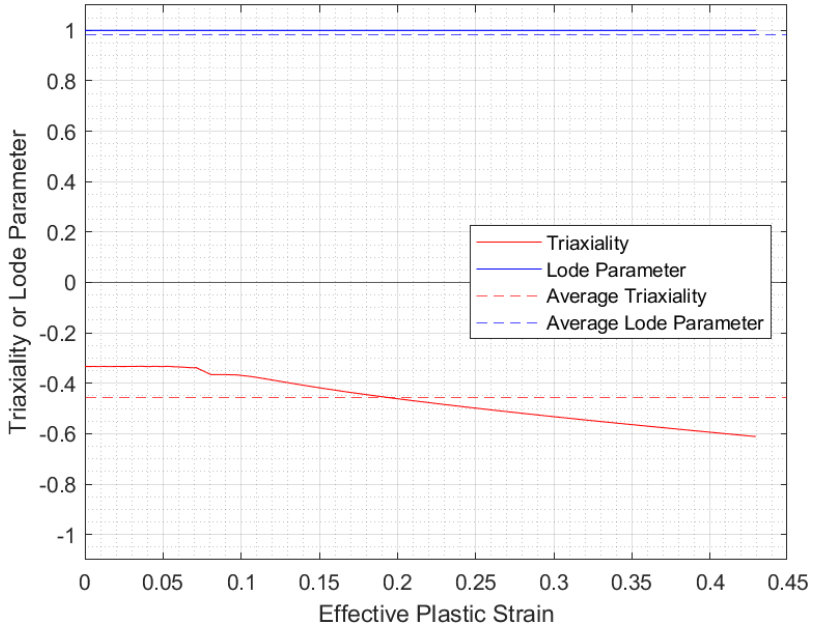

Figure 68: Representative Triaxiality and Lode Parameter Histories for SG5_4

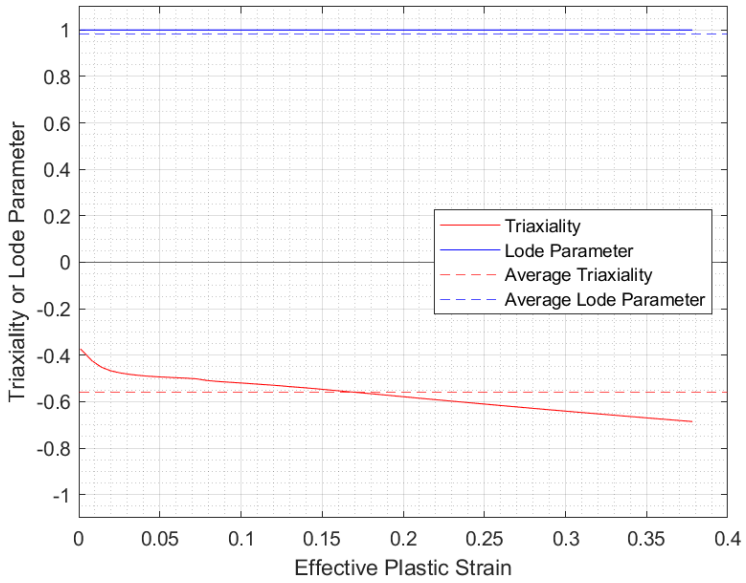

Figure 69: Representative Triaxiality and Lode Parameter Histories for SG6_1

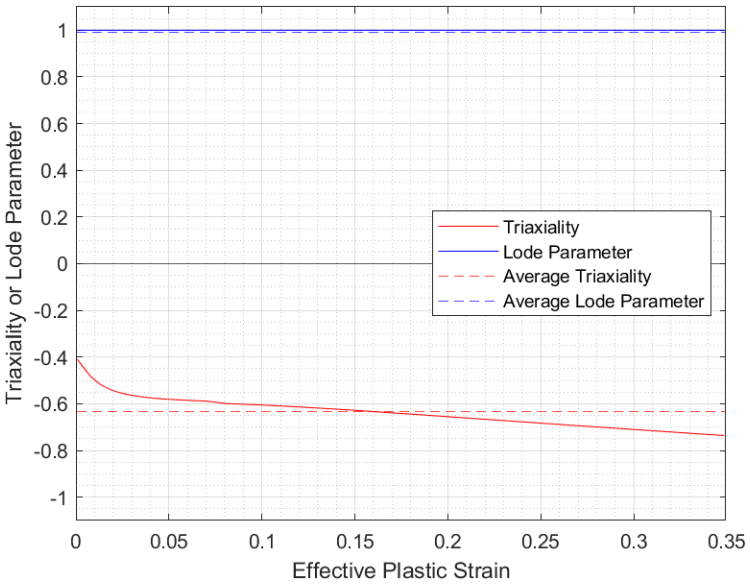

Figure 70: Representative Triaxiality and Lode Parameter Histories for SG7_1

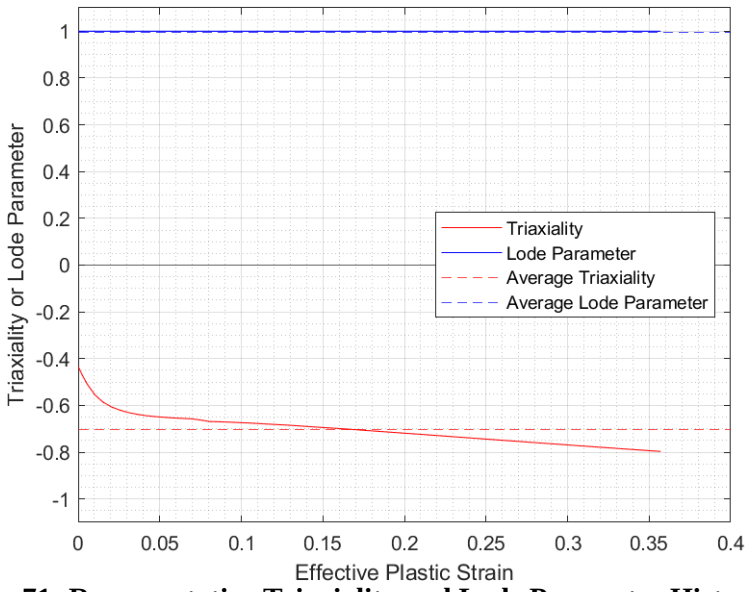

Figure 71: Representative Triaxiality and Lode Parameter Histories for SG8_1

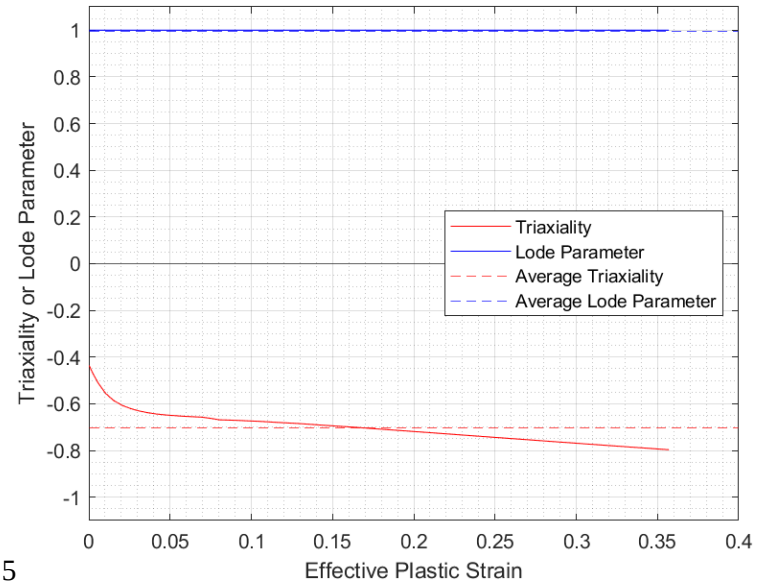

5

Figure 72: Representative Triaxiality and Lode Parameter Histories for SG9_1

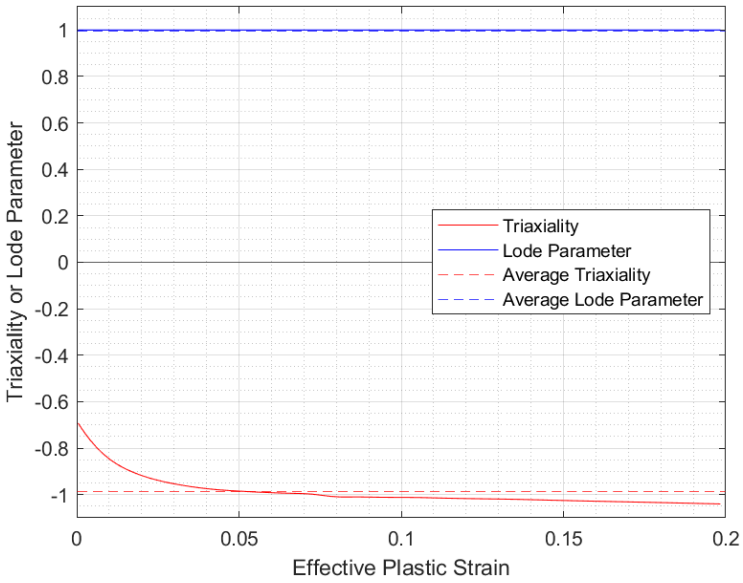

Figure 73: Representative Triaxiality and Lode Parameter Histories for SG10_1

Although the Lode parameter did not exhibit meaningful variations throughout the plastic deformation history, the triaxiality varied more significantly across all specimen geometries, particularly after the onset of necking (which occurs early in the plastic deformation history). Average values of the triaxiality and Lode parameter between the onset of plastic deformation and fracture were obtained using the weighted averages in Eqs. (19) and (20), with the effective plastic strain at fracture determined experimentally as follows.

From the DIC virtual strain gage, the maximum (longitudinal) and minimum (transverse) principal Hencky surface strains, ε_1 and ε_2, were obtained from the image prior to fracture. (Note that the DIC correlated strain field is only a two-dimensional surface map.) The usual assumption of isochoric (volume-preserving) plastic deformations and small elastic strains imposes the constraint that the trace of the Hencky strain tensor vanishes, so that the third principal Hencky strain, ε_3, can be found.

$$\varepsilon_3 = -(\varepsilon_1 + \varepsilon_2) \tag{23}$$

With all three DIC principal Hencky strain histories at the fracture location in hand, the effective true plastic strain at fracture, $\bar{\varepsilon}_p^f$, was determined as follows:

$$\bar{\varepsilon}_p^f = \sqrt{\frac{2}{3}(\varepsilon_1^2 + \varepsilon_2^2 + \varepsilon_3^2)} \tag{24}$$

Final values of the triaxiality, Lode parameter, and effective plastic strain at fracture – accounting for the five test/simulations performed for each specimen geometry – are reported in Table 6 as arithmetic means with corresponding standard deviations. A tabular presentation of these quantities test-by-test is provided in the Appendix.

Table 6: Stress State and Effective Plastic Strain (EPS) at Fracture (Mean ± Std. Dev.)

Spec. Geom.	Triaxiality	Lode Parameter	EPS at Fracture
SG5	-0.471±0.008	0.98±0.012	0.485±0.042
SG6	-0.569±0.010	0.984±0.004	0.409±0.025
SG7	-0.636±0.004	0.986±0.005	0.366±0.021
SG8	-0.686±0.009	0.984±0.006	0.335±0.021
SG9	-0.718±0.041	0.988±0.004	0.283±0.014
SG10	-0.976±0.011	0.988±0.006	0.205±0.021

The following figure is a visual representation of the average stress states for each specimen group where the lode parameter remains relatively constant due the tensile uniaxial loading.

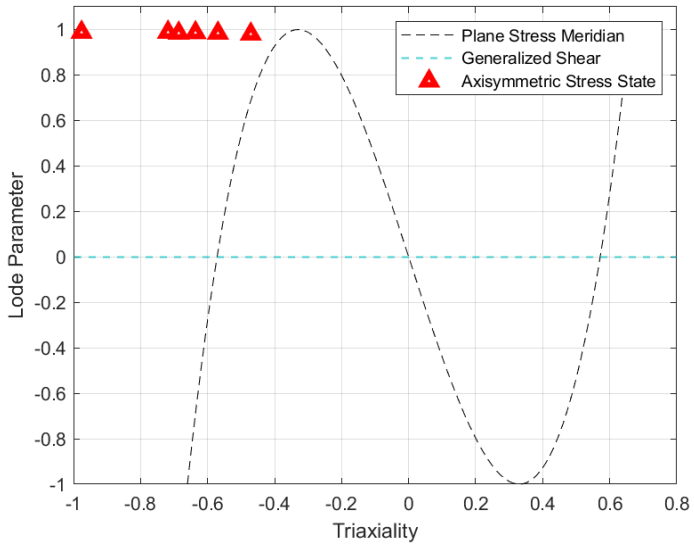

Figure 74: Experimental Axisymmetric Stress States within 2D Failure Map

Another graphical presentation of the two dimensional fracture locus is shown in Figure 75. Where the effective plastic strain at fracture is plotted against the triaxiality.

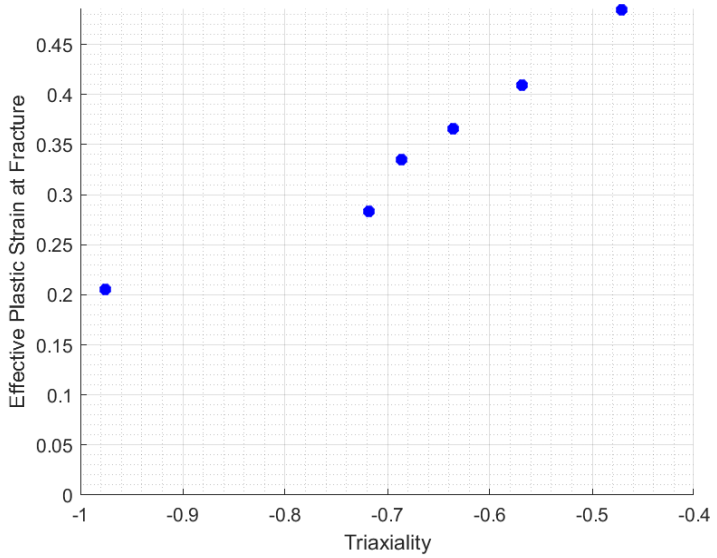

Figure 75: Experimental effective plastic strain at fracture vs. Triaxiality

When comparing the mean stress states in Table 6 for LPBF AM Ti-6Al-4V to those in Table 1 for wrought Ti-6Al-4V, no significant differences are observed in the reported Lode parameter values. However, meaningful differences are observed in mean triaxialities, with LPBF AM Ti-6Al-4V exhibiting stress states with lower, more negative (tensile) triaxialities. Further, substantial differences in effective plastic strain at fracture are reported, with LPBF AM Ti-6Al-4V exhibiting higher ductility at corresponding stress states. It is hypothesized that the higher fracture strains produced lower mean triaxiality values, as weighted averages persist over a larger portion of the post-necking plastic deformation history. The trend of effective plastic strain at fracture decreasing with an increasingly negative (tensile) triaxiality is consistent with a significant body of previous literature in the ductile fracture community.

The table presented below briefly exhibits the differences in reported values of EPS of AM Ti-6Al-4V from literature and the reported experimental values from this thesis. The round bar and round notched bar from [43] are closest to SG5 and SG8 respectively.

Table 7: Comparison of EPS Values (Experimental vs. Literature)

Eps Values of AM Ti-6Al-4V			
Experimental		Nalli et. al	
SG5	0.485	Round Bar	0.45
SG8	0.335	Round Notch Bar	0.27

3.4.3 Fractography

Figure 76 is an image from a Leica microscope showcasing the topology of a representative SG5 specimen fracture surface. The fracture surface appears to have the typical cup-and-cone behavior observed at negative (tensile) triaxialities. Craters along the surface, close to the center of the specimen, are surmised to be the result of microvoid coalescence. This fracture surface morphology was common throughout the full ductile fracture experimental program.

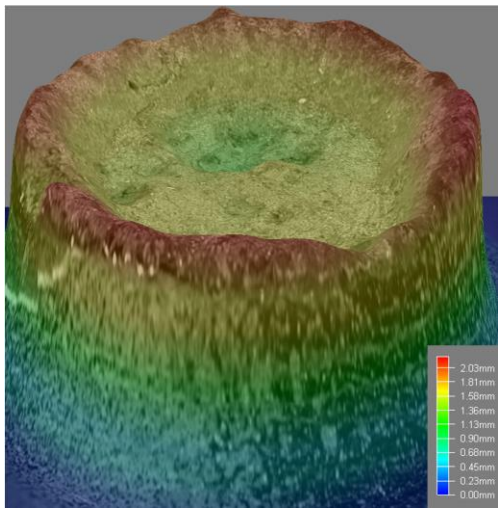

Figure 76: Representative Fracture Surface of AM Specimens.

CHAPTER 4

CONCLUSION

4.1 Reflections, Recommendations and Short-Term Next Steps

While the development of the tabulated ductile fracture locus is imperative to implementing an accurate FEA material model, it is also crucial that the initial methodology outlined in chapter 3 is executed both accurately and precisely. Therefore, in the best interest of future projects, it would be necessary to repeat the outlined methodology. However, several potential opportunities for improvement and refinement have been identified.

Discrepancy between simulation and experiment in Section 3.4. Discrepancies observed between simulation and experiment were attributed to several potential causes, including specimen metrology, strain rate effects, anisotropy, and the fabrication of plasticity and ductile fracture specimens in two different builds. In the short-term, it is recommended that all ductile fracture specimens be re-measured using digital calipers to confirm the dimensions reported using non-contact optical 3D measurements. Secondly, to mitigate potential strain rate discrepancies between simulation and experiment, it is recommended that all ductile fracture simulations be performed using LS-DYNA's implicit solver with the pair of viscoplastic hardening curves (at strain rates of 1E-4 and 1E-2 1/s) for LPBF AM Ti-6Al-4V reported in Ref. [42].

Through-thickness plastic strain gradient. At the time and region of fracture, a cross-sectional slice of the fracture plane of the specimen reveals there is generally a significant effective plastic strain gradient (Figure 77). This raises the possibility that the reported failure strain value from DIC, which comes from the surface of the specimen, may not be sufficient in assigning the plastic strain at fracture for a given stress-state. Therefore, if the plasticity model for the simulations is accurate, then the same element used for stress-state analysis can also be used to for the final strain at fracture.

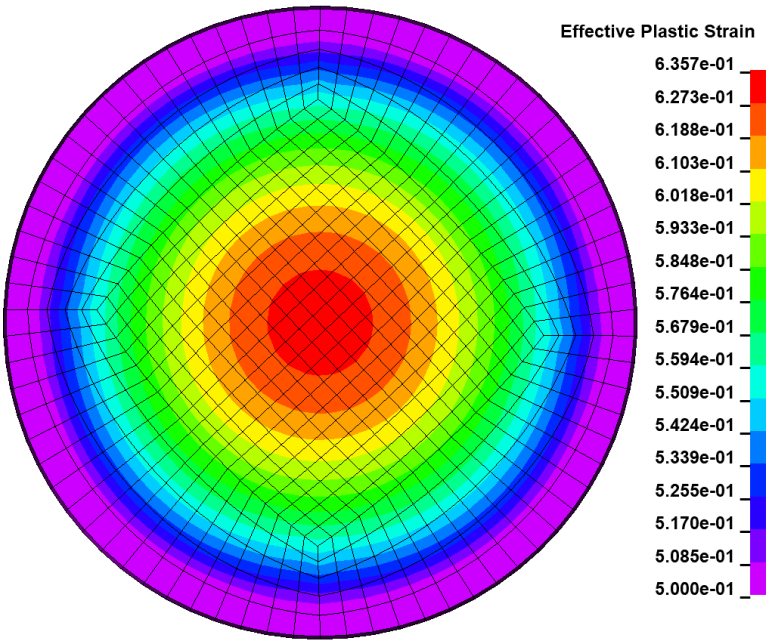

Figure 77: Cross-Sectional View of SG4_5 at Fracture Location

2nd principal strain vs. minimum principal strain. In order to acquire the principal Hencky strain vs. displacement plots shown in Section 3.4.2, history data for "max principal strain" and "2nd principal strain" were extracted from an element along the fracture line using LS-PrePost. The described history data from simulation was compared against the maximum and minimum principal Hencky surface strains from DIC. It was discovered that the "2nd principal strain" in LS-PrePost did not necessarily correlate to the minimum surface principal strain from DIC. This phenomenon was unexpected, as axisymmetric specimens were expected to have identical transverse (off-axis) principal strains, provided they exhibit isotropic (or transversely isotropic) response. In future work, it is recommended that all three DIC principal strains be calculated and ordered (from greatest to least). The minimum principal surface strain from DIC can then be properly correlated to either the "2nd principal strain" or "min principal strain" from the simulation.

Mesh effects. Regarding simulations, a mesh sensitivity analysis should be carried out to ensure the results of the simulations are not affected by a low-resolution mesh. It is possible that error may have arisen due to the cross-section of each mesh not being completely symmetrical. The mesh size itself was not entirely uniform throughout, leading to a more intense localization at the

core of each specimen. Therefore, it might be best to alter the meshing strategy for future simulations.

4.2 Longer-Term Future Work

Given the substantial interest surrounding additive manufacturing and the surprising lack of published research on the ductile fracture of LPBF Ti-6Al-4V and other additively manufactured aerospace metals, it would certainly be worth pursuing future investigations around this topic. Some ideas that should be taken into consideration when carrying out this project again in the future or one that is similar are discussed in what follows.

Another potential remedy for specimen geometry would be the use of a non-contact optical 3D scanning. These tools can both scan the geometry in its entirety and also create a mesh of the specimen. This would ensure greater accuracy throughout the metrology process and increae efficiency.

The mechanical tests were conducted under displacement control (constant actuator velocity) to achieve a targeted nominal strain rate, which did not take the effects of strain localization in the gage section potentially varying the strain rate throughout the test. If feasible, it would be beneficial to perform testing under strain rate control.

For future work, it is recommended that the plasticity specimens used to develop the constitutive model be fabricated during the same build as the ductile fracture specimens.

Another facet of a future project should be the development of more sophisticated material model (e.g., *MAT_224_GYS and *MAT_264) that is able to capture the effects of tension-compression yield asymmetry and build-orientation-induced plastic anisotropy, respectively.

Lastly, the value of a ductile fracture model is its ability to accurately calculate progressive damage (in each element at each time step) under a broad range of stress states (triaxiality and Lode parameter combinations). Therefore, experimentally investigating additional specimen geometries and loading conditions (plane stress tension, plane strain tension, tension-torsion, etc.) that enrich

the ductile fracture locus of LPBF AM Ti-6Al-4V would be advisable, so as to lead to higher-fidelity simulations when this model is employed in practice.

4.3 Scientific Contributions

The literature regarding LPBF AM Ti-64 ductile fracture is fairly sparse. Only over the last three to four years have rigorous investigations been conducted on the feasibility of developing accurate predictive model for AM Ti-6Al-4V. The 2D map failure map shown in the figure below produced by Heid et al [39] is the result of an investigation for various stress states in various instances of multiaxial tension. The work conducted in this thesis was envisioned to be supplemental to the literature by investigating axisymmetric stress states and failure strains in specimens of the same AM alloy using a hybrid experimental numerical approach as seen in Figure 78.

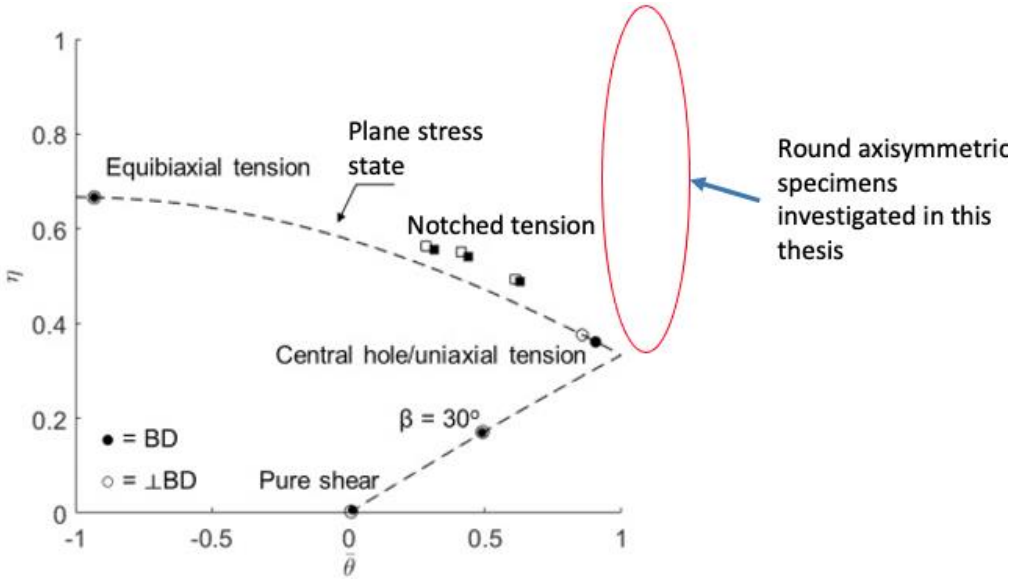

Figure 78: Existing 2D fracture locus for AM Ti-6Al-4V [39]

REFERENCES

[1] Ansys/LST, “LS-DYNA”, URL https://www.lstc.com/products/ls-dyna. Accessed April 19, 2021.

[2] Reporting Wildlife Aircraft Strikes, AC 150/5200-32B, U.S. Department of Transportation and Federal Aviation Administration, AAS-300, Office of Airport Safety and Operations - Airport Safety & Operations Division, May 31, 2013.

[3] Cleary, E.C., and Dolbeer, R.A., "Wildlife Hazard Management at Airports: A Manual for Airport Personnel" (2005). USDA National Wildlife Research Center - Staff Publications. 133.

[4] Marra, P.P., Dove, C.J., Dolbeer, R., Dahlan, N.F., Heacker, M., Whatton, J.F., Diggs, N.E., France, C. and Henkes, G.A. “Migratory Canada geese cause crash of US Airways Flight 1549,” Frontiers in Ecology and the Environment, Vol. 7, No. 6, pp. 297-301.

[5] Tulis, D., “Pilots, Crew, Passengers Celebrate 2009 ‘Hudosn Miracle’ Damaged Airbus is Carolinas Aviation Museum Centerpiece”, URL https://www.aopa.org/news-and-media/all-news/2019/january/16/crew-and-passengers-celebrate-2009-hudson-miracle-flight. Last modified January 16, 2019. Accessed April 19, 2021.

[6] Loss of Thrust in Both Engines After Encountering a Flock of Birds and Subsequent Ditching on the Hudson River US Airways Flight 1549 Airbus A320-214, DCA09MA026 , 490 L’Enfant Plaza, S.W. Washington, D.C. 20594, U.S. National Transportation Safety Board, June 9, 2009.

[7] Pilot’s Handbook of Aeronautical Knowledge FAA-H-8083-25B, U.S. Department of Transportation and Federal Aviation Administration; P.O. Box 25082, Oklahoma City, OK 73125, 2016, pp. 7-22.

[8] NTSB. Left Engine Failure and Subsequent Depressurization, Southwest Airlines Flight 1380, Boeing 737-7H4, N772SW, Philadelphia, Pennsylvania, April 17, 2018. Aircraft Accident Report AAR-19/03. November 2019, Accessed 19, 2021.

[9] Insurance Institute for Highway Safety, “About our tests”, https://www.iihs.org/ratings/about-our-tests#verification, Accessed April 19, 2021

[10] Wu, S.R., Cheng, J., “Advanced development of explicit FEA in automotive applications”, *Computer Methods in Applied Mechanics and Engineering*, Computer Methods in Applied Mechanics and Engineering, Oct 1997 Vol. 149, No. 1-4, pp. 189-199.

[11] Barbat, B., Li, X., Prasad, P., *A Comparative Analysis of Vehicle-To-Vehicle and Vehicle -To-Rigid Fixed Barrier Frontal Impacts*, Ford Motor Company, USA. June 2001.

[12] Ansys/LST, “Metal Forming Application”, URL:https://www.lstc.com/applications metal_forming. Accessed April 19, 2021.

[13] Valberg, H. S., Applied Metal Forming Including FEM Analysis, Cambridge University Press N.Y. USA., 2010, pp. 1, 34.

[14] Alia-Novobilski, M., “Embracing Opportunity: Additive Technology for Manufacturing”, URL:https://www.wpafb.af.mil/News/Article-Display/Article/1043404/embracing-%20opportunity-additive-technology-for-manufacturing/, Last modified January 6, 2017. Accessed April 19, 2021.

[15] Han, P., Additive Design and Manufacturing of Jet Engine Parts, Engineering, November 2017, Vol. 3, No. 5, pp. 648-652.

[16] Han, J.-C., Dutta, S., and Ekkad, S., Gas Turbine Heat Transfer and Cooling Technology, 2nd ed. 2013: CRC Press Taylor & Francis Group 6000 Broken Sound Parkway NW, Suite 300 Boca Raton, FL, pp. 25.

[17] Badum, L., Leizeronok, B., and Cukurel, B., "New Insights from Conceptual Design of an Additive Manufactured 300 W Microgas Turbine Toward Unmanned Aerial Vehicle Applications." ASME. *J. Eng. Gas Turbines Power*. February 2021; Vol. 143, No. 2.

[18] ASTM, “Additive Manufacturing Overview”, URL: https://www.astm.org/industry/additive-manufacturing-overview.html, Accessed April 19, 2021.

[19] T. DebRoy, H.L. Wei, J.S. Zuback, T. Mukherjee, J.W. Elmer, J.O. Milewski, A.M. Beese, A. Wilson-Heid, A. De, W. Zhang, "Additive manufacturing of metallic components – Process, structure and properties", *Progress in Materials Science*, March 2018, Vol. 92, pp. 112-224.

[20] Herzog, D., Seyda V., Wycisk, E., Emmelmann, C., "Additive Manufacturing of Metals"*Acta Materialia*, Vol. 117, September 2016, pp. 371-392.

[21] Ducato, A., Fratini, L., La Cascia, M., Mazzola, G., "An Automated Visual Inspection System for the Classification of the Phases of Ti-6Al-4V Titanium Alloy", 2013.

[22]Gorji, M.B., Tanconge-Dejean, T., Mohr, D., "Heterogeneous random medium plasticity and fracture model of additively-manufactured Ti-6Al-4V", *Acta Materialia,* Feburary 2018 pp. 442-455

[23] Antonysamy, A.A., Meyer, J., Prangnell P.B., "Effect of Build Geometry On The B-Grain Structure and Texture in Additive Manufacture Of Ti6Al4V By Selective Electron Beam Melting", *Materials Characterization,* Vol. 84, 2013, pp. 153-168.

[24] Zukas J.A. Impact Dynamics. Wiley, New York, 1982. pp. 11.

[25] McClintock, F.A. "A Criterion for Ductile Fracture by the Growth of Holes." *ASME J. Appl. Mech.* Vol. 35 No. 2, 1968 pp. 363–371.

[26] Rice, J.R., Tracey, D.M., "On the ductile enlargement of voids in triaxial stress fields." *J. Mech. Phys. Solids*, Vol. 17, No. 3, 1969 pp. 201–217.

[27] Gurson, A.L., "Continuum theory of ductile rupture by void nucleation and growth. Part I: Yield criteria and flow rules for porous ductile media." *J. Eng. Mater. Technol.* Vol. 99 No. 1, 1969, pp. 2–15 1977.

[28] Tvergaard, V., Needleman, A., "Analysis of the cup-cone fracture in a round tensile bar." *Acta Metall.* Vol. 32, 1984, pp. 157–169.

[29] Benzerga, A.A., Leblond, JB., Needleman, A. "Ductile failure modeling". Int J Fract 201, 29–80 (2016).

[30] Johnson, G.R., “Materials Characterization for Computations Involving Severe Dynamic Loading”, *Proc. Army Symp. on Solid Mechanics*, 1980, Work in Progress, Cape Cod, Massachusetts, Sept. 1980, pp. 62-67.

[31] Johnson, G.R., Cook, W.H., “Fracture characteristics of three metals subjected to various strains, strain rates, temperatures and pressures.” *Eng. Fract. Mech,* Vol. 21, No. 1, 1985, pp. 31–48.

[32] Mackenzie, A.C., Hancock, J.W., Brown, D.K., “On the influence of state of stress on ductile failure initiation in high strength steels.” *Eng. Fract. Mech.* Vol. 9, No. 1, 1977, pp. 167–188.

[33] Bao, Y., Wierzbicki T., “On fracture locus in the equivalent strain and stress triaxiality space.” *Int. J. Mech. Sci.* Vol. 46, No. 1, 2004, pp. 81–98.

[34] Barsoum, I., Faleskog, J., “Rupture mechanisms in combined tension and shear — Experiments.” *Int. J. Solids Struct.* Vol. 44, No. 6, 2007, pp. 1768–1786

[35] Danas K., Castañeda P.P., “Influence of the Lode parameter and the Stress triaxiality on the Failure of Elasto-Plastic Porous Materials”. *International Journal of Solids and Structures*, Vol. 49, 2012, pp. 1325-1342.

[36] Hammer, J.T., Plastic Deformation and Ductile Fracture of Ti-6Al-4V Under Various Loading Conditions. Graduate Thesis, The Ohio State University, 2012.

[37] Haight, S., Wang L., Du Bois, P., Carney, K., Kan, C-D. “Development of Titanium Alloy Ti-6Al-4V. U.S. Department of Transportation Federal Aviation Administration Air Traffic Organization Operations Planning Office of Aviation Research and Development, DOT/FAA/TC-15/23, May 2016.

[38] *MAT_224 User Guide, LS-DYNA Aerospace Working Group, 2017.

[39] Alexander E. Wilson-Heid, Allison M. Beese, Fracture of Laser Powder Bed Fusion Additively Manufactured Ti–6Al–4V Under Multiaxial Loading: Calibration and Comparison of Fracture Models, *Materials Science and Engineering: A*, Vol. 761, July 2019.

[40]Lai, W.M., Rubin, D., Krempel, E., Introdution To Continuum Mechanics 4th ed., Elsevier, Massachusetts, 2010.

[41] Onaka, S. “Appropriateness of the Hencky Equivalent Strain as the Quantity to Represent the Degree of Severe Plastic Deformation”, Materials Transactions, Vol. 53, No. 8, 2012, pp. 1547-1548.

[42] Hoover, L.D., “Large Strain Plastic Deformation of Traditionally Processed and Additively Manufactured Aerospace Metals”. Graduate Thesis, University of Dayton, 2021.

[43] Nalli, F., Cortese, L., Concli, F., Ductile Damage Assessment of Ti-6Al-4V, 17-4PH and AlSi10Mg for Additive Manufacturing, Engineering Fracture Mechanics, 2021 Vol. 241

[44]Ansys/LST, “What Are the Differences Between Implicit and Explicit”, URL: https://www.dynasupport.com/faq/general/what-are-the-differences-between-implicit-and-explicit, Accessed April 20, 2021.

[45] Spulak, N., Lowe, R.L., J.D. Seidt, A. Gilat, C.K. Park, K.S. Carney, Ductile Fracture Under In-Plane Biaxial Tension and Out-of-Plane Compression, *International Journal of Solids and Structures*, 2020, Vol. 202, pp. 234-242

[46] Seidt, J.D., Plastic Deformation and Ductile Fracture of 2024-T351 Aluminum Under Various Loading Conditions. Ph.D. Dissertation, The Ohio State University, 2010

[47] Lowe, R.L., Hoover, L.D., Negri, C.A. “Experimental Design for Negative Triaxialities: Ductile Fracture Under Combined Uniaxial Tension and Hydrostatic Pressure.” *16th LS-DYNA Users Conference*®, 2020.

[48] Concli F., Gilioli A., Nalli F. Experimental–numerical assessment of ductile failure of Additive Manufacturing selective laser melting reticular structures made of Al A357. Proceedings of the Institution of Mechanical Engineers, Part C: Journal of Mechanical Engineering Science. March 2019.

[49] ASTM International. F2924-14 Standard Specification for Additive Manufacturing Titanium-6 Aluminum-4 Vanadium with Powder Bed Fusion. West Conshohocken, PA; ASTM International, 2014.

[50] MTS, "MTS Alignment Solution Ensure the accuracy and reliability of test system data", https://www.mts.com/cs/groups/public/documents/library/dev_002709.pdf, Accessed May 23, 2021.

[51] International Digital Image Correlation Society: Standardization, Good Practices, and Uncertainty Quantification Committee, "A Good Practices Guide for Digital Image Correlation" URL: https://idics.org/guide/DICGoodPracticesGuide_ElectronicVersion-V5g-181022.pdf , last modified October, 2018. Accessed May 23, 2021.

[52] Correlated Solutions, "DIC Calibration", URL: https://www.correlatedsolutions.com/calibration/, Accessed May 24, 2021.

[53] Correlated Solutions, "Vic-3D V7 Ref. Manual URL: http://www.correlatedsolutions.com/supportcontent/Vic-3D-v7-Manual.pdf, Accessed May 24, 2021.

[54] MIT Open Courseware "Lecture 12: Fundamental Concepts in Structural Plasticity" URL: https://ocw.mit.edu/courses/mechanical-engineering/2-080j-structural-mechanics-fall-2013/course-notes/MIT2_080JF13_Lecture12.pdf. Accessed June 8, 2021

APPENDIX A

Supplemental Data

Material Certification

The following figure was used to qualify the powder for the AM build.

AP&C
A GE Additive Company

3765 La Vérendrye, suite 110, Boisbriand, Quebec, Canada, J7H 1R8
Tel. (+1) 450.434-1004; Fax: (+1) 450-434-1200
www.advancedpowders.com

F-002 Rev.1
Page 1 of 1

MATERIAL CERTIFICATE No: MC-20-1095

Customer:	University of Dayton, RI-Energy Technologies & Materials Div., River Road Facility, 2610 East River Road, Dayton, OH 45439-1534, United States.		
Purchase Order:	P2014869	**Internal Order:**	GEA75415 Rev.1
Material Description:	Ti-6Al-4V grade 5 powder	**Laboratory No:**	LIMS_01
Size:	15-53 µm	**Lot #:**	201-G0001
Specification:	ASTM F2924	**Quantity:**	40 kg

POWDER COMPOSITION (weight percent)				
Element	**ASTM F2924**	**Measured**	**Testing method**	**Status**
Aluminum, range	5.50 - 6.75	6.34	ASTM E2371	Conforming
Vanadium, range	3.50 - 4.50	3.92	ASTM E2371	Conforming
Iron, max.	0.30	0.19	ASTM E2371	Conforming
Oxygen, max.	0.20	0.17	ASTM E1409	Conforming
Carbon, max.	0.08	0.02	ASTM E1941	Conforming
Nitrogen, max.	0.05	0.01	ASTM E1409	Conforming
Hydrogen, max.	0.015	0.002	ASTM E1447	Conforming
Yttrium, max.	0.005	< 0.001	ASTM E2371	Conforming
Others each, max.	0.10	< 0.10	ASTM E2371	Conforming
Others total, max.	0.40	< 0.40	ASTM E2371	Conforming
Titanium	Balance	Balance		
Chemical analysis laboratory: Luvak Inc. (722 Main Street, Boylston MA, 01505). Report 0-89674				

POWDER CHARACTERIZATION			
Description	**Required**	**Measured**	**Status / Comments**
Particle size distribution per ASTM B214			
Particle Size (µm)	**% By Mass**	**% By Mass**	
> 53	Report	3.2	NA
≤ 53	Report	96.8	NA
Particle size distribution per ASTM B822 (Coulter® LS Particle Size Analyzer)			
D_{10}	Report	21 µm	NA
D_{50}	Report	38 µm	NA
D_{90}	Report	52 µm	NA
< 15 µm	Report	4 % by volume	NA
Flow Rate per ASTM B964 (Carney)			
Flow Rate (sec. for 50 g)	Report	7.6	NA
Apparent Density per ASTM B417 (Carney)			
Apparent Density (g/cm³)	Report	2.56	NA
Analyses were done by AP&C at their location and reported results are rounded following ASTM E29.			
We hereby certify that the above values conform to the requirements of Purchase Order P2014869			

2020-12-16

Date | **Quality department**

Figure 79: Material Certification for AM-Ti-6Al-4V Powder

Force vs. Displacement & Principal Surface Strain vs. Displacement Plots

The figures contained in this section are the force vs. displacement and principal surface strain vs. displacement plots for the remainder of the mechanical test specimens.

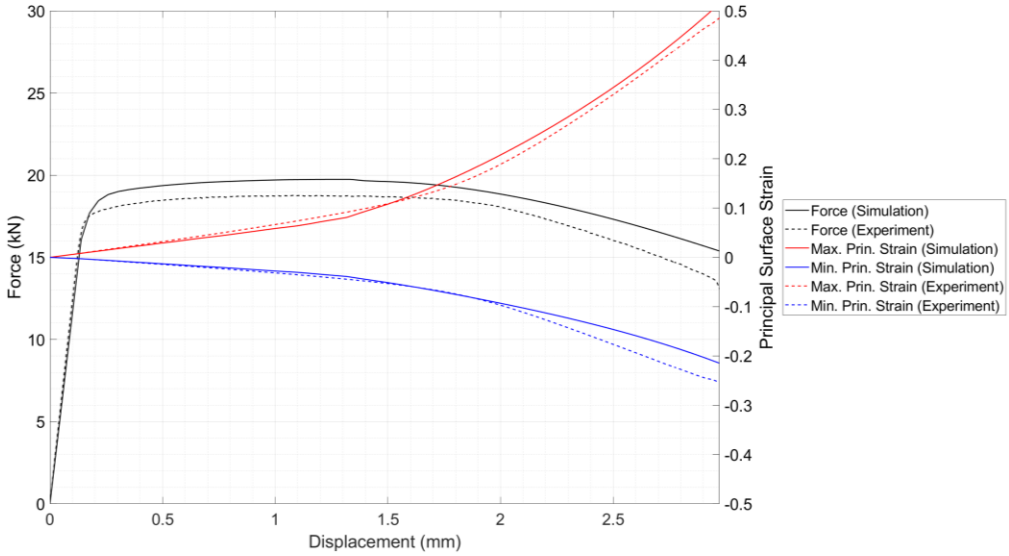

Figure 80: SG5 Test #1 (SG5_1) Force vs. Displacement (Left) and Principal Surface Strains (E1 – max, E2 – min) vs. Displacement (Right)

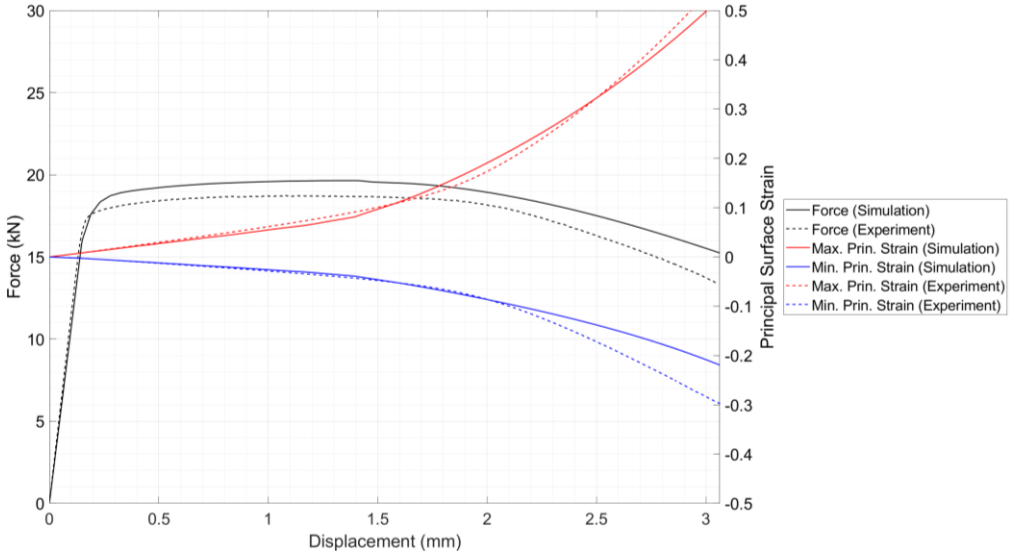

Figure 81: SG5 Test #2 (SG5_2) Force vs. Displacement (Left) and Principal Surface Strains (E1 – max, E2 – min) vs. Displacement (Right)

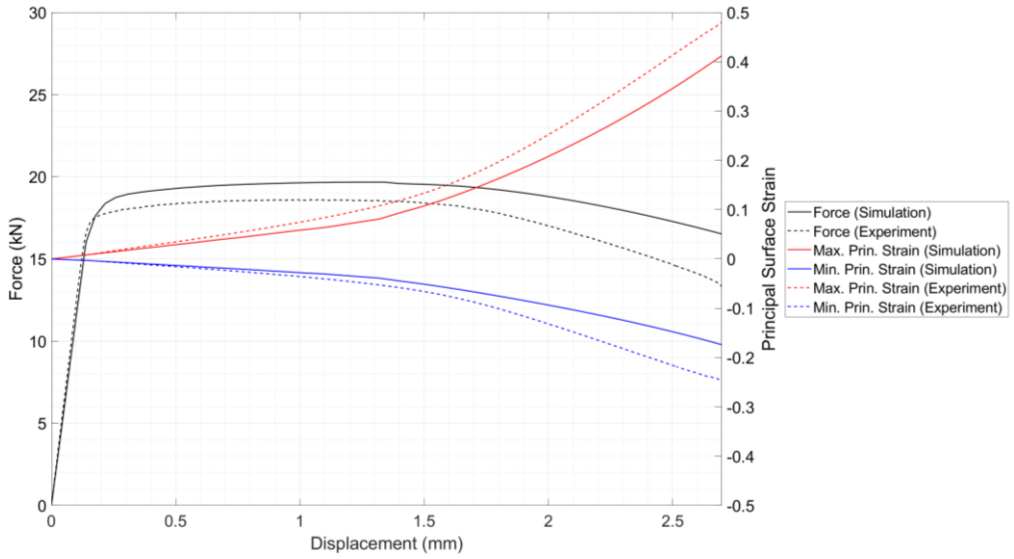

Figure 82: SG5 Test #3 (SG5_3) Force vs. Displacement (Left) and Principal Surface Strains (E1 – max, E2 – min) vs. Displacement (Right)

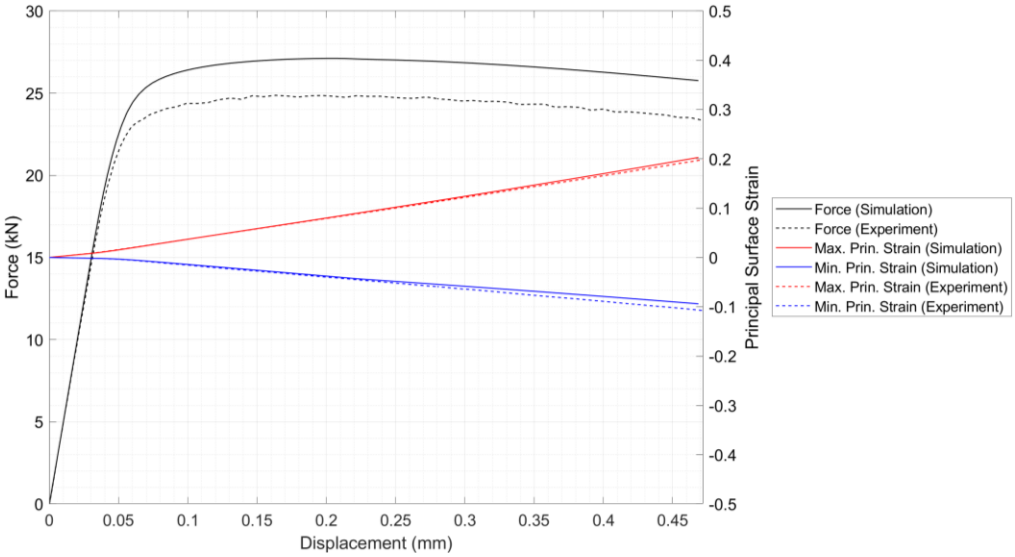

Figure 83: SG5 Test #5 (SG5_5) Force vs. Displacement (Left) and Principal Surface Strains (E1 – max, E2 – min) vs. Displacement (Right)

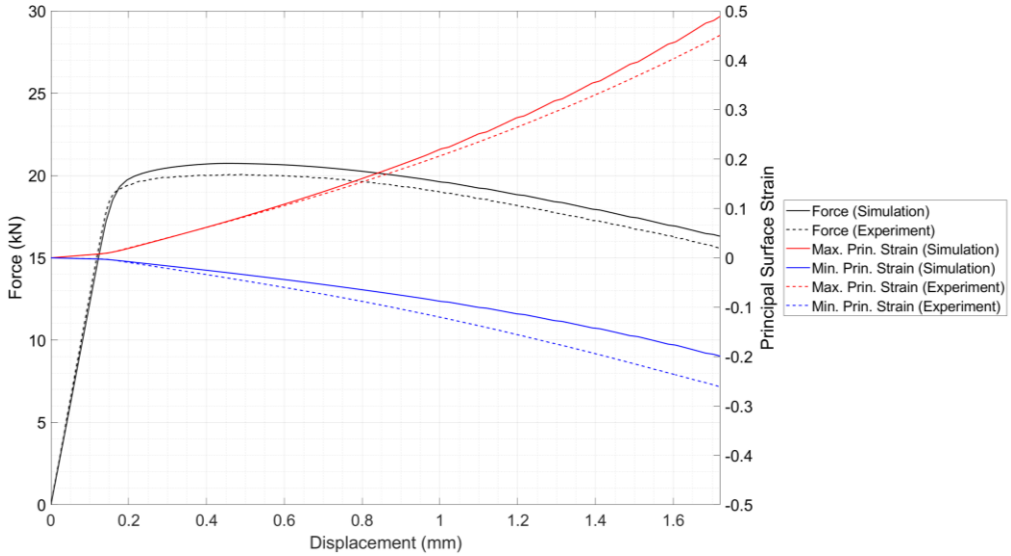

Figure 84: SG6 Test #2(SG6_2) Force vs. Displacement (Left) and Principal Surface Strains (E1 – max, E2 – min) vs. Displacement (Right)

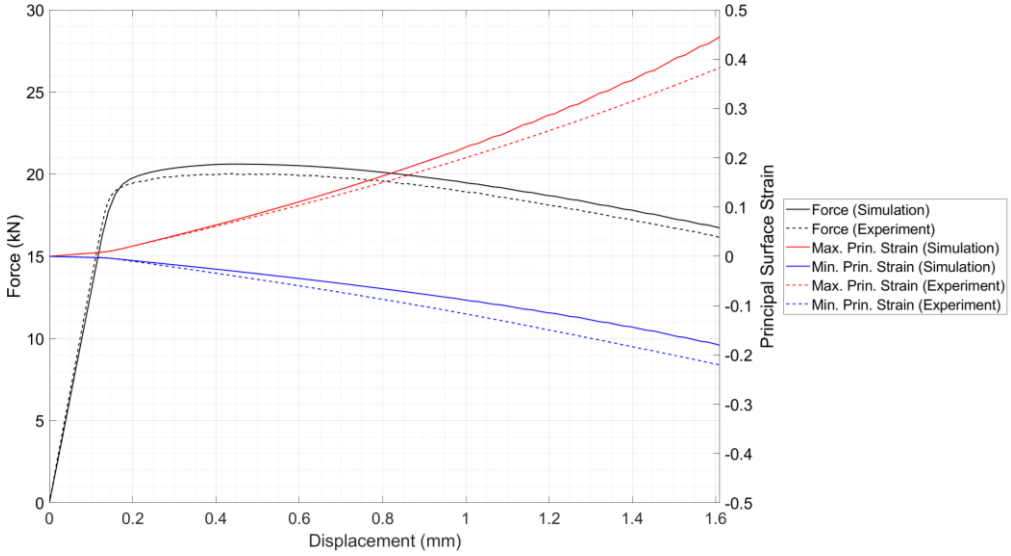

Figure 85: SG6 Test #3(SG6_3) Force vs. Displacement (Left) and Principal Surface Strains (E1 – max, E2 – min) vs. Displacement (Right)

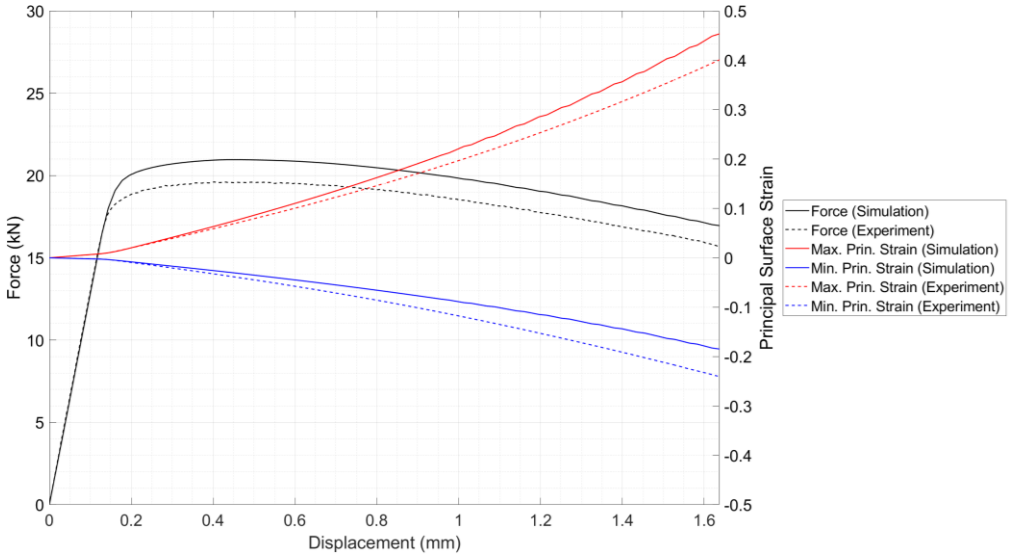

Figure 86: SG6 Test #4(SG6_4) Force vs. Displacement (Left) and Principal Surface Strains (E1 – max, E2 – min) vs. Displacement (Right)

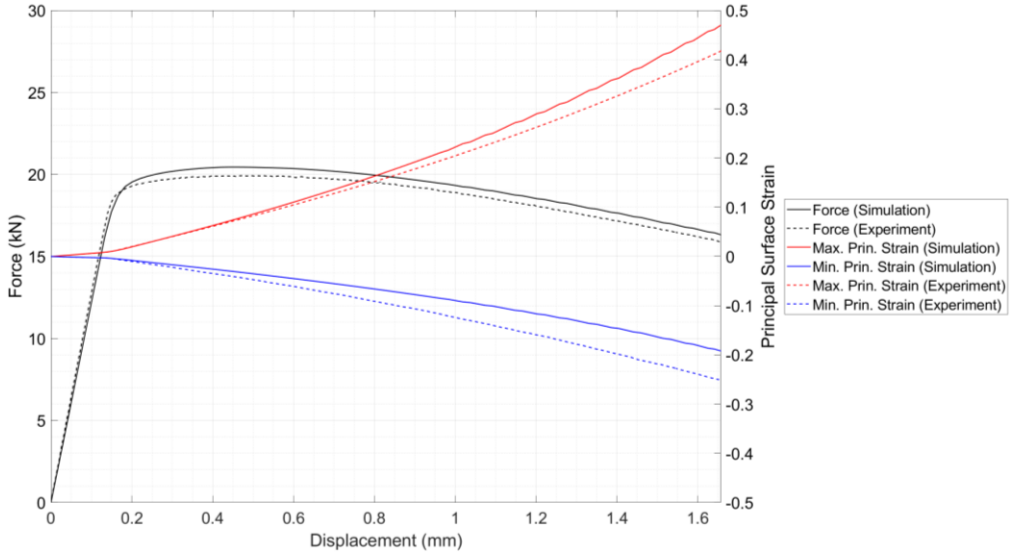

Figure 87: SG6 Test #5(SG6_5) Force vs. Displacement (Left) and Principal Surface Strains (E1 – max, E2 – min) vs. Displacement (Right)

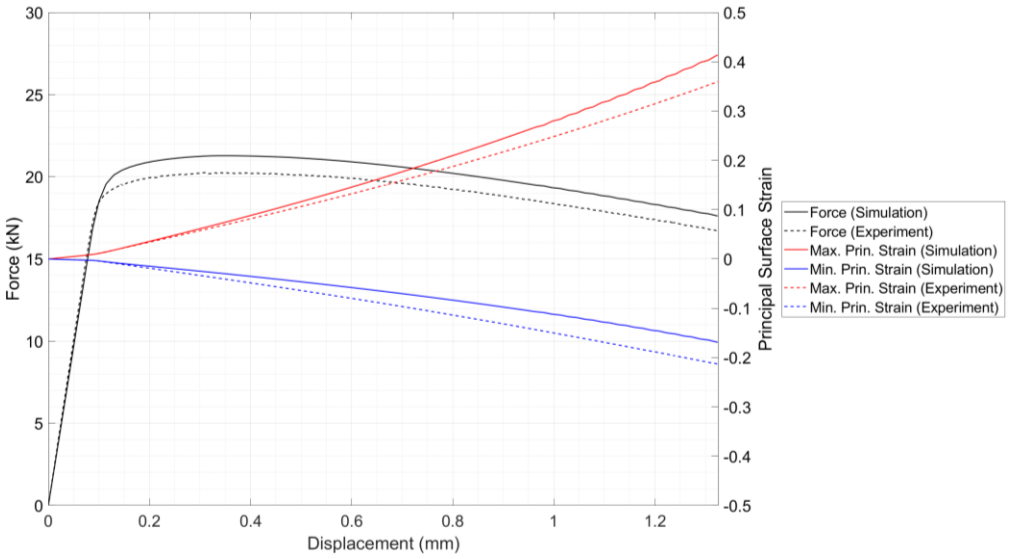

Figure 88: SG7 Test #2(SG7_2) Force vs. Displacement (Left) and Principal Surface Strains (E1 – max, E2 – min) vs. Displacement (Right)

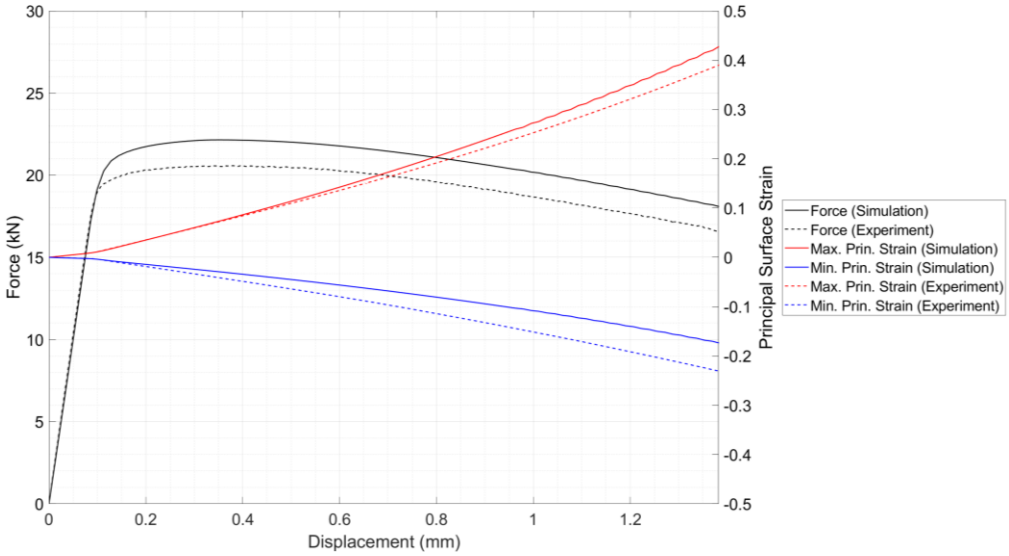

Figure 89: SG7 Test #3(SG7_3) Force vs. Displacement (Left) and Principal Surface Strains (E1 – max, E2 – min) vs. Displacement (Right)

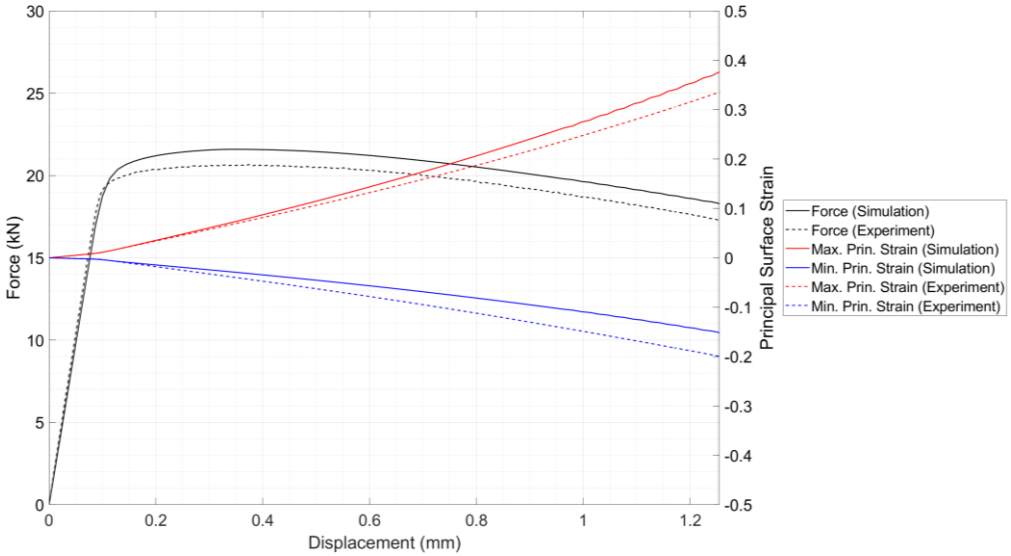

Figure 90: SG7 Test #4(SG7_4) Force vs. Displacement (Left) and Principal Surface Strains (E1 – max, E2 – min) vs. Displacement (Right)

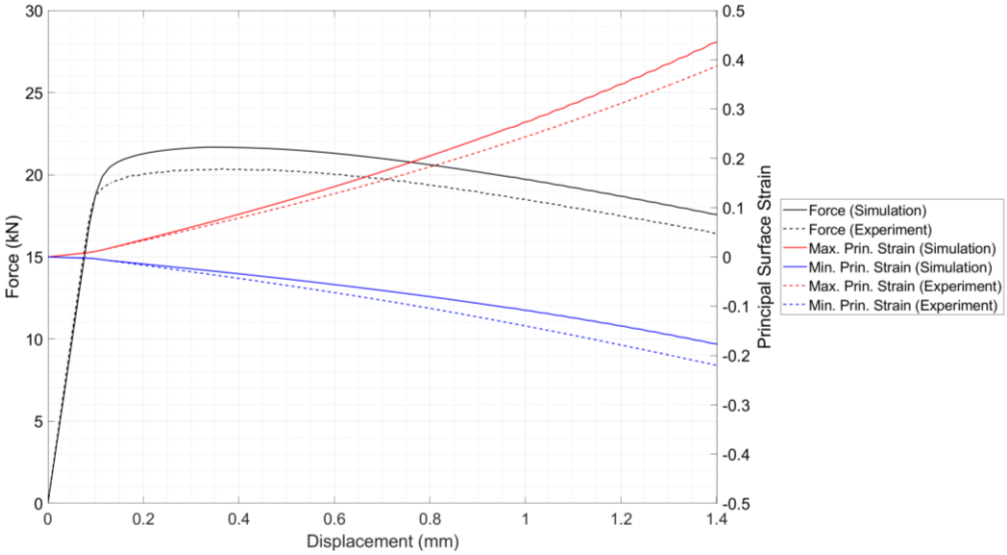

Figure 91: SG7 Test #5(SG7_5) Force vs. Displacement (Left) and Principal Surface Strains (E1 – max, E2 – min) vs. Displacement (Right)

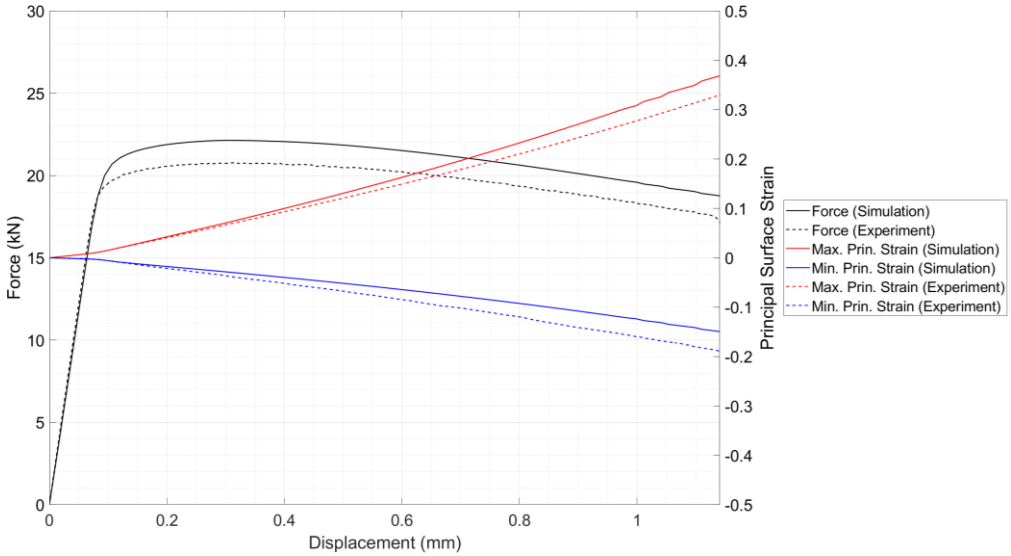

Figure 92: SG8 Test #2(SG8_2) Force vs. Displacement (Left) and Principal Surface Strains (E1 – max, E2 – min) vs. Displacement (Right)

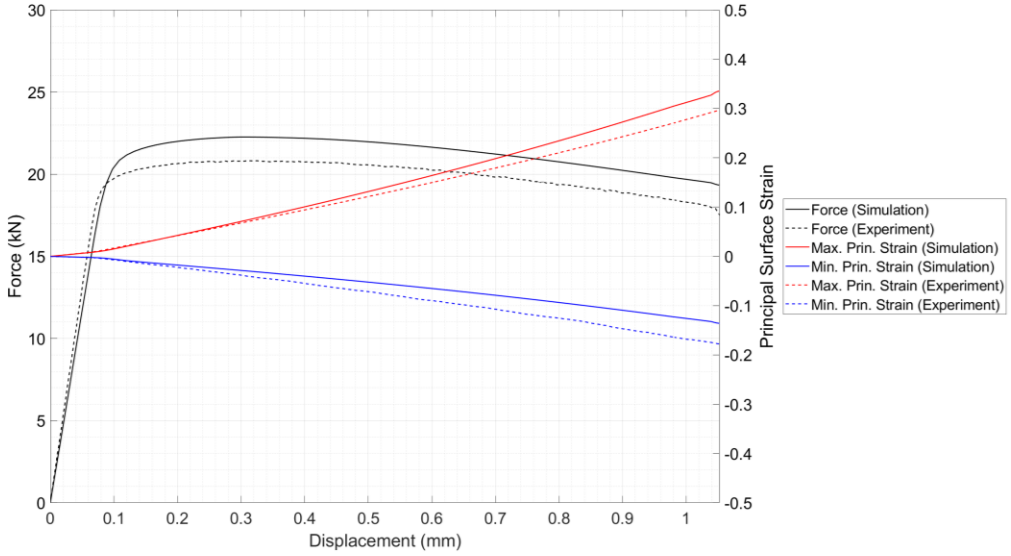

Figure 93: SG8 Test #3(SG8_3) Force vs. Displacement (Left) and Principal Surface Strains (E1 – max, E2 – min) vs. Displacement (Right)

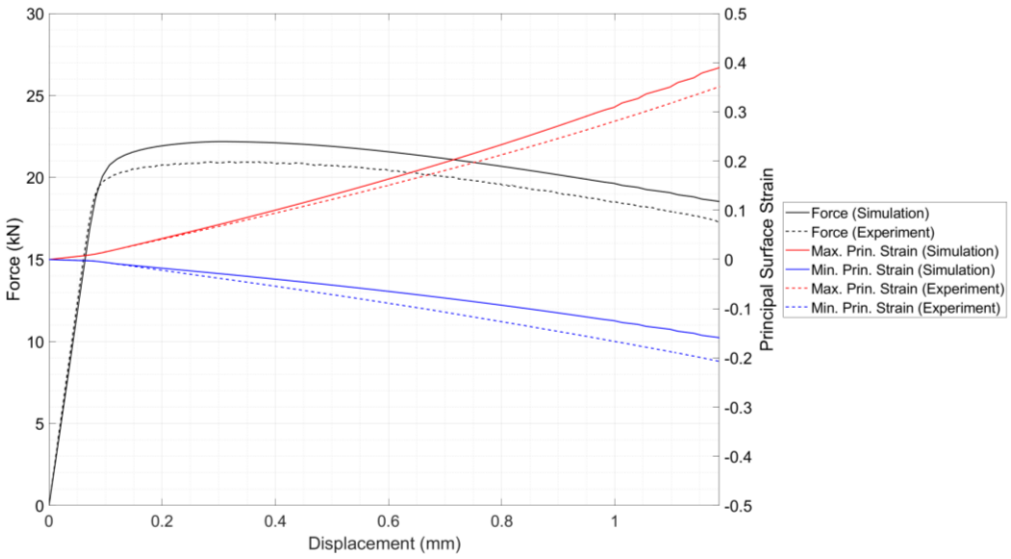

Figure 94: SG8 Test #4(SG8_4) Force vs. Displacement (Left) and Principal Surface Strains (E1 – max, E2 – min) vs. Displacement (Right)

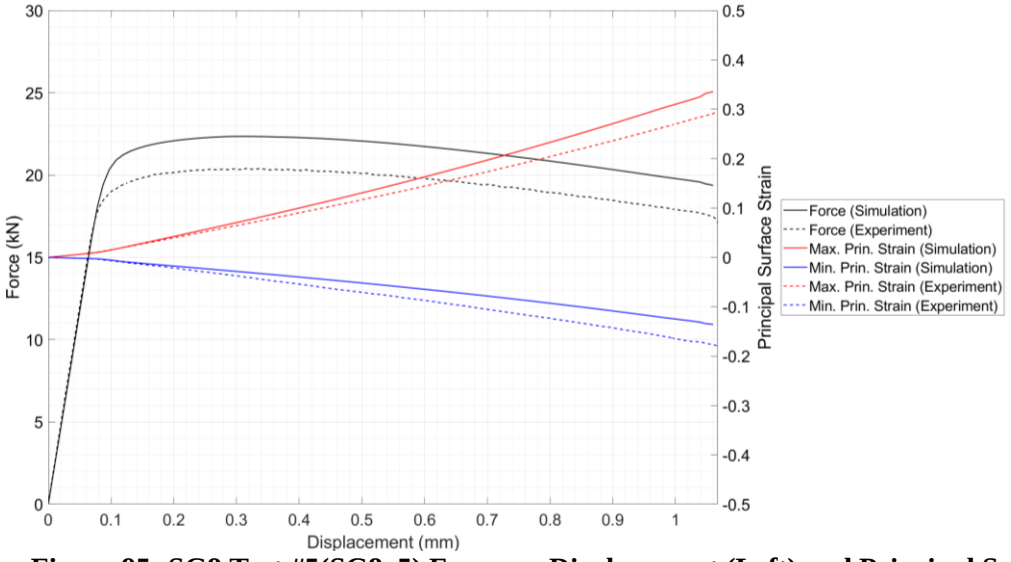

Figure 95: SG8 Test #5(SG8_5) Force vs. Displacement (Left) and Principal Surface Strains (E1 – max, E2 – min) vs. Displacement (Right)

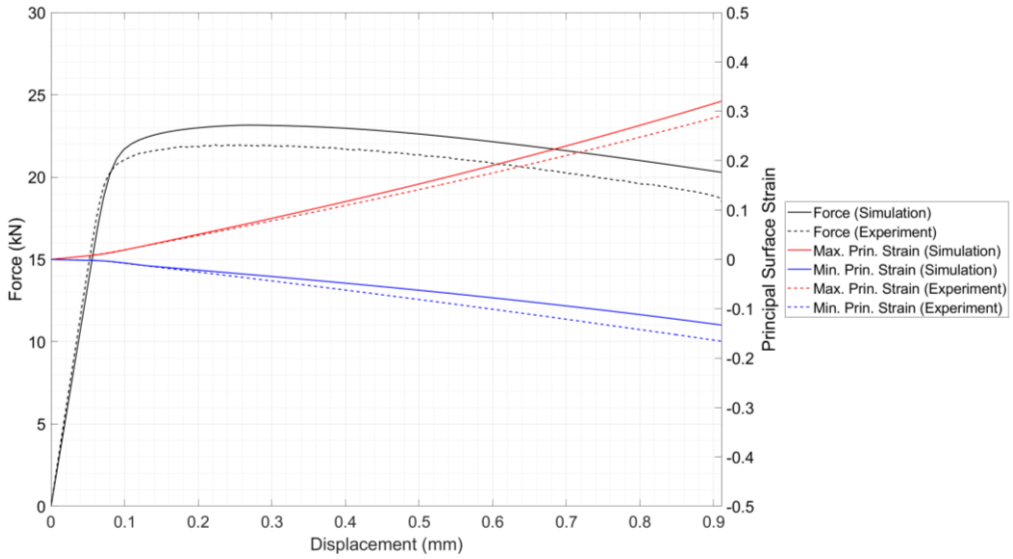

Figure 96: SG9 Test #2(SG9_2) Force vs. Displacement (Left) and Principal Surface Strains (E1 – max, E2 – min) vs. Displacement (Right)

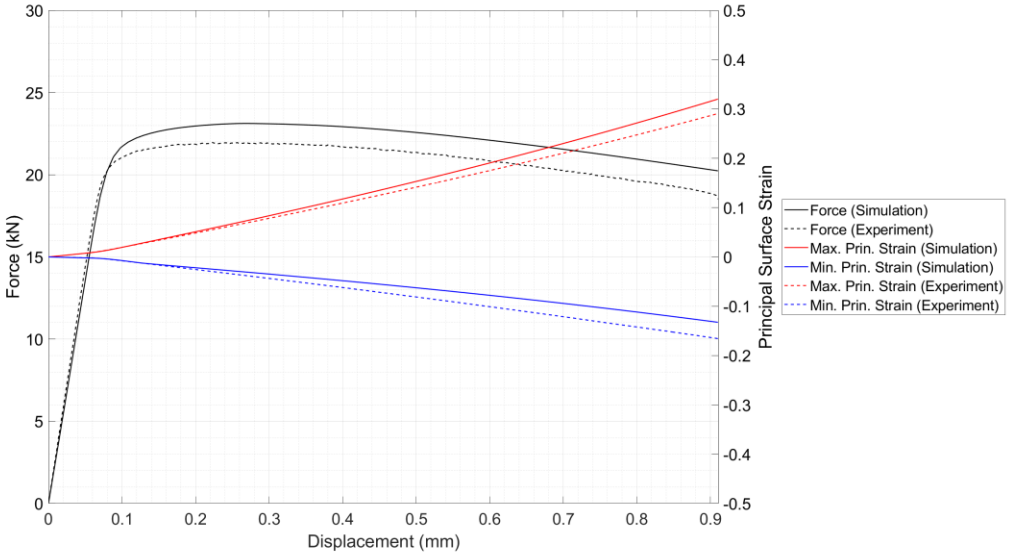

Figure 97: SG9 Test #3(SG9_3) Force vs. Displacement (Left) and Principal Surface Strains (E1 – max, E2 – min) vs. Displacement (Right)

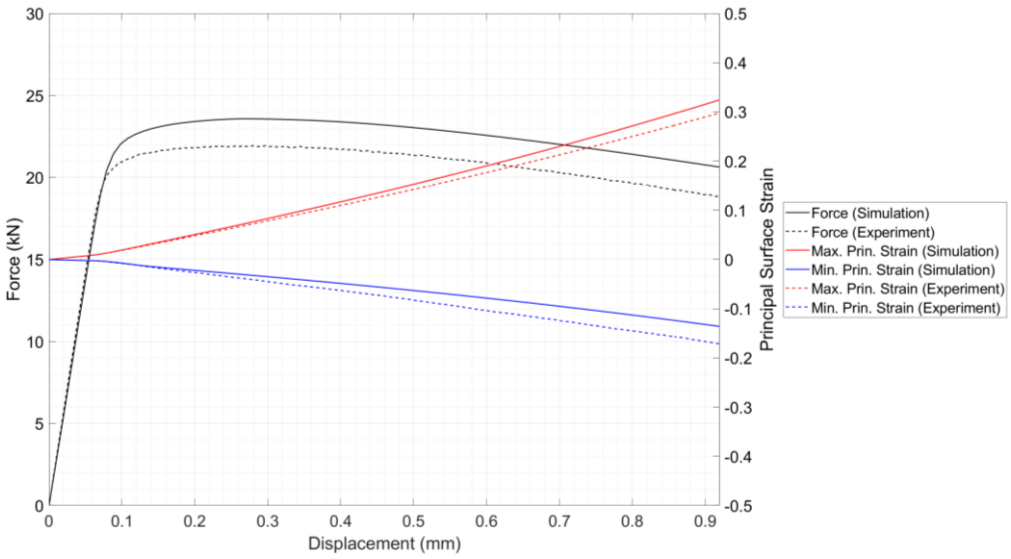

Figure 98: SG9 Test #4(SG9_4) Force vs. Displacement (Left) and Principal Surface Strains (E1 – max, E2 – min) vs. Displacement (Right)

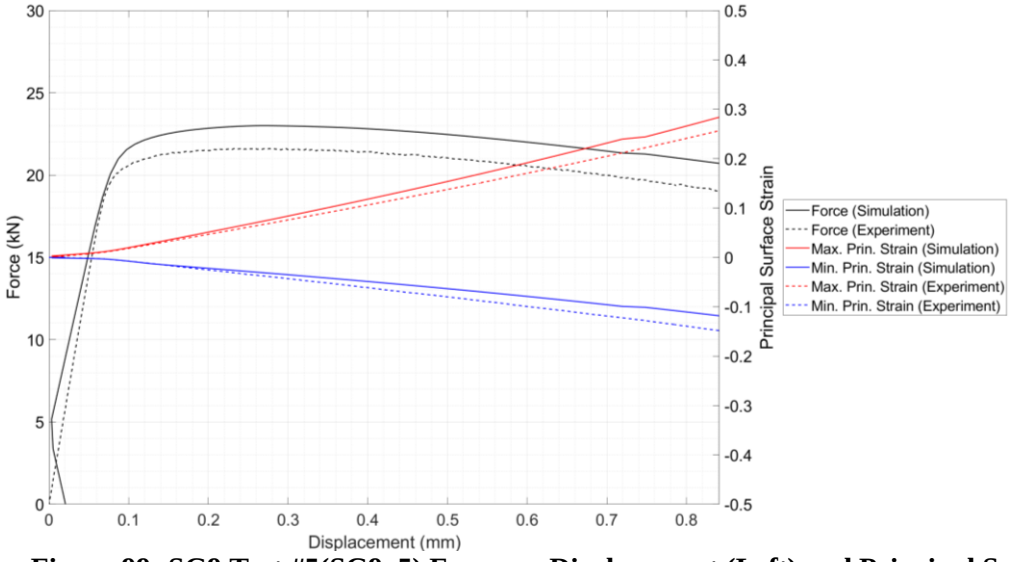

Figure 99: SG9 Test #5(SG9_5) Force vs. Displacement (Left) and Principal Surface Strains (E1 – max, E2 – min) vs. Displacement (Right)

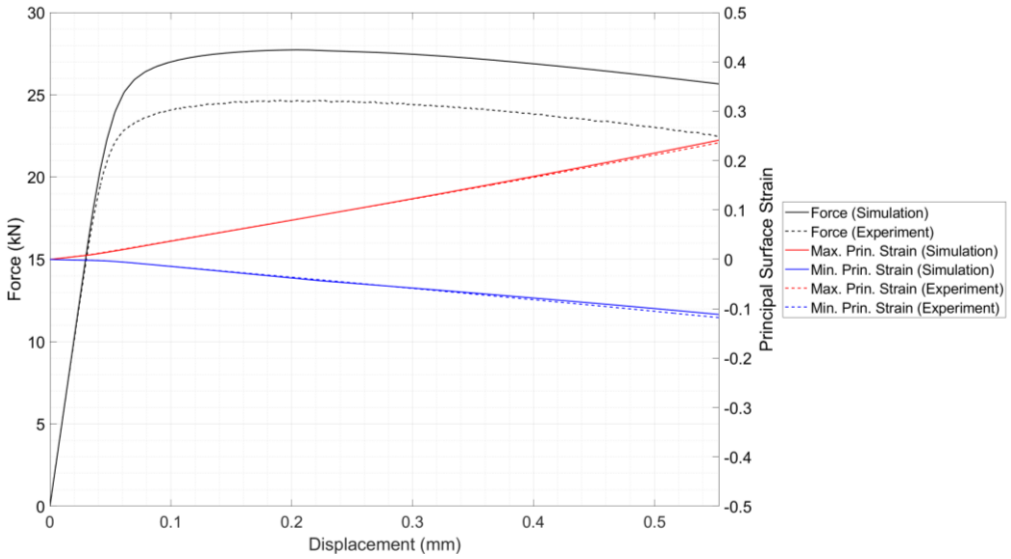

Figure 100: SG10 Test #2(SG10_2) Force vs. Displacement (Left) and Principal Surface Strains (E1 – max, E2 – min) vs. Displacement (Right)

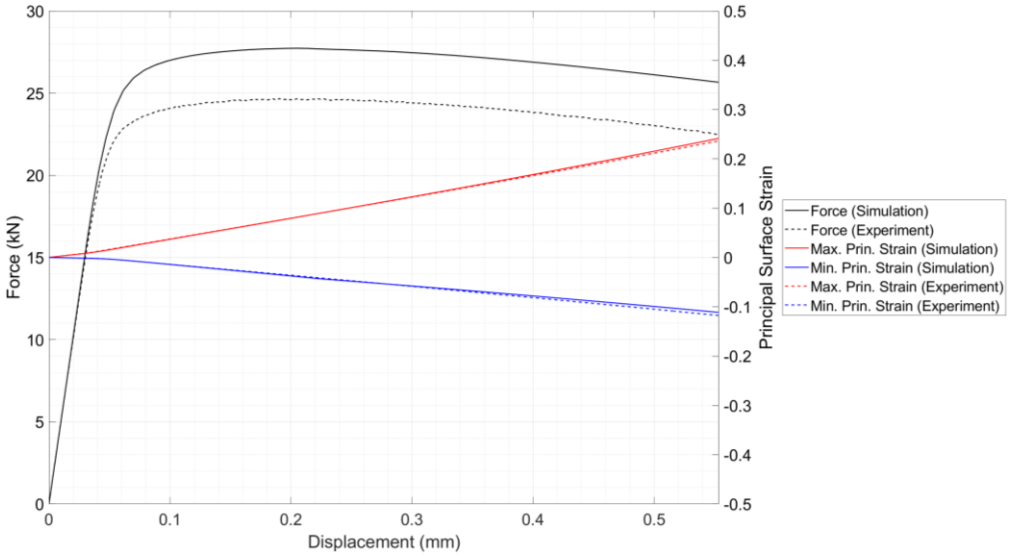

Figure 101: SG10 Test #3(SG10_3) Force vs. Displacement (Left) and Principal Surface Strains (E1 – max, E2 – min) vs. Displacement (Right)

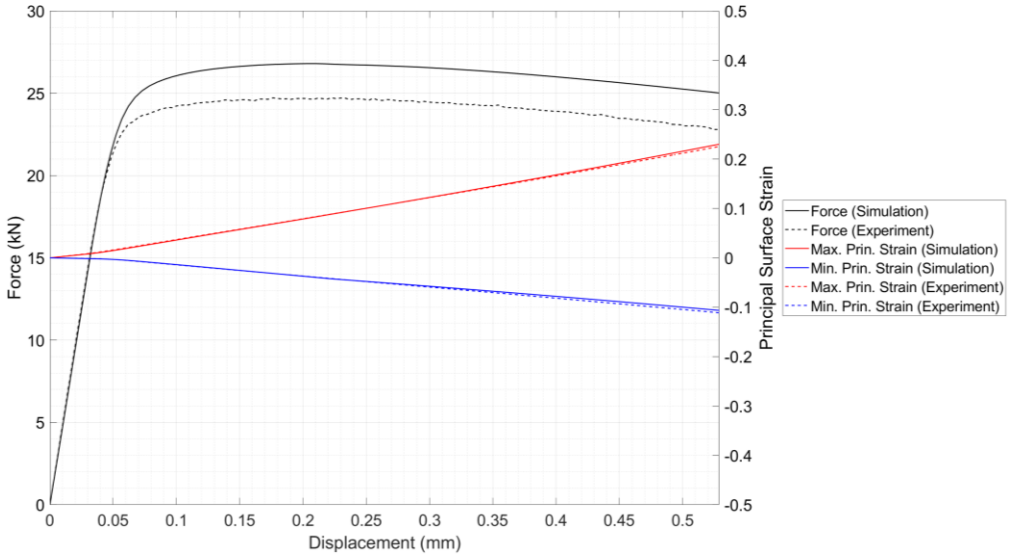

Figure 102: SG10 Test #4(SG10_4) Force vs. Displacement (Left) and Principal Surface Strains (E1 – max, E2 – min) vs. Displacement (Right)

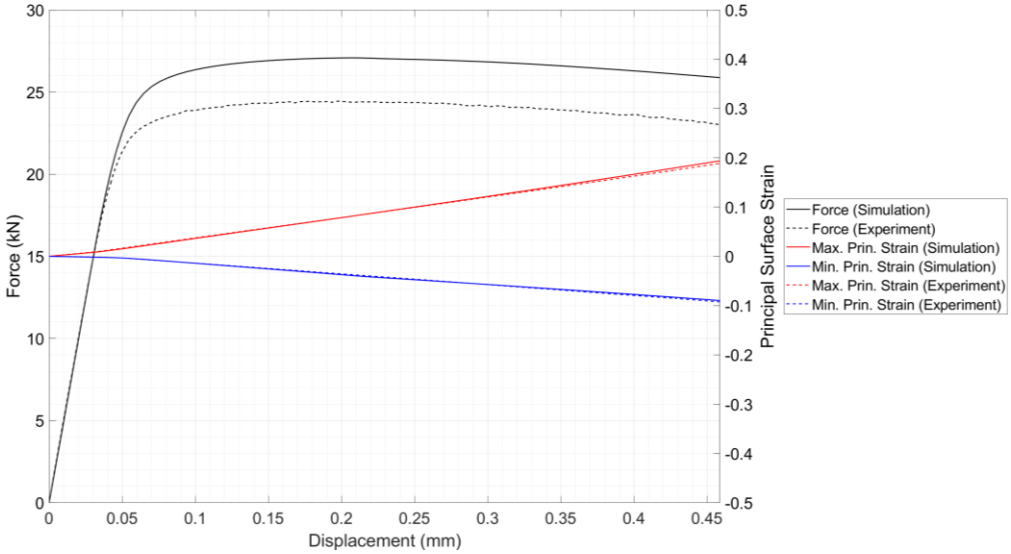

Figure 103: SG10 Test #5(SG10_5) Force vs. Displacement (Left) and Principal Surface Strains (E1 – max, E2 – min) vs. Displacement (Right)

Experimental and Simulation Principal Surface Strain Plots

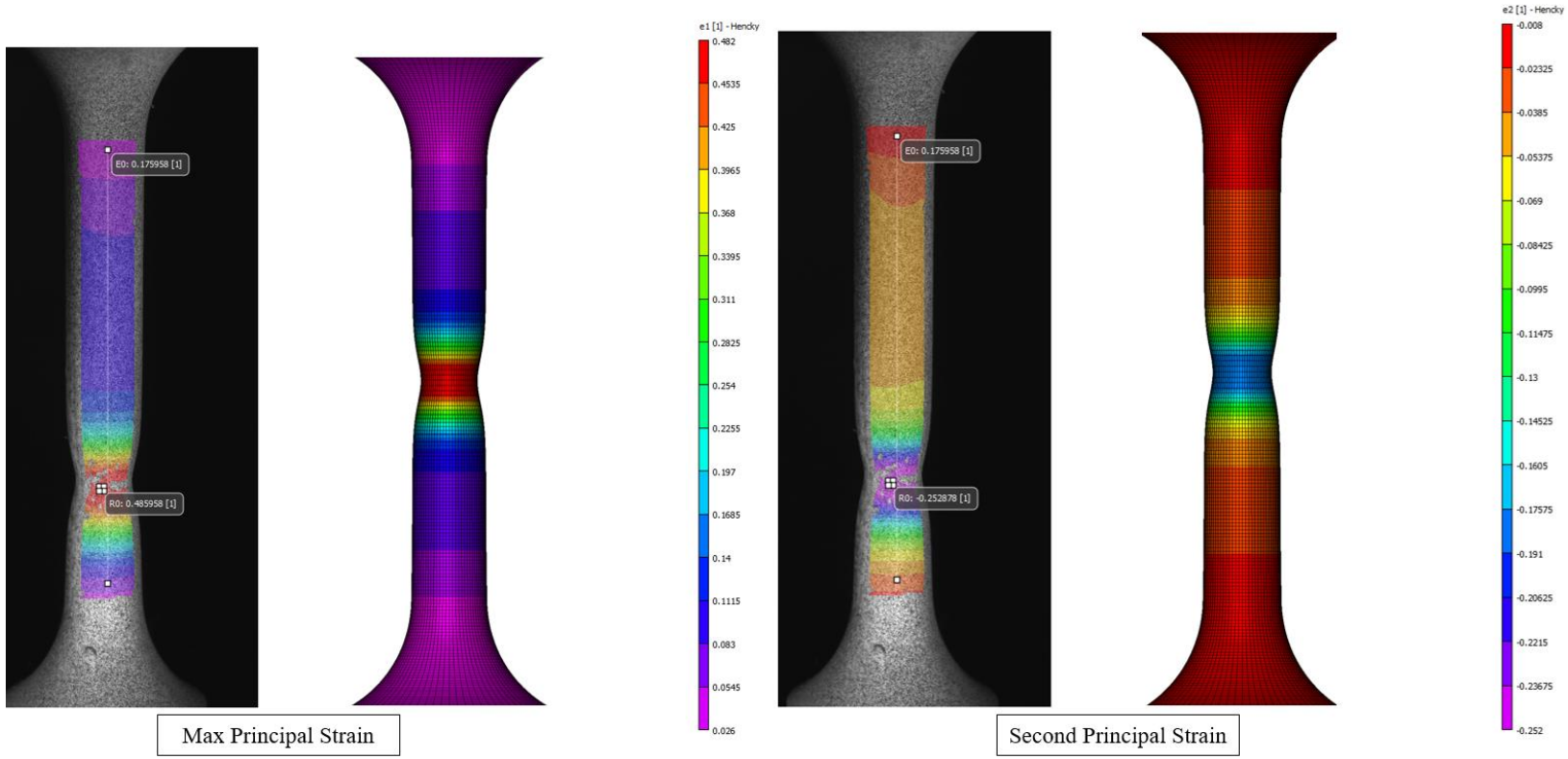

Figure 104: SG5_1 Principal Surface Strain Fringe Plots (Experimental vs. Simulation)

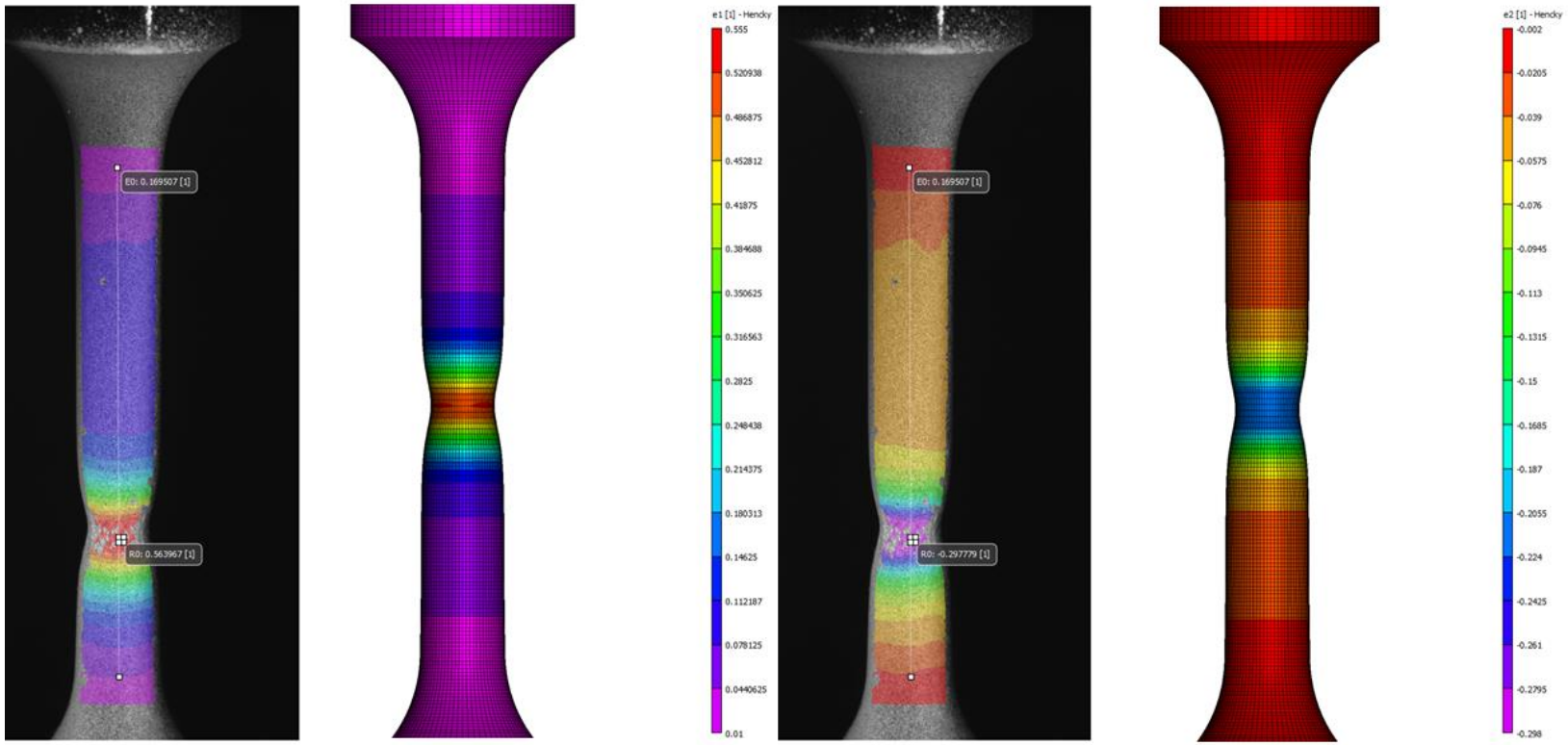

Figure 105: SG5_2 Principal Surface Strain Fringe Plots (Experimental vs. Simulation)

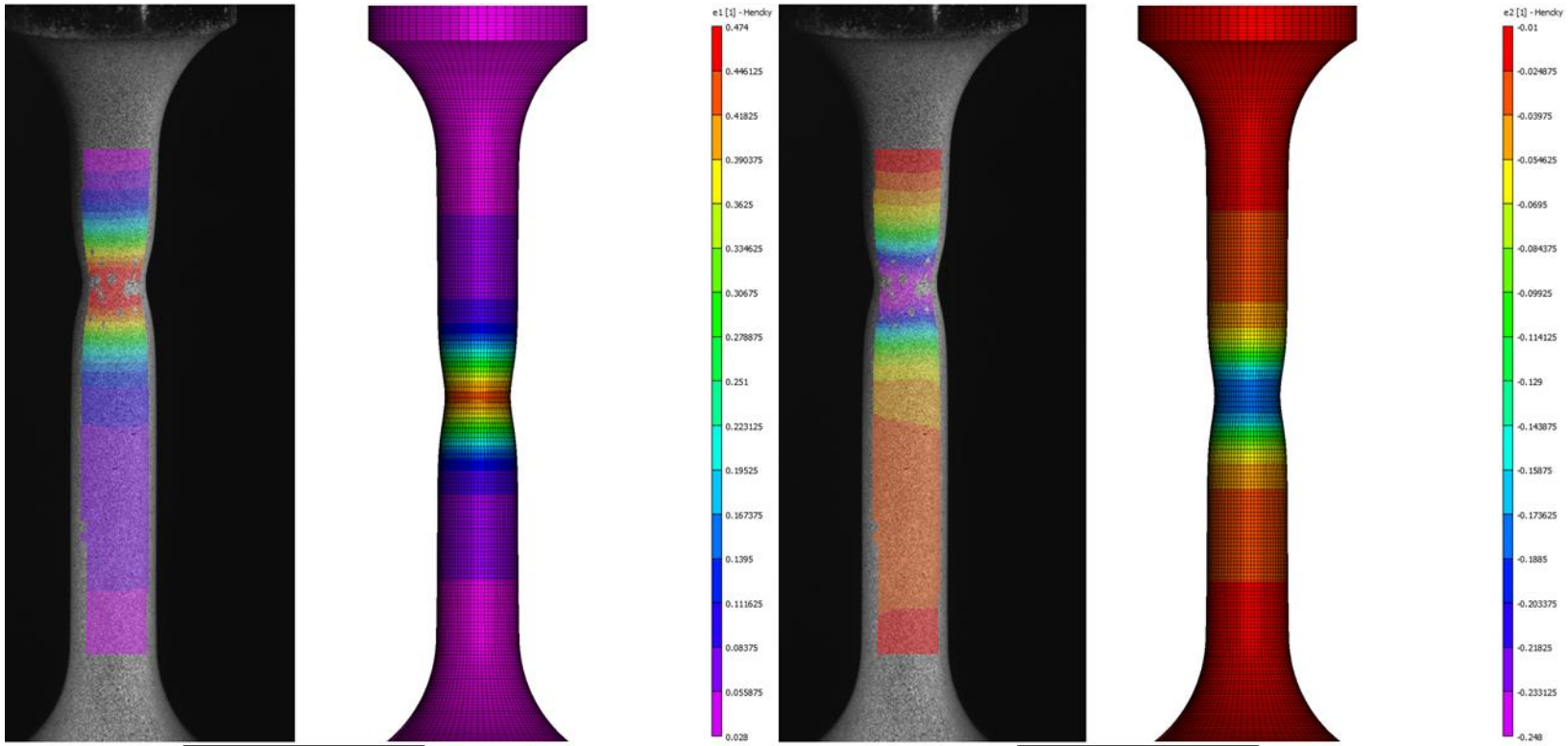

Figure 106: SG5_3 Principal Surface Strain Fringe Plots (Experimental vs. Simulation)

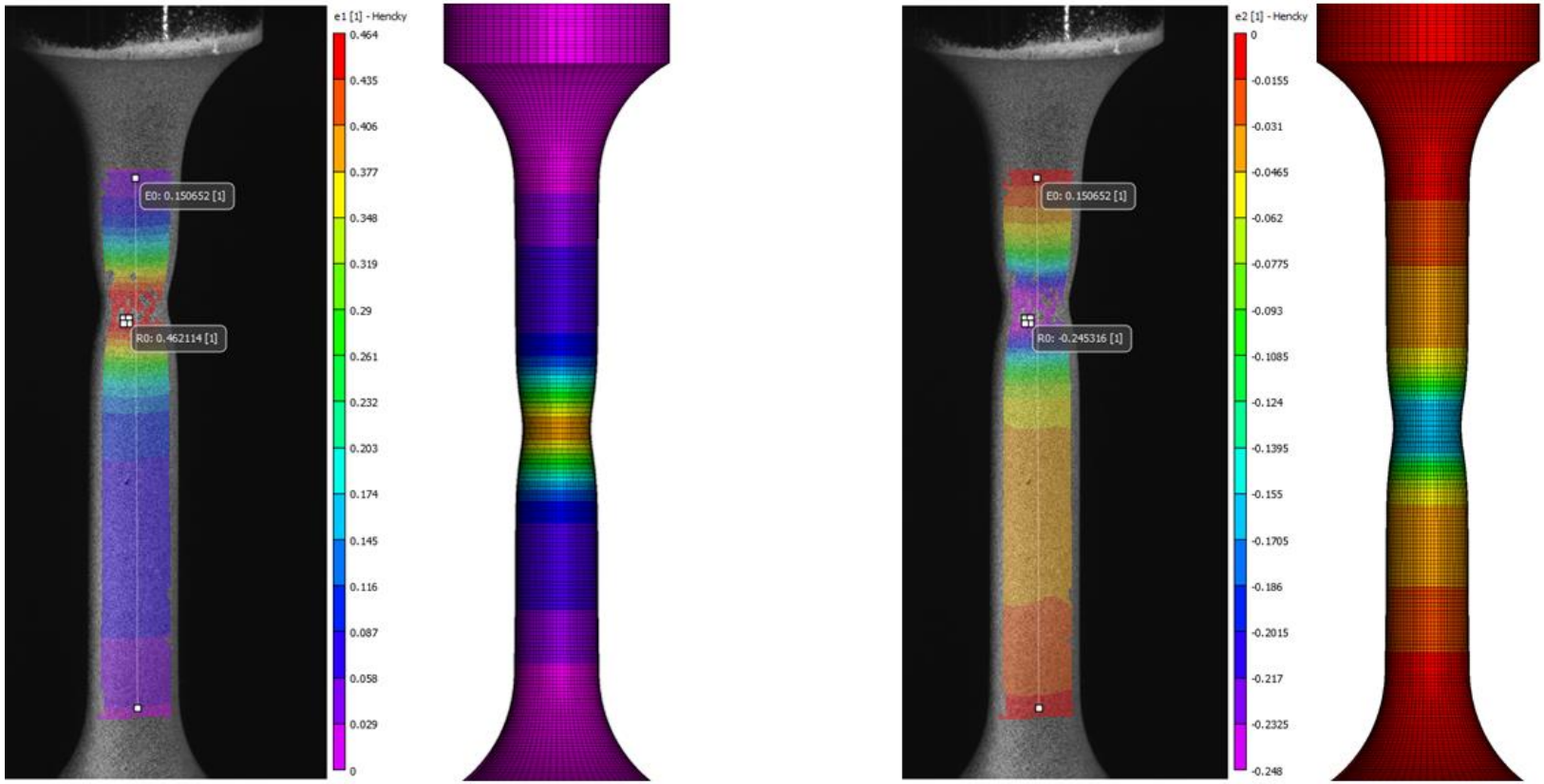

Max Principal Strain

Second Principal Strain

Figure 107: SG5_5 Principal Surface Strain Fringe Plots (Experimental vs. Simulation)

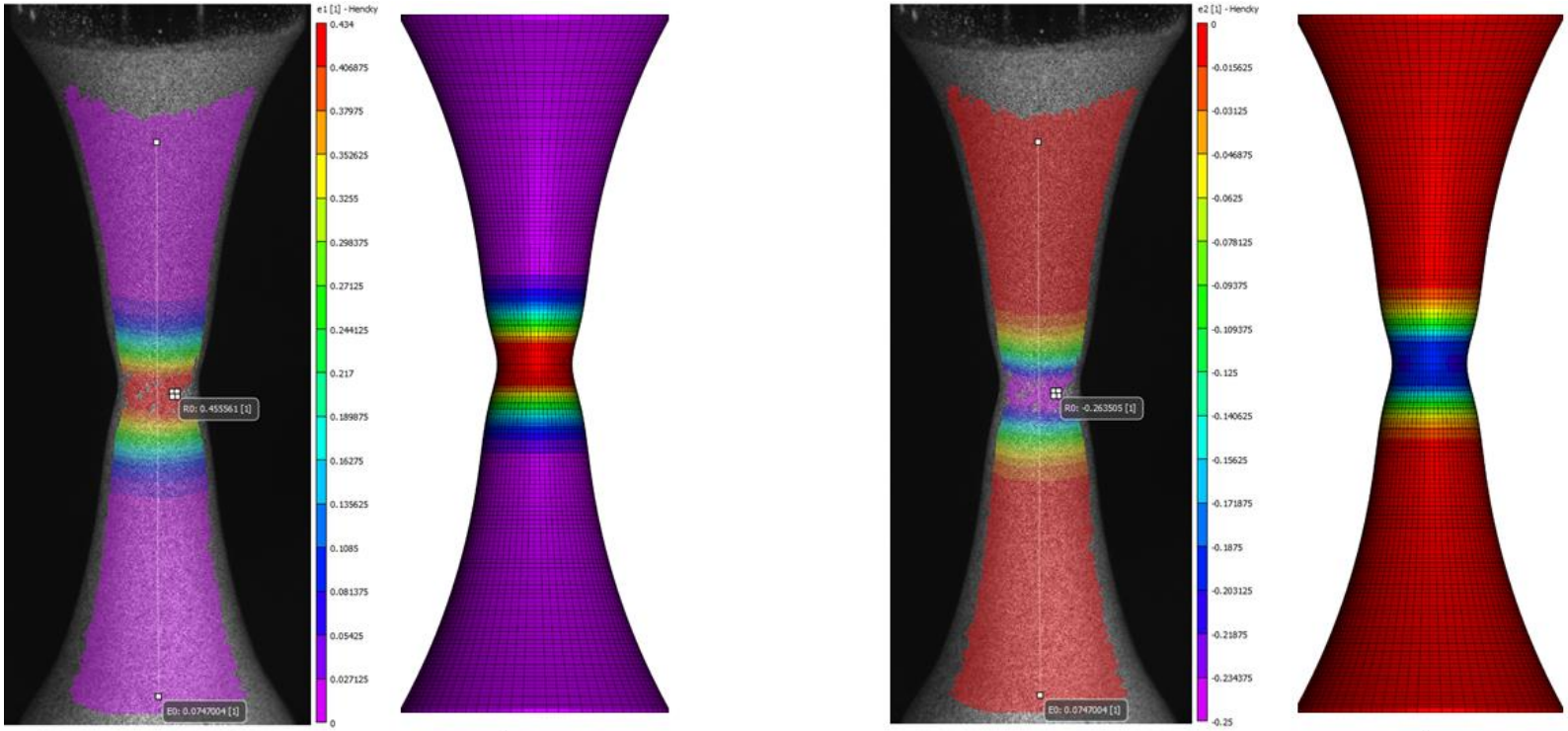

Figure 108: SG6_2 Principal Surface Strain Fringe Plots (Experimental vs. Simulation)

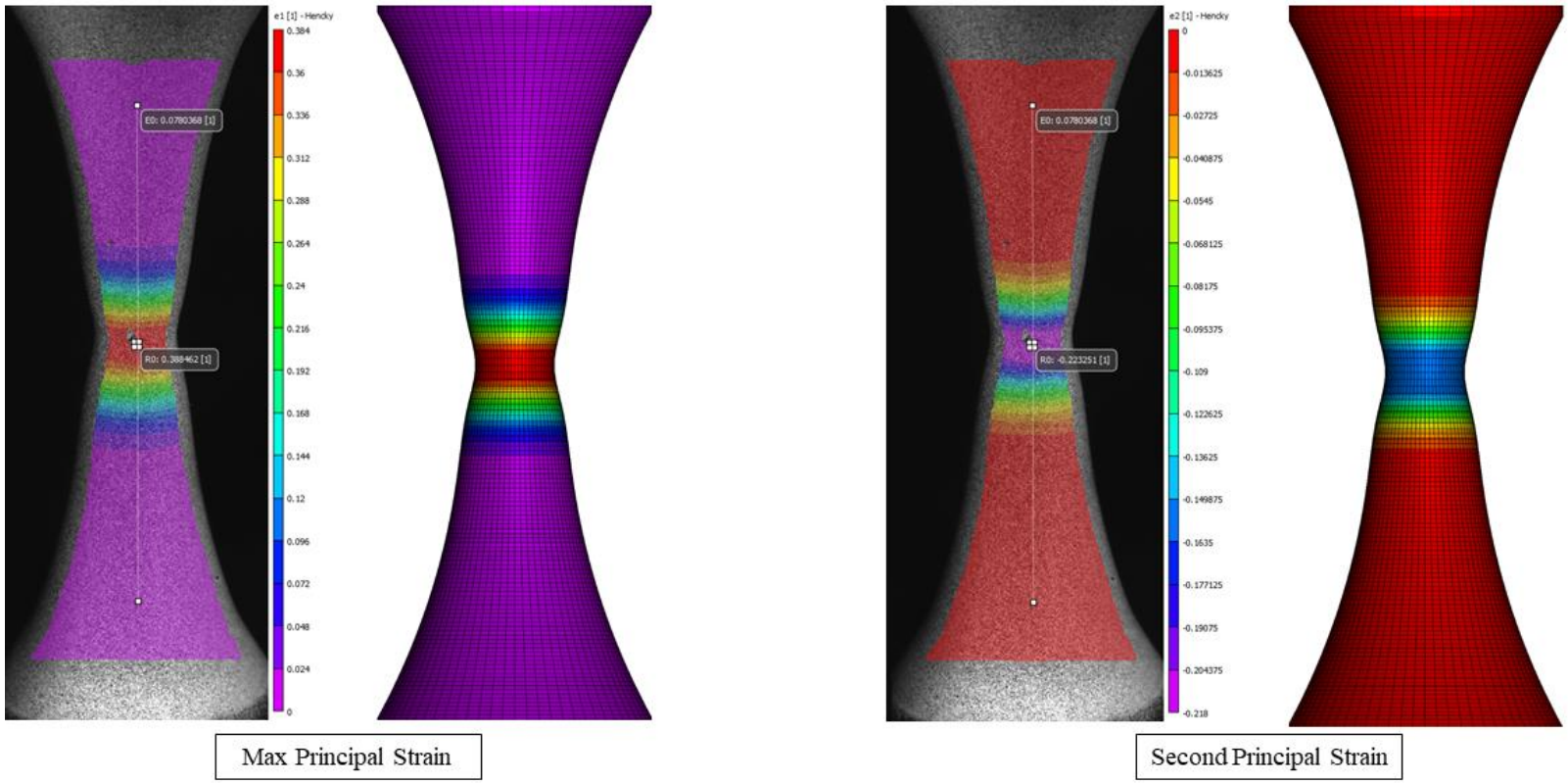

Figure 109: SG6_3 Principal Surface Strain Fringe Plots (Experimental vs. Simulation)

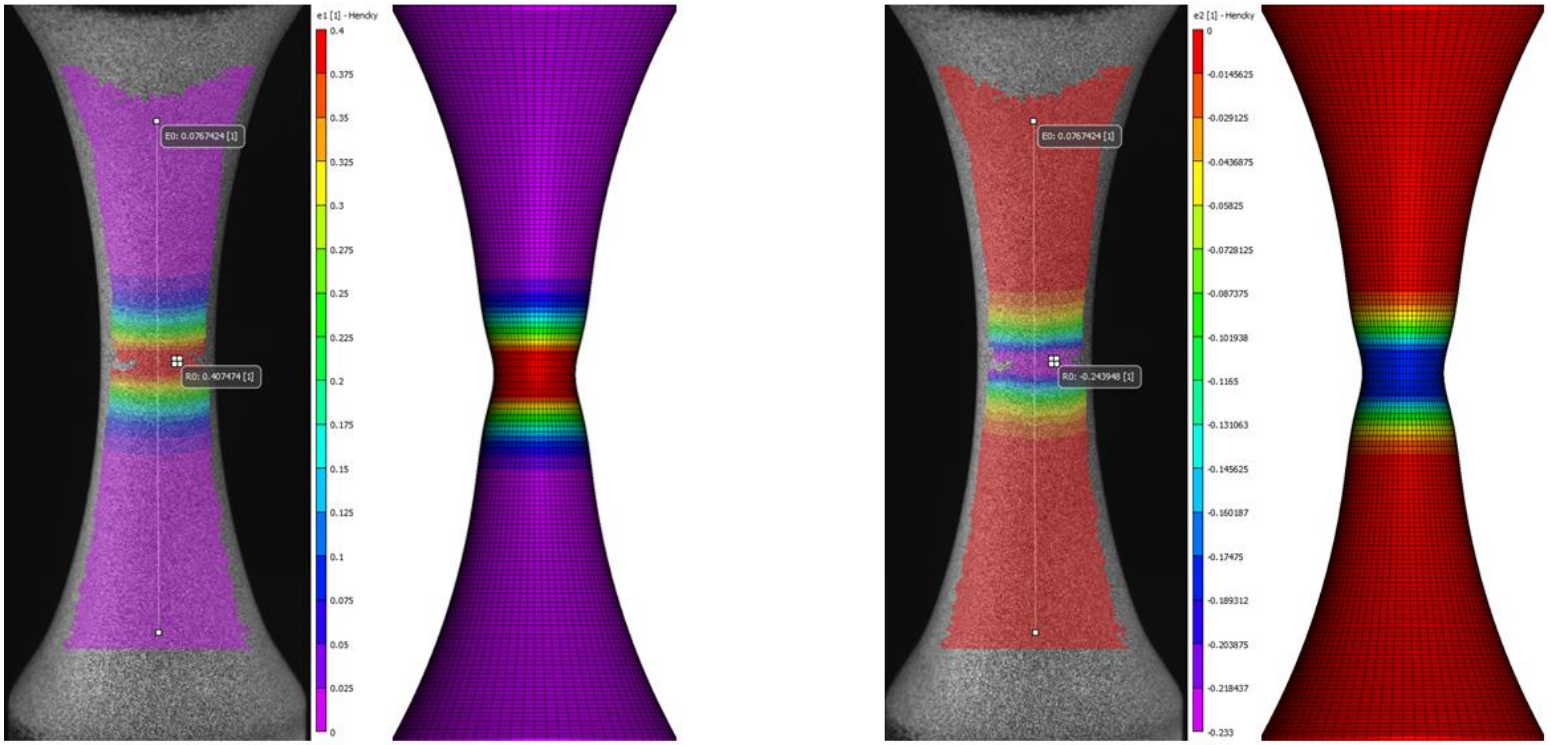

Figure 110: SG6_4 Principal Surface Strain Fringe Plots (Experimental vs. Simulation)

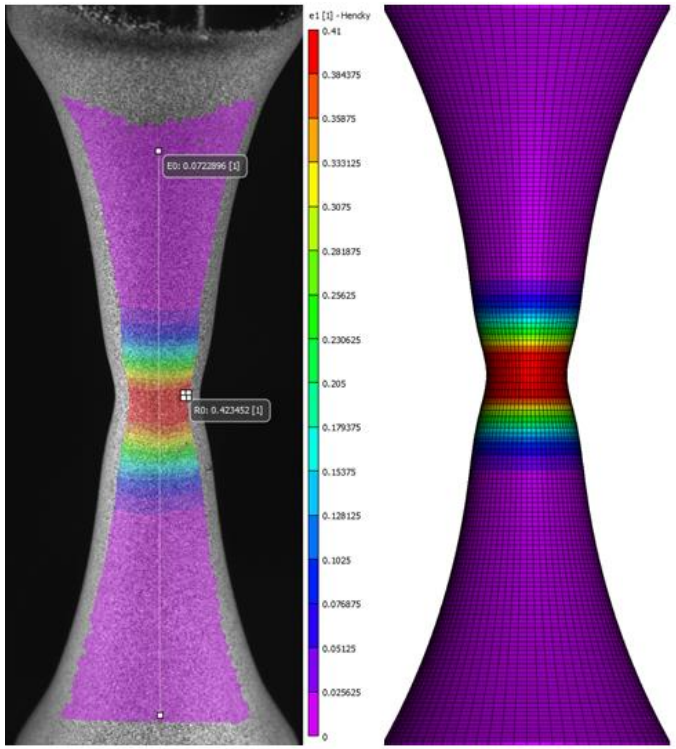

Max Principal Strain

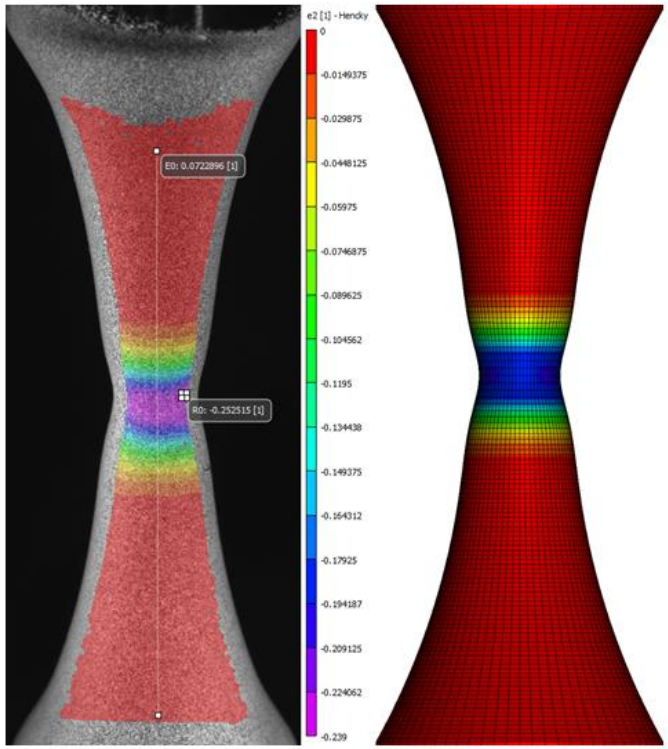

Second Principal Strain

Figure 111: SG6_5 Principal Surface Strain Fringe Plots (Experimental vs. Simulation)

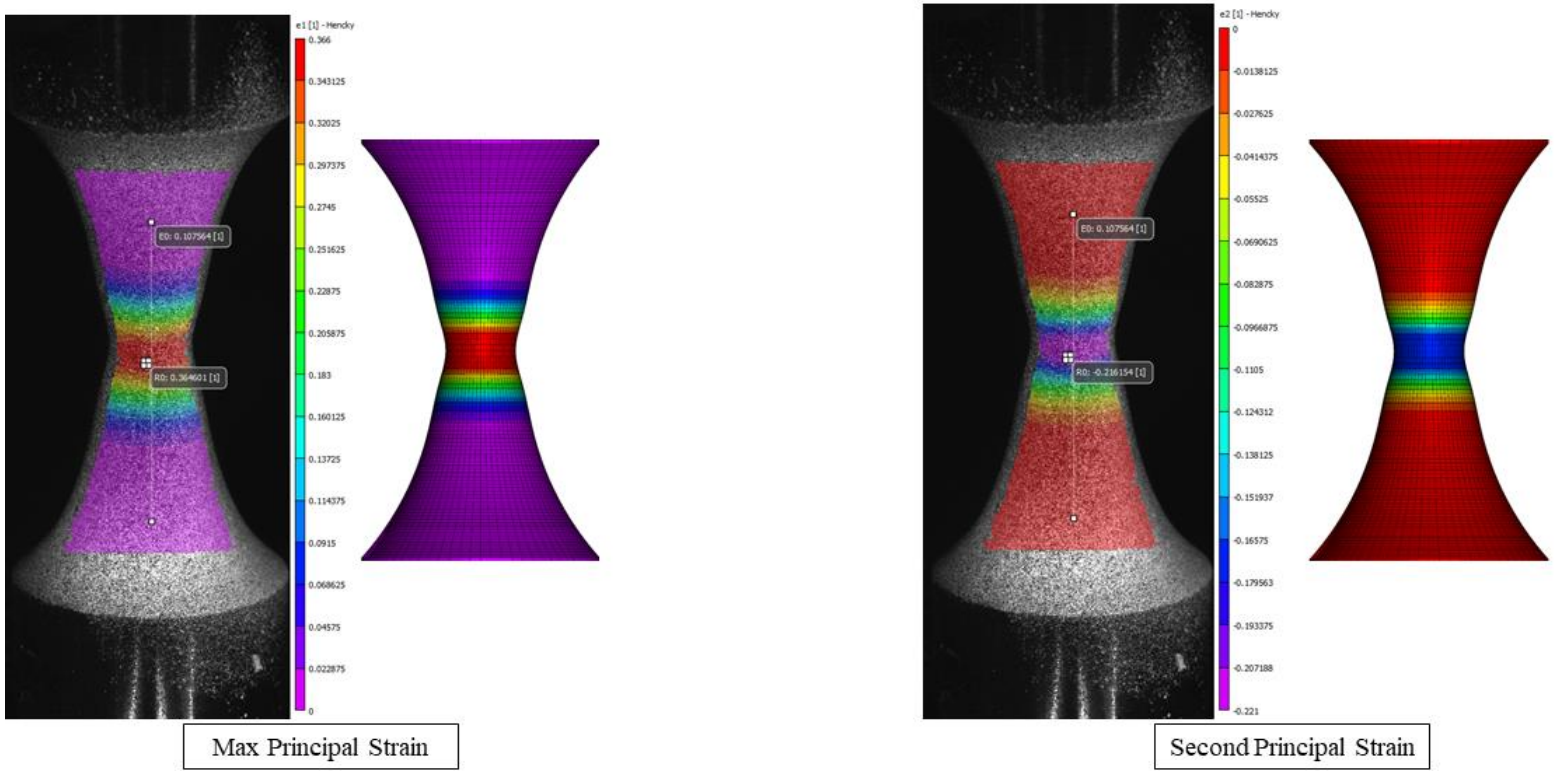

Max Principal Strain

Second Principal Strain

Figure 112: SG7_2 Principal Surface Strain Fringe Plots (Experimental vs. Simulation)

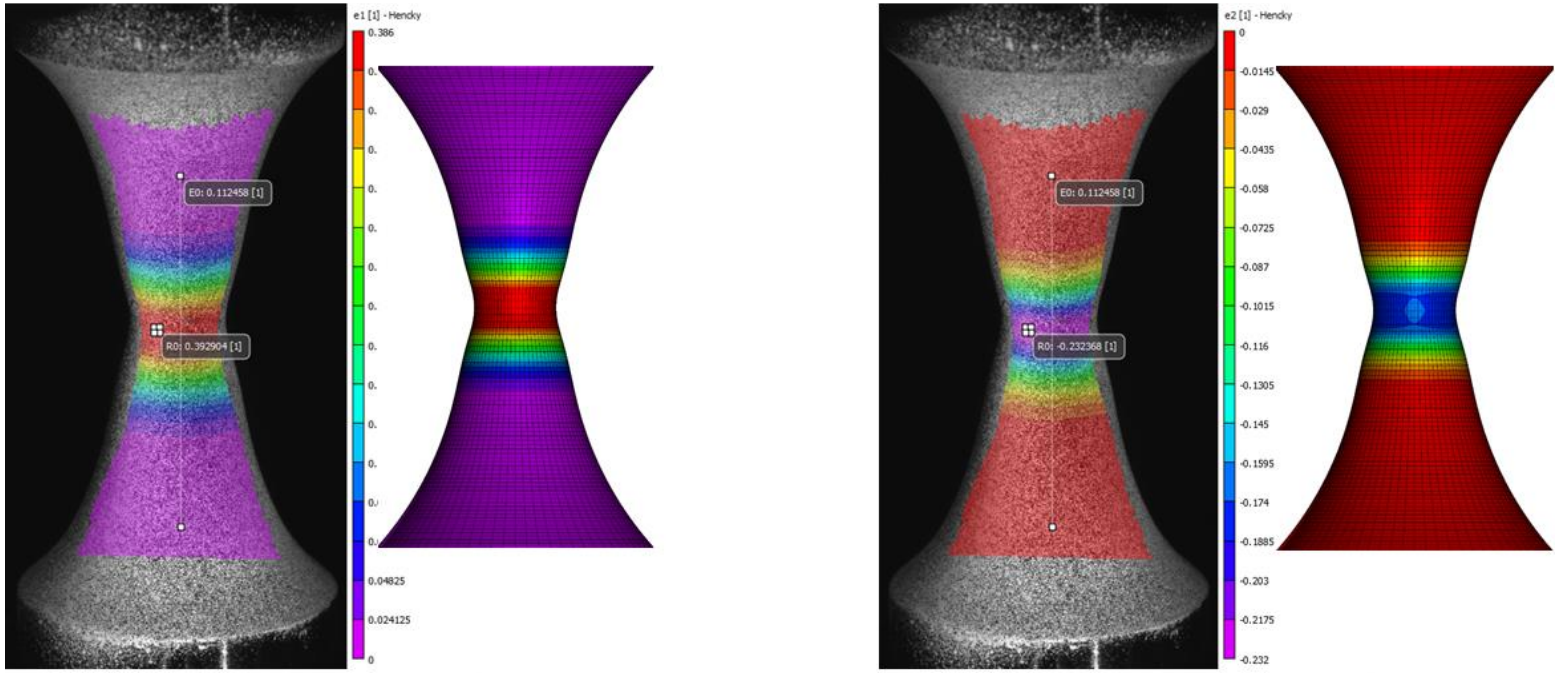

Figure 113: SG7_3 Principal Surface Strain Fringe Plots (Experimental vs. Simulation)

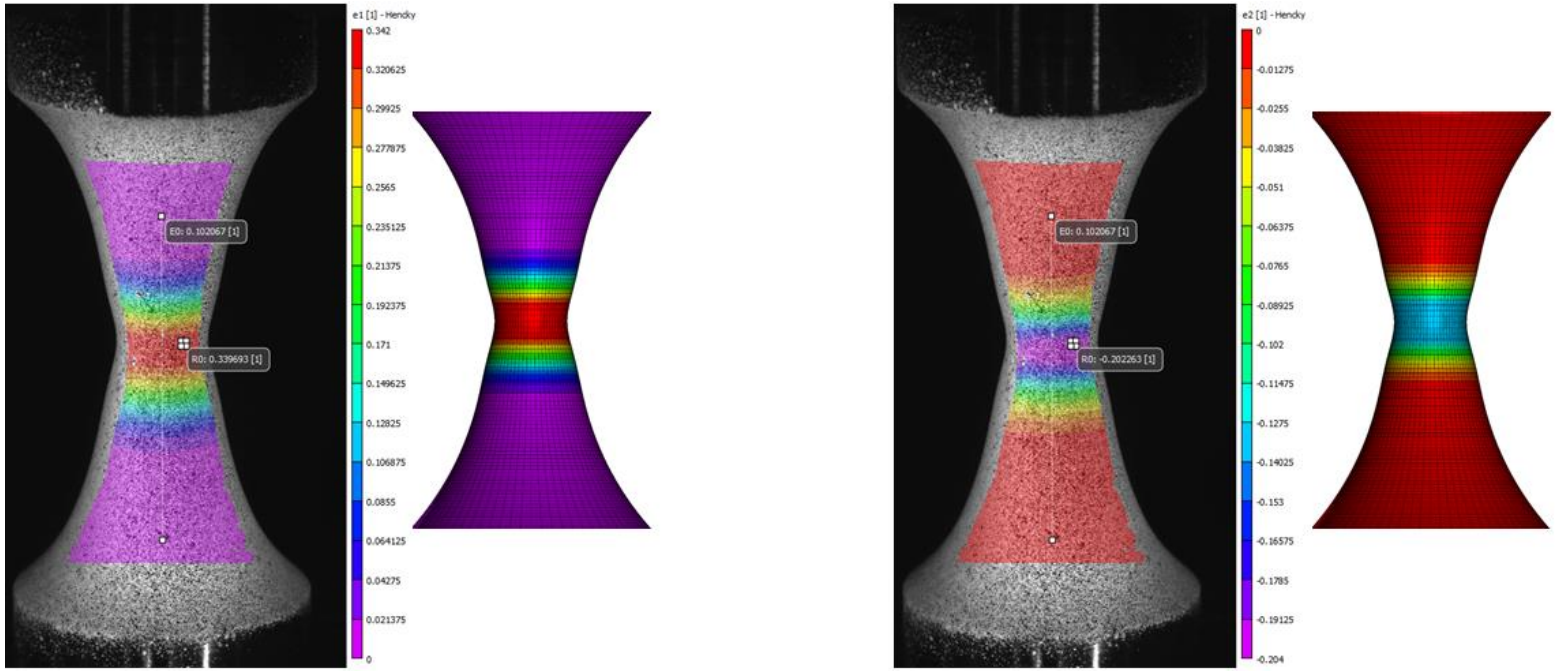

Figure 114: SG7_4 Principal Surface Strain Fringe Plots (Experimental vs. Simulation)

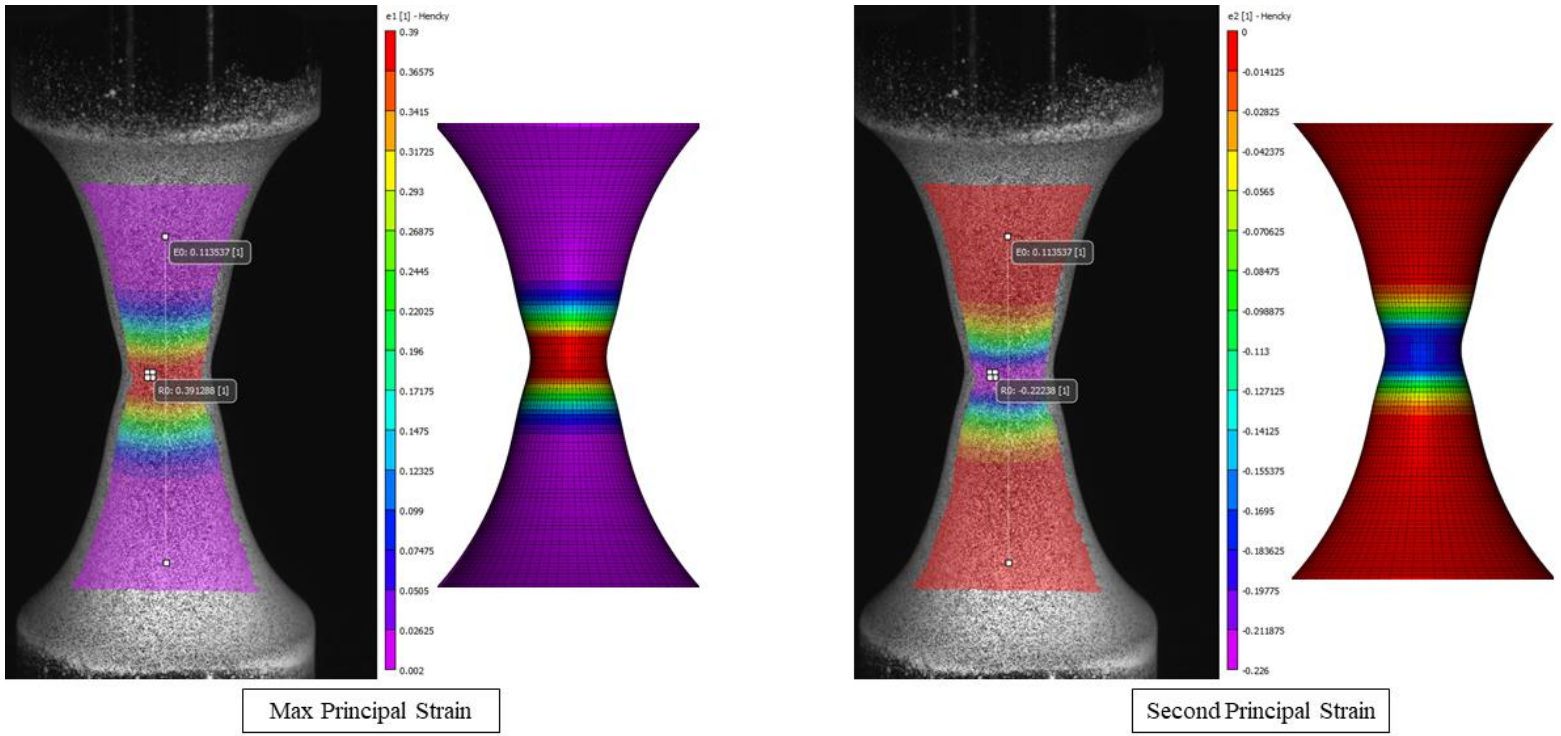

Max Principal Strain

Second Principal Strain

Figure 115: SG7_5 Principal Surface Strain Fringe Plots (Experimental vs. Simulation)

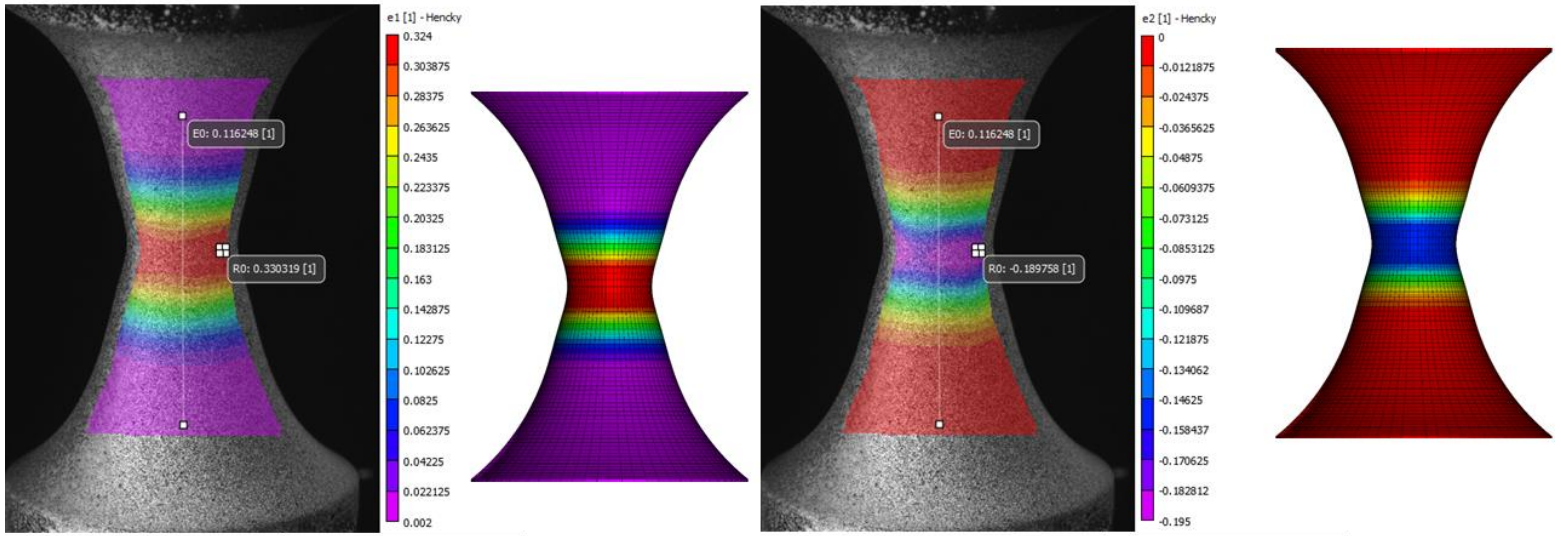

Figure 116: SG8_2 Principal Surface Strain Fringe Plots (Experimental vs. Simulation)

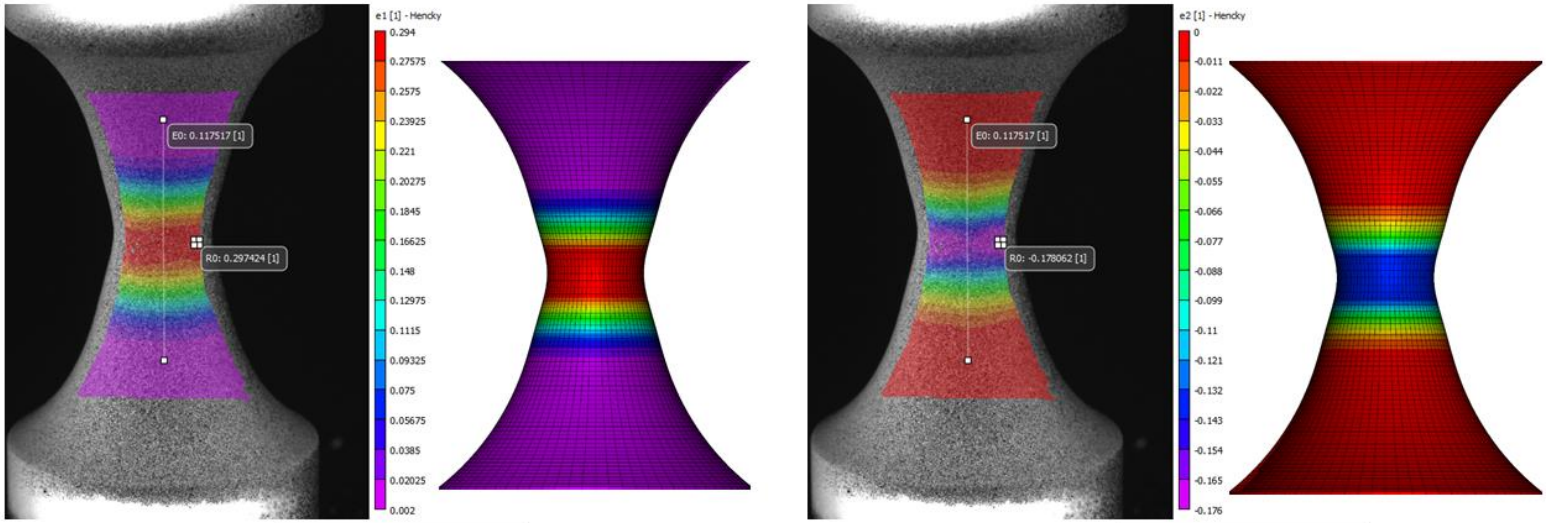

Figure 117: SG8_3 Principal Surface Strain Fringe Plots (Experimental vs. Simulation)

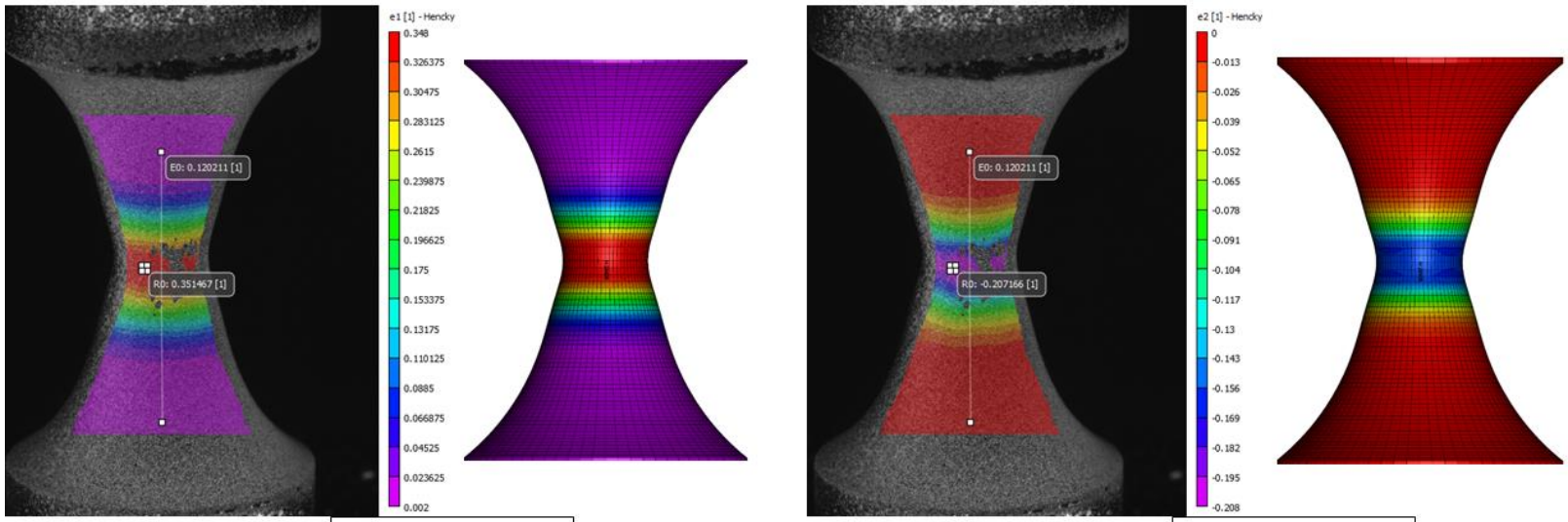

Figure 118: SG8_4 Principal Surface Strain Fringe Plots (Experimental vs. Simulation)

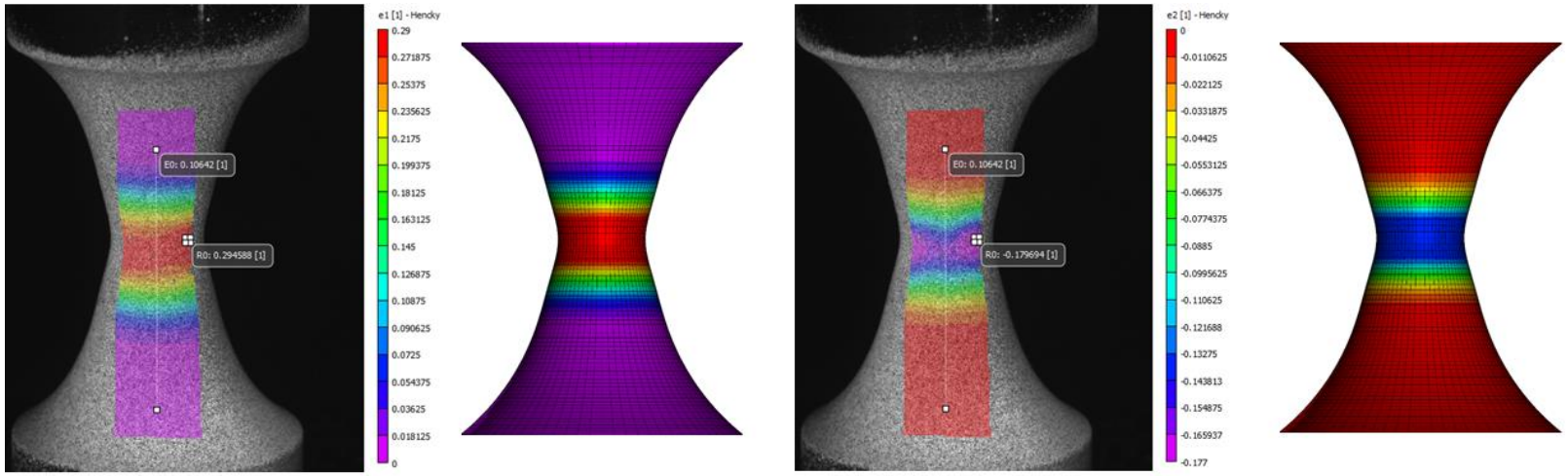

Figure 119:SG8_5 Principal Surface Strain Fringe Plots (Experimental vs. Simulation)

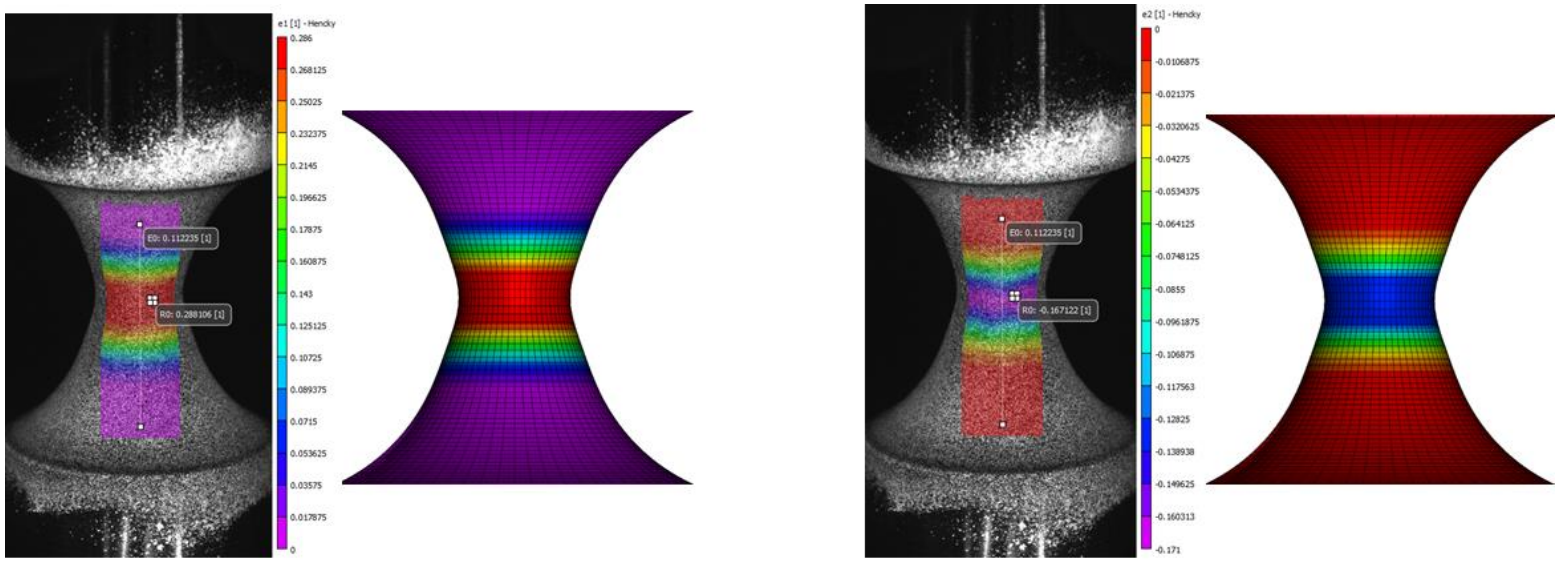

Max Principal Strain

Second Principal Strain

Figure 120: SG9_2 Principal Surface Strain Fringe Plots (Experimental vs. Simulation)

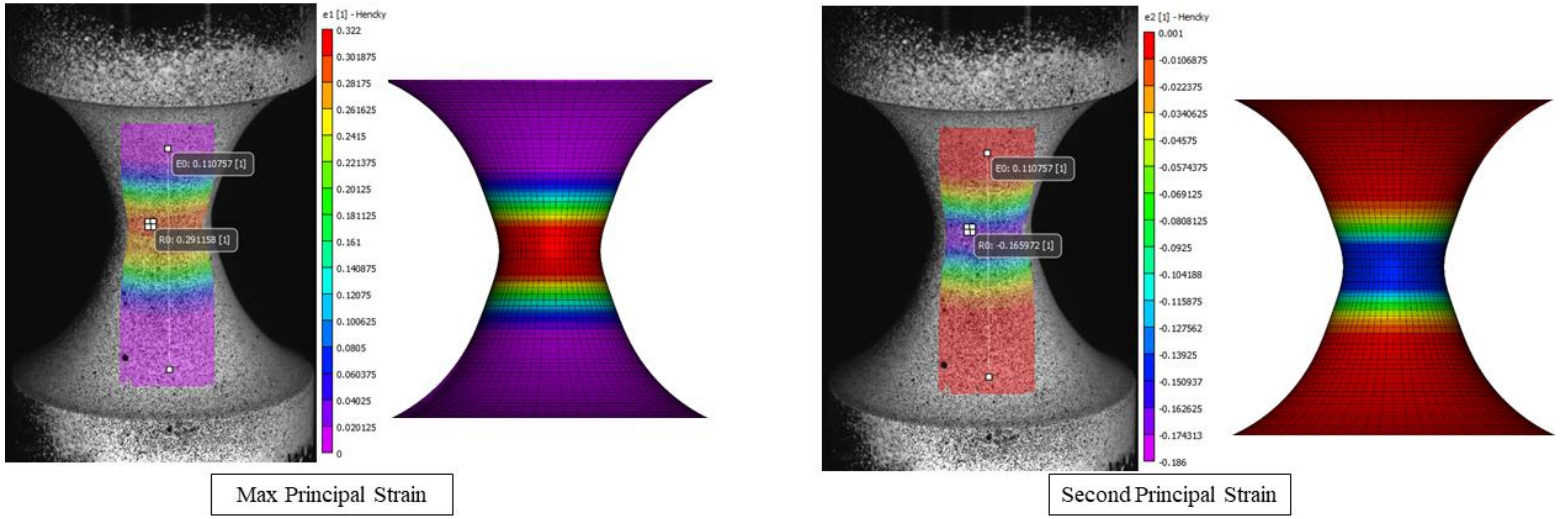

Max Principal Strain

Second Principal Strain

Figure 121: SG9_3 Principal Surface Strain Fringe Plots (Experimental vs. Simulation)

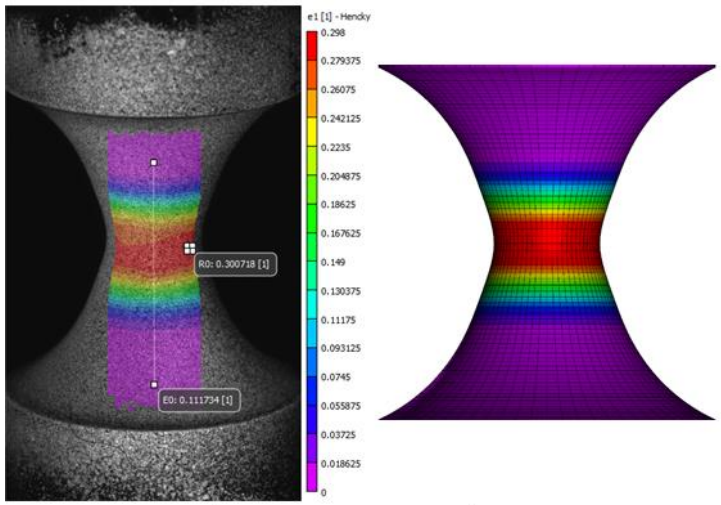

Max Principal Strain

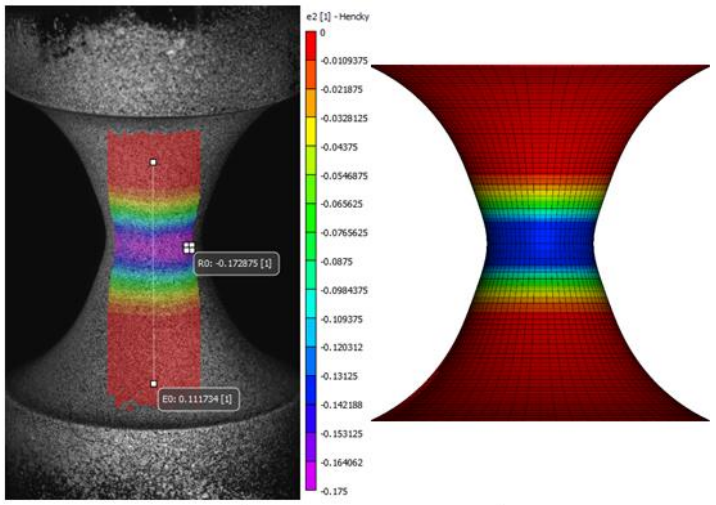

Second Principal Strain

Figure 122: SG9_4 Principal Surface Strain Fringe Plots (Experimental vs. Simulation)

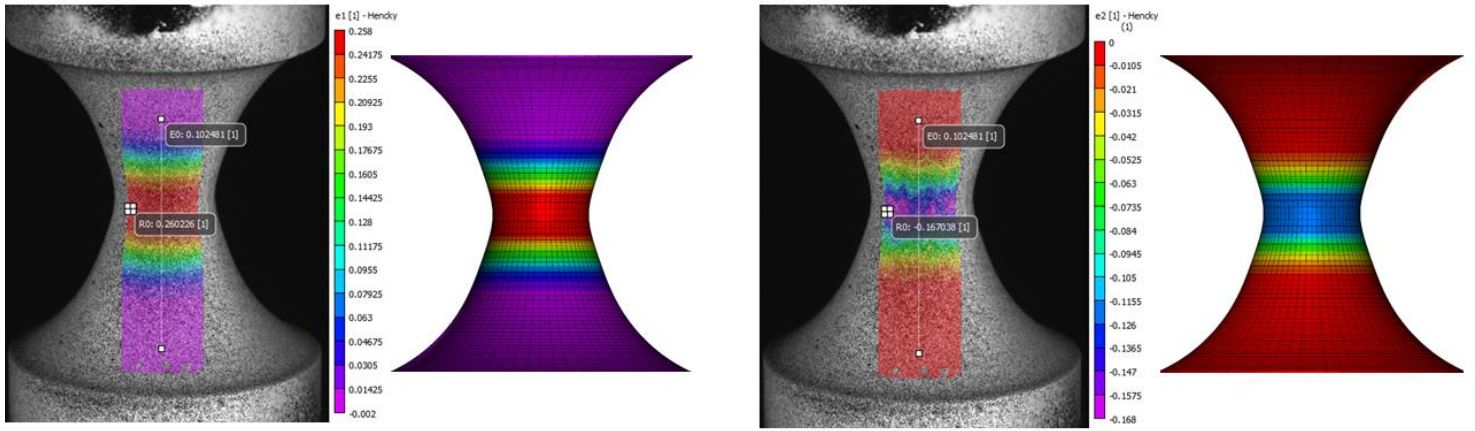

Max Principal Strain

Second Principal Strain

Figure 123: SG9_5 Principal Surface Strain Fringe Plots (Experimental vs. Simulation)

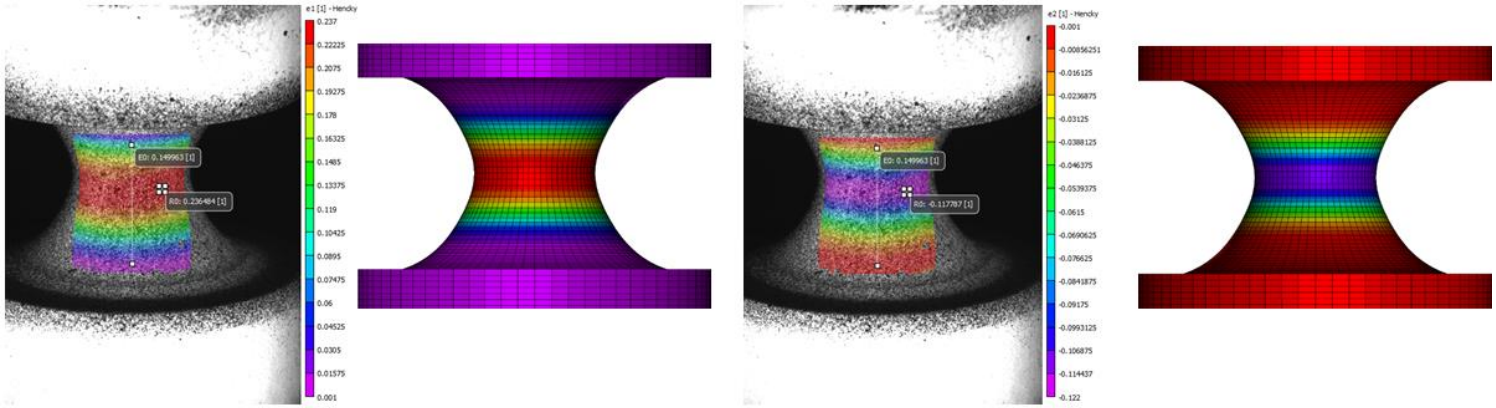

Max Principal Strain

Second Principal Strain

Figure 124: SG9_2 Principal Surface Strain Fringe Plots (Experimental vs. Simulation)

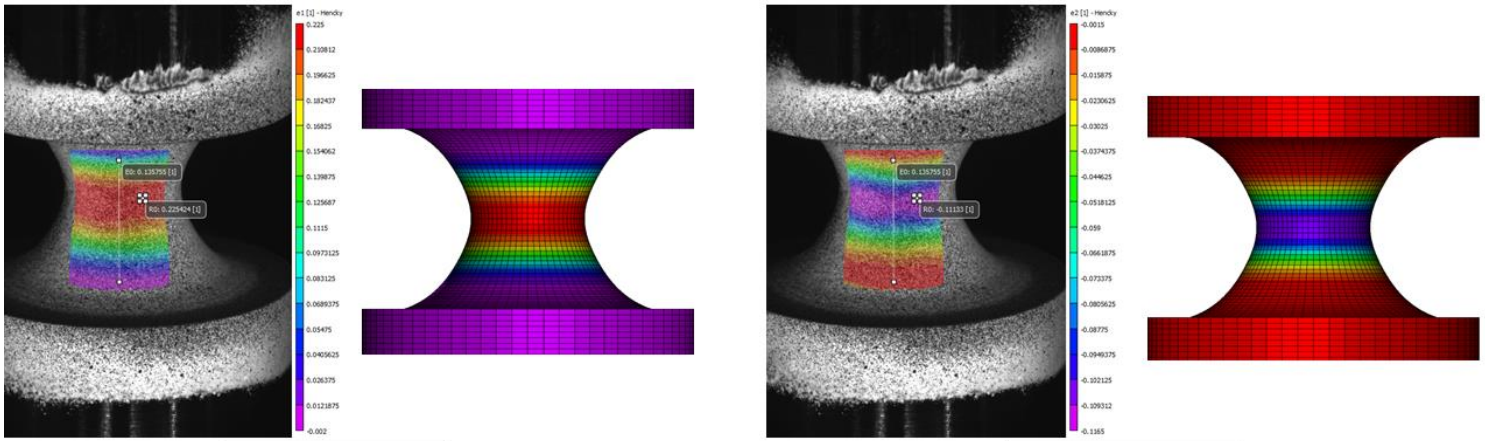

Figure 125: SG9_3 Principal Surface Strain Fringe Plots (Experimental vs. Simulation)

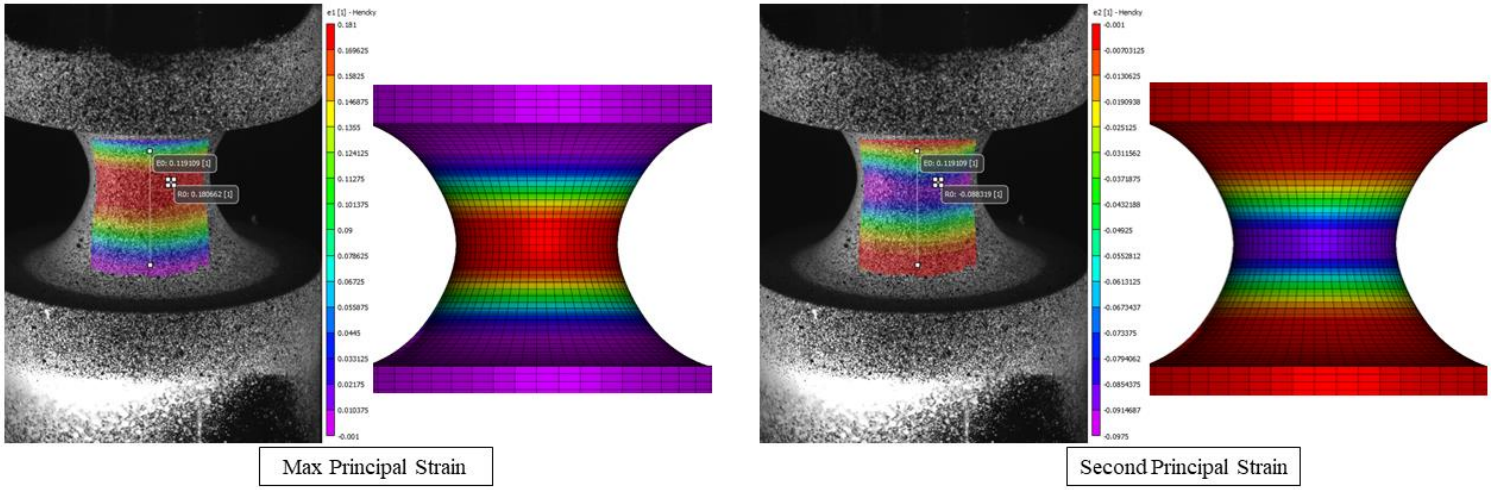

Figure 126: SG9_4 Principal Surface Strain Fringe Plots (Experimental vs. Simulation)

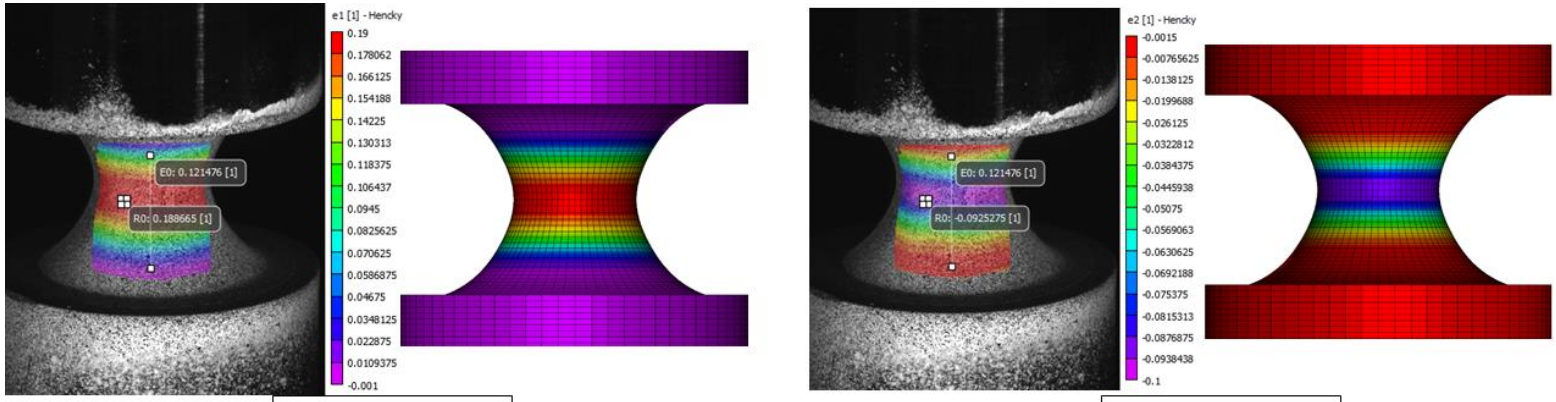

Figure 127: SG9_5 Principal Surface Strain Fringe Plots (Experimental vs. Simulatio

Stress State Parameters

Table 8: Individual Specimen Stress State Values

Spec No.	Triaxiality	Lode Parameter	Efp
SG5_1	-0.4720	0.981	0.486
SG5_2	-0.480	0.956	0.564
SG5_3	-0.480	0.996	0.480
SG5_4	-0.457	0.983	0.437
SG5_5	-0.466	0.985	0.461
SG6_1	-0.561	0.981	0.384
SG6_2	-0.586	0.991	0.453
SG6_3	-0.556	0.977	0.385
SG6_4	-0.570	0.988	0.404
SG6_5	-0.574	0.986	0.421
SG7_1	-0.633	0.989	0.351
SG7_2	-0.640	0.994	0.362
SG7_3	-0.641	0.982	0.392
SG7_4	-0.631	0.989	0.338
SG7_5	-0.637	0.979	0.389
SG8_1	-0.702	0.996	0.358
SG8_2	-0.681	0.979	0.332
SG8_3	-0.690	0.986	0.339
SG8_4	-0.688	0.980	0.353
SG8_5	-0.672	0.978	0.297
SG9_1	-0.519	0.995	0.275
SG9_2	-0.765	0.983	0.292
SG9_3	-0.770	0.987	0.292
SG9_4	-0.778	0.993	0.299
SG9_5	-0.760	0.986	0.258
SG10_1	-0.987	0.997	0.199
SG10_2	-0.983	0.984	0.236
SG10_3	-0.987	0.996	0.225
SG10_4	-0.965	0.981	0.181
SG10_5	-0.961	0.987	0.189

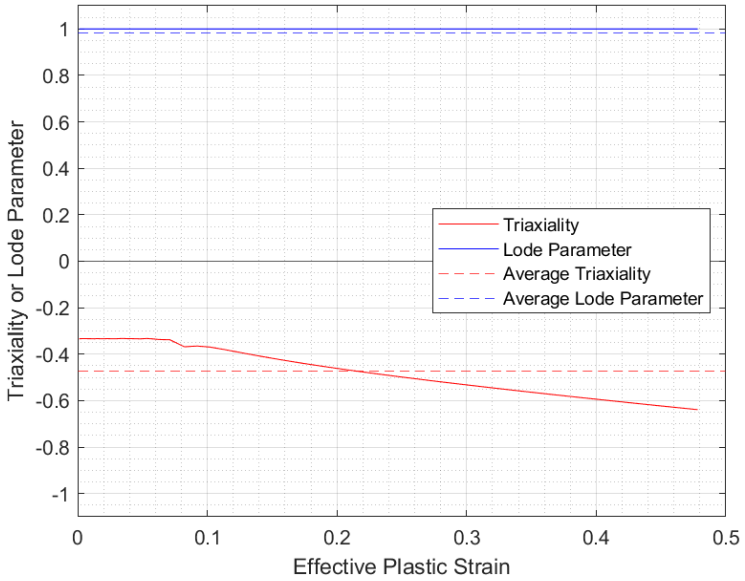

Figure 128: **Representative Triaxiality and Lode Parameter Histories for SG5-1**

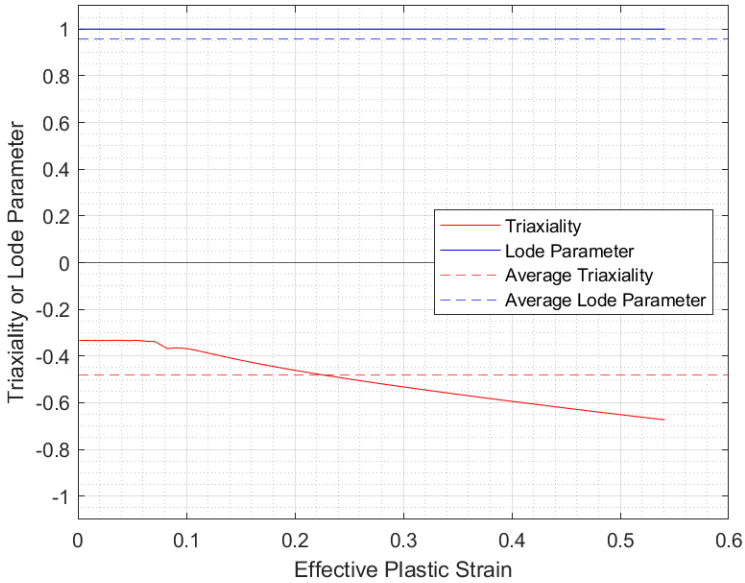

Figure 129: Representative Triaxiality and Lode Parameter Histories for SG5-2

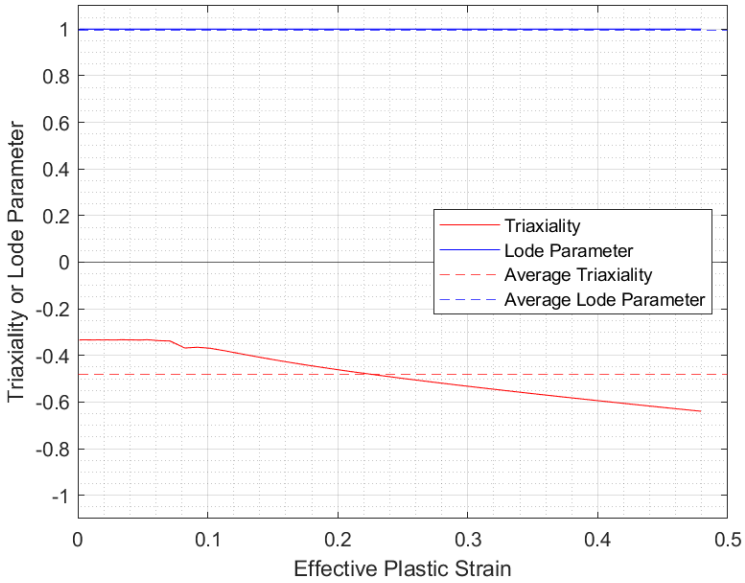

Figure 130: **Representative Triaxiality and Lode Parameter Histories for SG5-3**

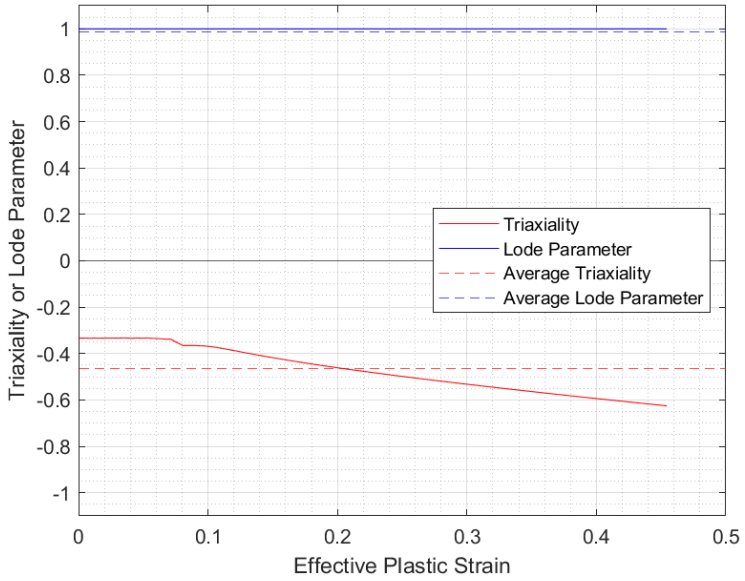

Figure 131: Representative Triaxiality and Lode Parameter Histories for SG5-5

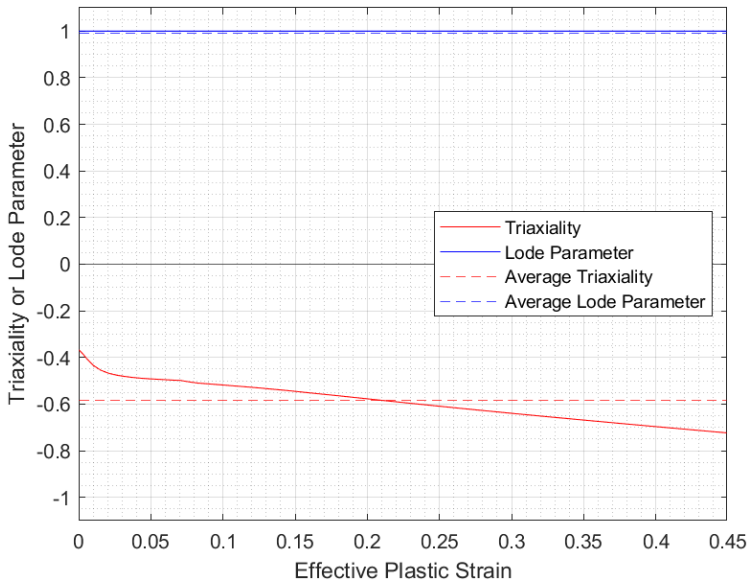

Figure 132: Representative Triaxiality and Lode Parameter Histories for SG6-2

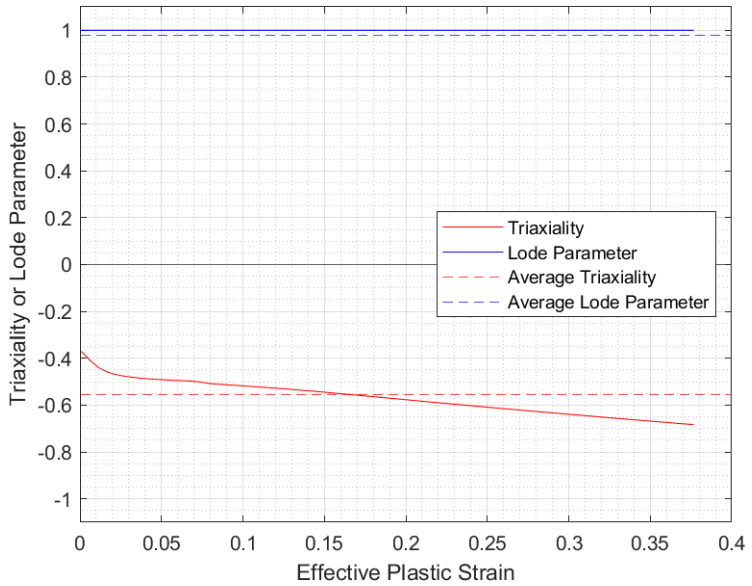

Figure 133: Representative Triaxiality and Lode Parameter Histories for SG6-3

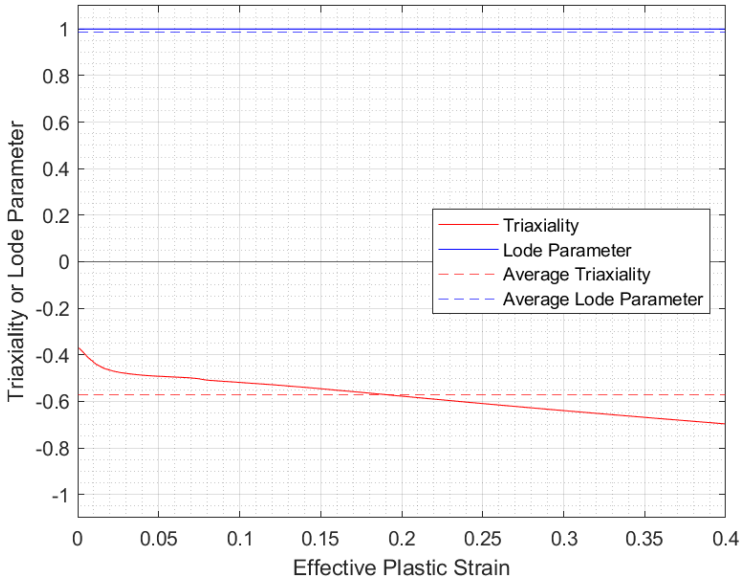

Figure 134: Representative Triaxiality and Lode Parameter Histories for SG6-4

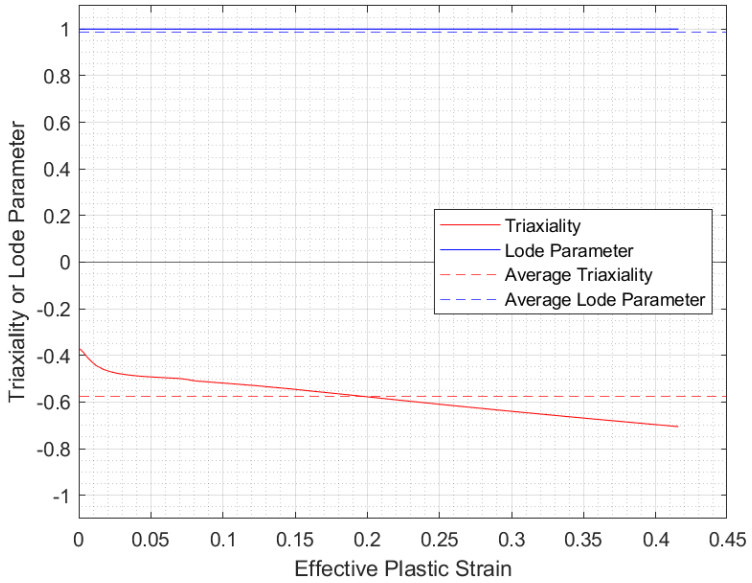

Figure 135: Representative Triaxiality and Lode Parameter Histories for SG6-5

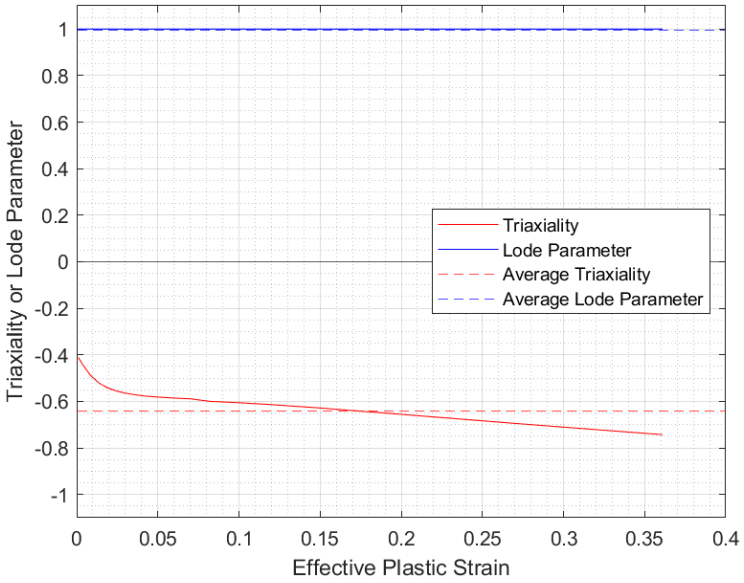

Figure 136: Representative Triaxiality and Lode Parameter Histories for SG7-2

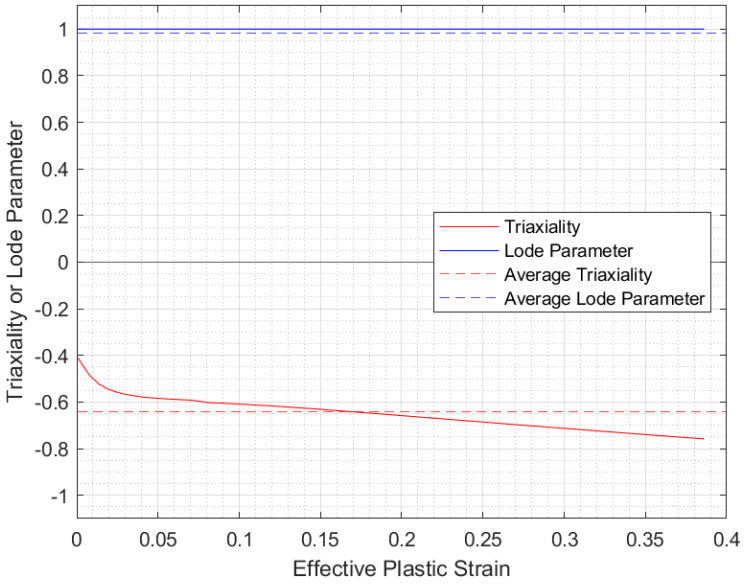

Figure 137: Representative Triaxiality and Lode Parameter Histories for SG7-3

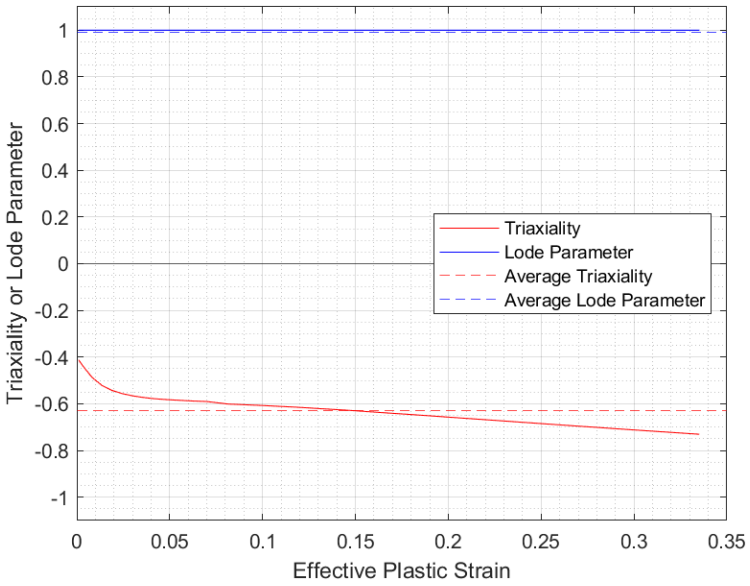

Figure 138: Representative Triaxiality and Lode Parameter Histories for SG7-4

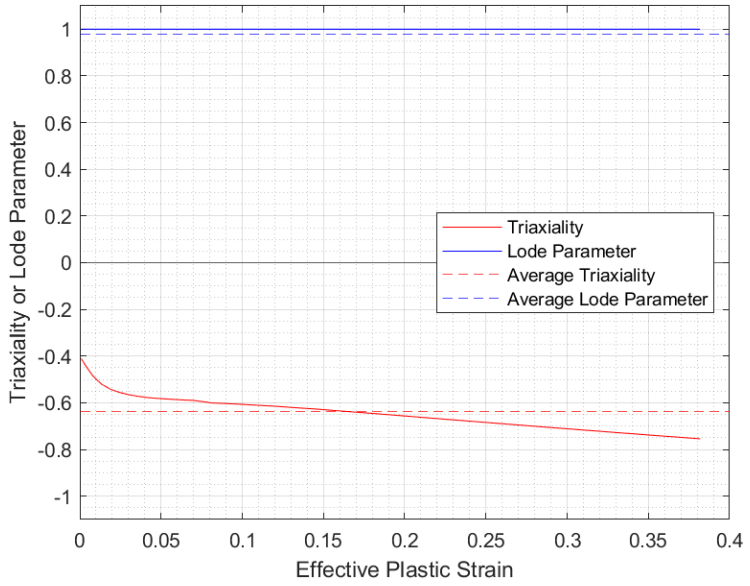

Figure 139: Representative Triaxiality and Lode Parameter Histories for SG7-5

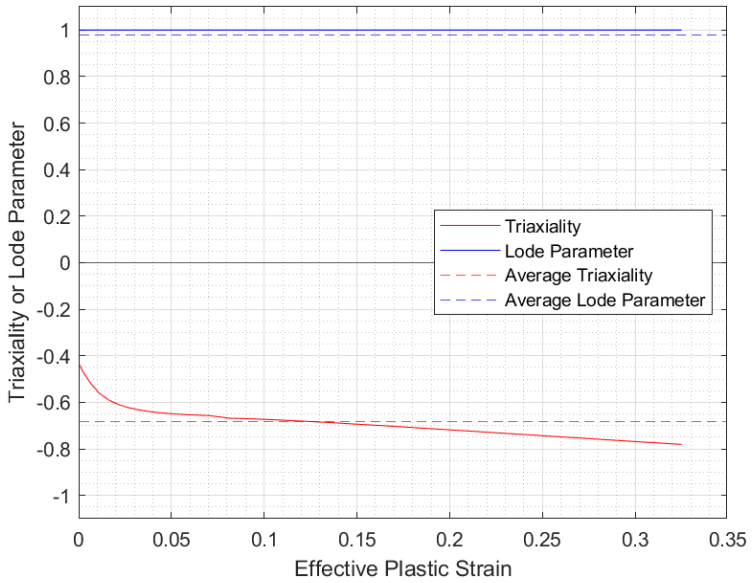

Figure 140: Representative Triaxiality and Lode Parameter Histories for SG8-2

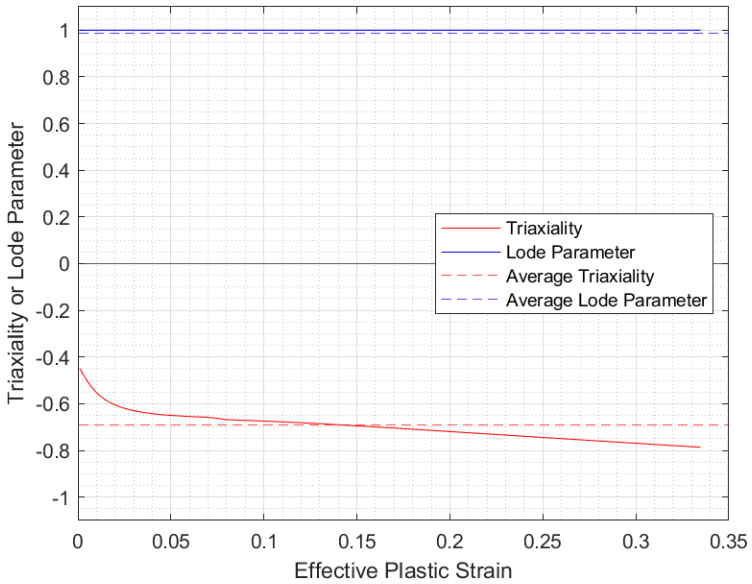

Figure 141: Representative Triaxiality and Lode Parameter Histories for SG8-3

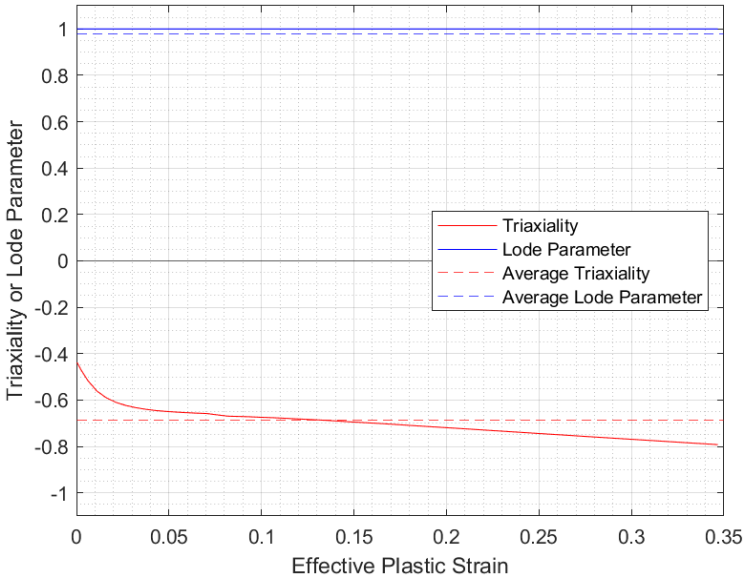

Figure 142: Representative Triaxiality and Lode Parameter Histories for SG8-4

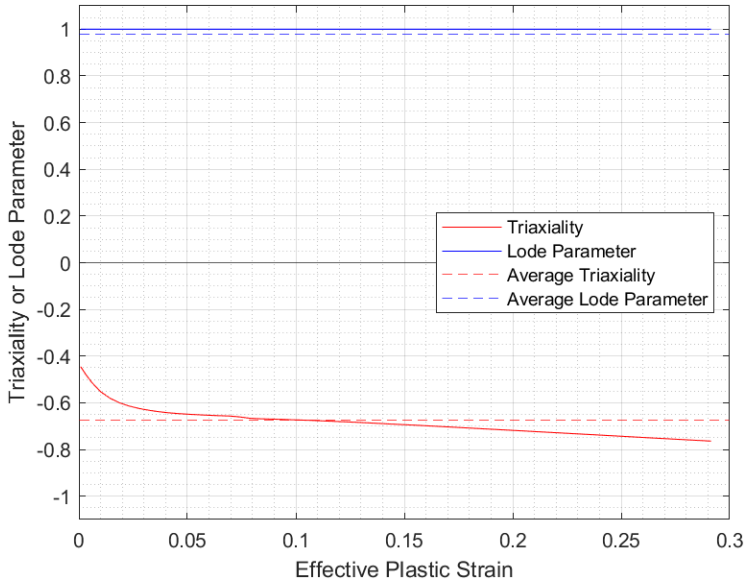

Figure 143: Representative Triaxiality and Lode Parameter Histories for SG8-5

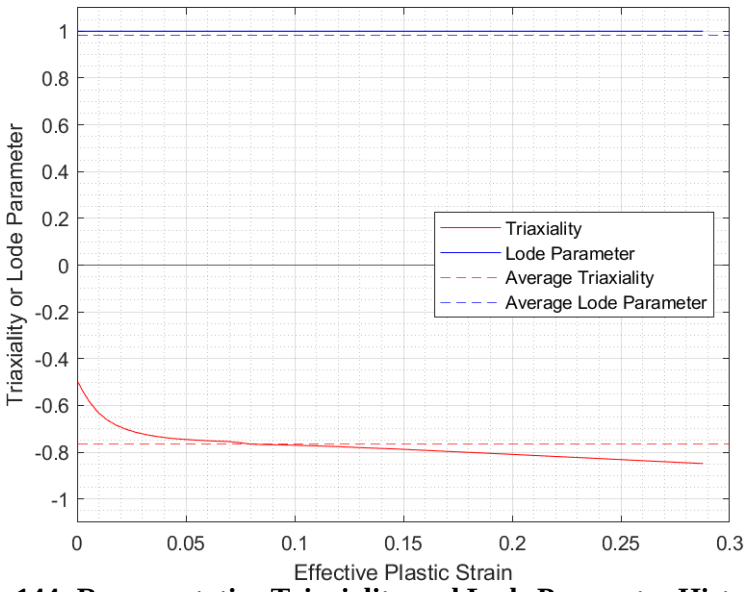

Figure 144: Representative Triaxiality and Lode Parameter Histories for SG9-2

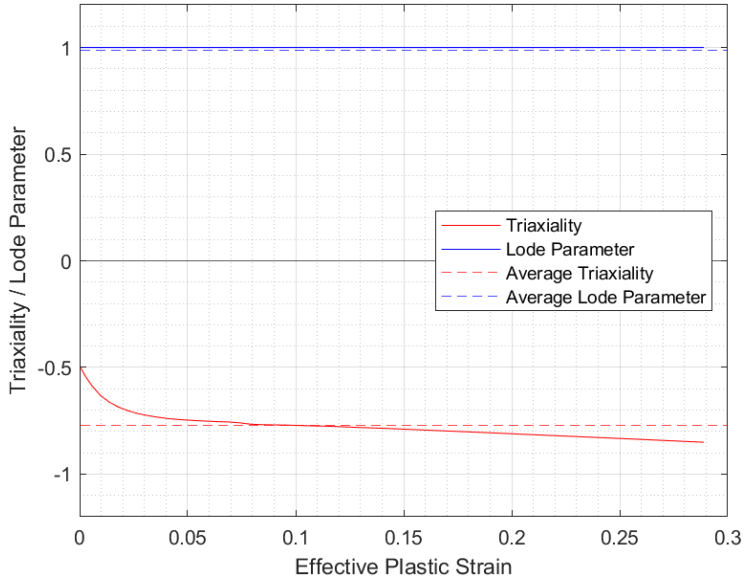

Figure 145: Representative Triaxiality and Lode Parameter Histories for SG9-3

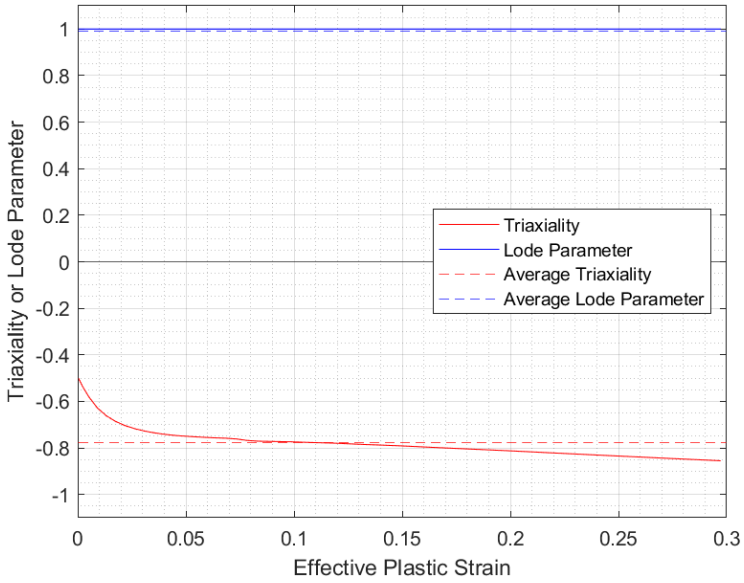

Figure 146: Representative Triaxiality and Lode Parameter Histories for SG9-4

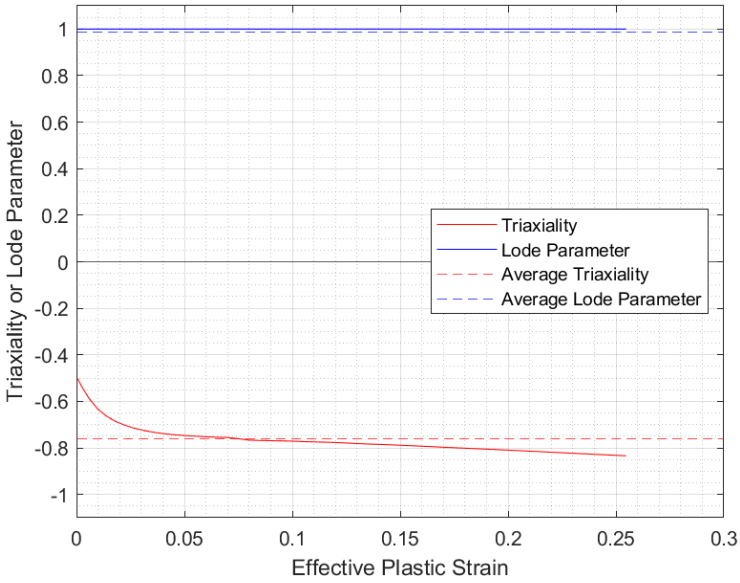

Figure 147 Representative Triaxiality and Lode Parameter Histories for SG9-5

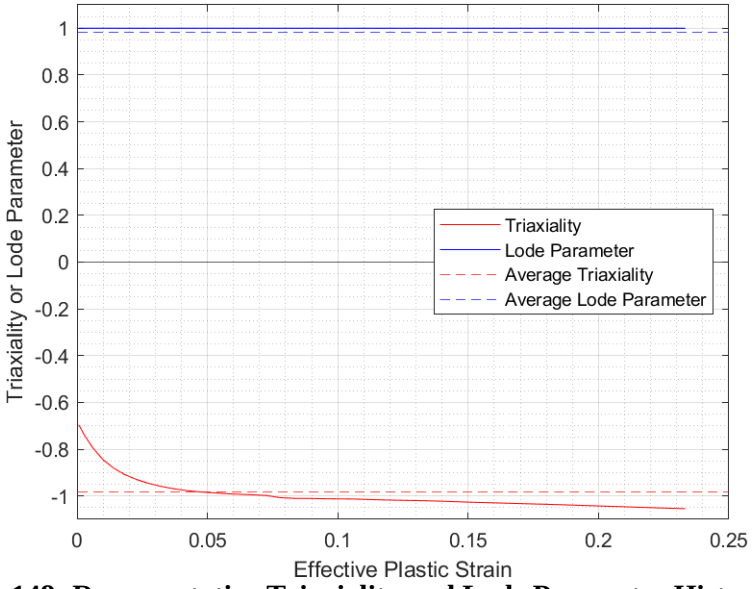

Figure 148: Representative Triaxiality and Lode Parameter Histories for SG10-2

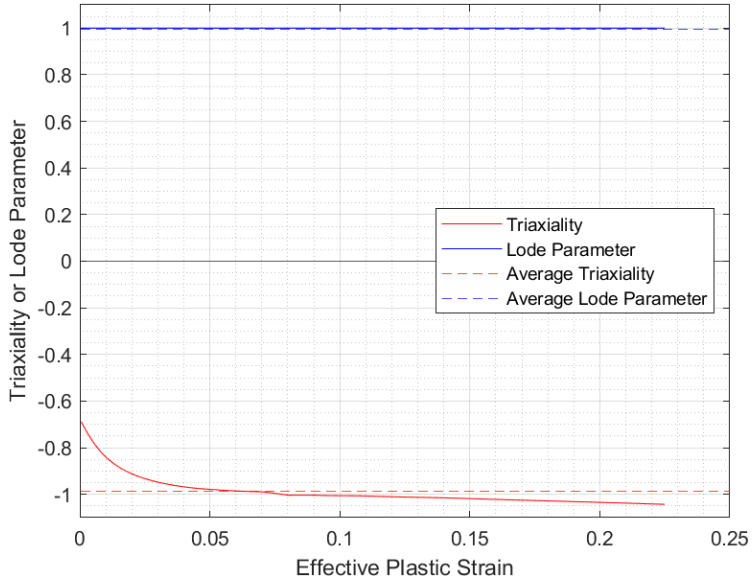

Figure 149: Representative Triaxiality and Lode Parameter Histories for SG10-3

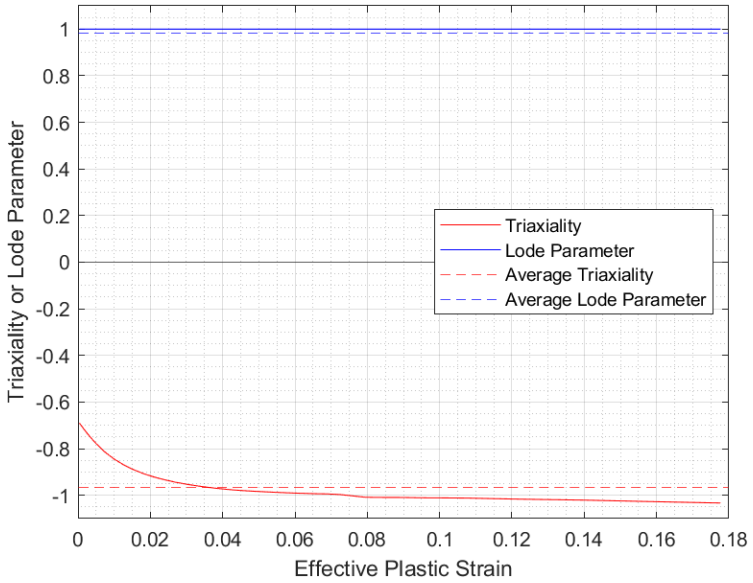

Figure 150: Representative Triaxiality and Lode Parameter Histories for SG10-4

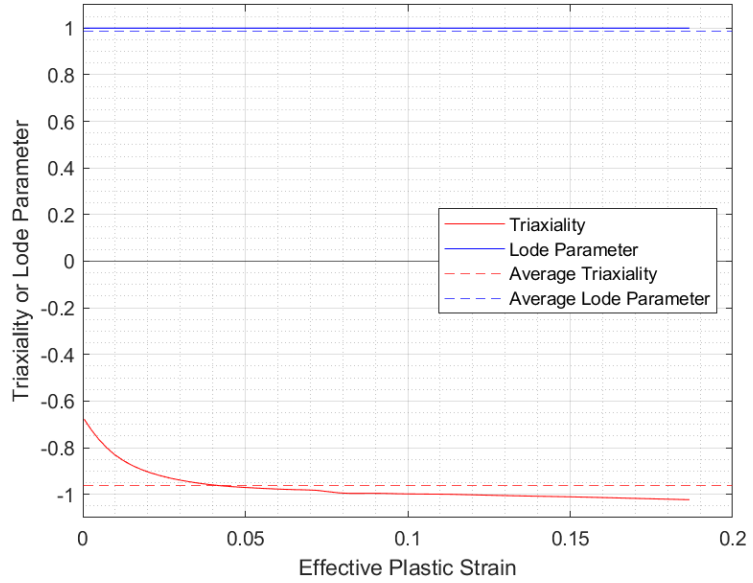

Figure 151: Representative Triaxiality and Lode Parameter Histories for SG10-5